Granular Flow Modelling of Rotating Drum Flows using Positron Emission Particle Tracking

Thirunavukkarasu Pathmathas

B.Sc.(Hons), University of Jaffna, Jaffna, Sri Lanka 2001

Pre-Doctoral Dip. in HEP, International Centre for Theoretical Physics (ICTP), Trieste, Italy 2004

MSc, Post Graduate Institute of Science (PGIS) University of Peradeniya, Peradeniya, Sri Lanka 2009

Supervisor

Dr Indresan Govender

Thesis presented for the degree of

DOCTOR OF PHILOSOPHY

in the Department of Physics

UNIVERSITY OF CAPE TOWN

February 2015

Contents

List of Figures

List of Tables

Abstract

Tumbling mills are characterized by a flowing granular mixture comprising slurry, ore and grinding media. Akin to fluid flow, a rheological description underpinning granular flow has long been expected and pursued by many researchers. Unfortunately, no single theory has hitherto been able to successfully describe all the peculiar features and flow phases of granular systems. Tumbling mills exhibit a rich coexistence of all known flow phases and is arguably the most complicated of the granular flow geometries. Not surprisingly, current comminution models are almost entirely empirical with limited predictive capability beyond their window of design.

Using Positron Emission Particle Tracking (PEPT) data we recover the key ingredients (velocity, shear rate, volume concentration, bed depth) for developing, testing and calibrating granular flow models. In this regard, 5 mm and 8 mm glass beads are rotated within a 476 mm diameter mill, fitted with angled lifter bars along the inner azimuthal walls and operated in batch mode across a range of drum rotation speeds that span cascading and cataracting Froude regimes. After averaging the PEPT outputs into representative volume elements, subsequent continuum analysis of the flowing layer revealed a rich coexistence of flow regimes −(i) quasi-static, (ii) dense (liquid-like), and (iii) inertial− that are consistent with the measured volume concentrations spanning these regimes in rotating drums. Appropriately matched constitutive choices for the shear stresses then facilitated the derivation of a new granular rheology that is able to (smoothly) capture all phases of the tumbling mill flow at transition points that match leading experimental findings reported in the literature. Limiting our models to athermal boundary conditions, we then derive the power density for better understanding of flow dissipation that ultimately drives the comminution purpose of tumbling mills. The rheology and power density models were then applied to the 5 mm and 8 mm glass bead data to reveal that shear power density is an order of magnitude larger than the normal component. Notwithstanding, the effective friction coefficient −which is akin to viscosity in typical fluids− remains relatively constant across most of the flowing layer with notable exponential growth across the interface from dense-to-inertial that continued into the inertial regime.

Acknowledgements

First and foremost I would like to express my sincere gratitude to my supervisor, Dr Indresan Govender, for giving me the opportunity to work uder his expert supervision. It has been an honour to be his PhD student in the Department of Physics at the University of Cape Town, South Africa. Without his thoughtful guidance, coherent and illumining instructions, financial support, constant encouragement and endless patience throughout the last four years, my PhD thesis would not have been possible to accomplish. I am also grateful to Dr Indresan Govender for his constant support to overcome Matlab issues that I faced during the PhD thesis write-up and preparation of research papers. I also thank him for the extended financial support towards attending international and local conferences. A special thanks is also extended to my wife, Jeyathadchayini and children, Thasshwin and Hariishni, for all their love and encouragement. Finally, I would like to thank my mother and late father, for their emotional love and care.

Chapter 1

Introduction

Particulate flow in rotating drums exhibit complex phenomena such as avalanching, segregation, mixing, drying, aggregation, comminution (abrasion, attrition and fracture) and convection. Industrially, the flow of granular material in rotating drums spans applications of mixing, rotary kilns and comminution. The nature of the latter application (tumbling mills) usually requires high frequency rotations of dense media in drums fitted with radial baffles to facilitate the strain rate and cataracting demands of the process, while mixers and kilns typically require an active flowing layer to mediate the mixing or heat transfer requirements.

Tumbling mills are reported to be $< 5\%$ efficient in the conversion of input power to useful comminution energy while accounting for more than 60% of the plant's operating costs [Wills (1997)]. Current breakage and transport models in tumbling mills are purely empirical machine models. While such models provide highly tweaked recipes for interpolating within the boundary conditions from which they were developed, the ability to extrapolate beyond the window of design is limited, and arguably dangerous, in light of depleting ore bodies and tighter environmental regulations. To remain competitive and economically viable within these stringent and ever changing boundary conditions, mining companies are forced to consider new comminution devices that can potentially increase operational efficiency. Central to this pursuit is an understanding of the mechanisms governing breakage (and transport) of granular flows. Mechanistic understanding holds the potential to step changes in comminution efficiency: Assuming that the mechanisms are independent of the boundary conditions, it is possible to change the boundary conditions (machine parameters, including novel machine designs) in model space and investigate the influence on efficiency.

Breakage energy is intimately coupled to the stresses that dominate within the flowing granular material. A complete description of the dissipation mechanisms in tumbling mills requires a theory that captures all significant phases of the granular flow. Unfortunately, the leading granular flow theories relevant to rotating drums [Midi (2004), Taberlet et al. (2006), Jop et al. (2006), Pignatel et al. (2012)] do not fully capture all flow phases prevalent in rotating drum flows.

In this thesis we develop a model of rotating drum flows that extends the visco-plastic rheology of Jop et al. (2006) to include kinetic and turbulent stresses. The resulting effective friction coefficient smoothly captures the expected phase transitions between the solid-, liquid- and

gas-like phases occurring in tumbling mill flows. Positron Emission Particle Tracking (PEPT) measurements are used to derive the key inputs to the model (solids concentration, velocity, shear rate, bed depth, free surface profile). A subsequent athermal energy balance facilitates estimates of the power dissipation distributions by the frictional, inertial, and turbulent stresses. Taken together with the PEPT inputs, the in-situ power dissipation is constituted for a range of drum rotation rates.

The rest of the thesis is organised as follows:

(i) Chapter 2 presents a review of the granular flow literature.

(ii) Chapter 3 describes the experimental program undertaken with PEPT and the key analysis schemes employed.

(iii) Chapter 4 describes the granular flow model with a particular focus on tumbling mill rheology.

(iv) Chapter 5 develops an athermal energy balance using the granular rheology developed in chapter 4. The chapter concludes with an illustration of the model outputs on the 60% critical speed PEPT data.

(v) Chapter 6 presents the results of the 5 mm and 8 mm glass beads rotated in a 476 mm diameter tumbling mill across a range of drum rotation rates.

(vi) Chapter 7 presents the conclusions.

Chapter 2

Literature Review

2.1 Flow regimes in rotating drums

Granular flows in rotating drums are often described by a flowing free surface layer over a densely packed rising en-masse that is considered static relative to the rotating drum. Figure (2.1) is a simple illustration (not to scale) of the typical flow regimes studied primarily in the physics literature and is based on the schematic given in Midi (2004).

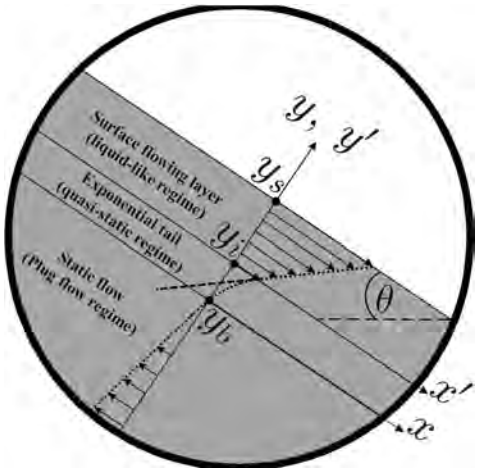

Figure 2.1: Granular flow in a clockwise rotating drum according to Midi (2004). The arrows below the top of the surface flowing layer indicate velocities whose profile is delineated by the dotted line. The linear velocity profile in the surface flowing layer is extrapolated along the dashed line to find the intersection with the $y-$axis.

Starting at the top of the surface flowing layer (often referred to as the free surface layer) and moving into the bed along the negative y-direction, figure (2.1), the velocity in the surface flowing layer decreases essentially linearly with depth until very close to the bottom of the flow where the decrease starts to slow down exponentially with further increases in depth. The exponential tail is a solid-like regime that is characterised by dense quasi-static flows in

which the deformations are very slow and the particles interact by frictional contact [Roux (2002)]. The linear region is a liquid-like regime that is also densely packed but still able to flow like a liquid with particles interacting by both friction and collision [Pouliquen and Chevoir (2002), Midi (2004), and Forterre and Pouliquen (2008)]. Henein et al. (1983) and Mellmann (2001) classified granular flows in rotating drums by the Froude number $F_r = \frac{\omega^2 R}{g}$; see figure (2.2), where ω is the angular speed in radians per second, R denotes the internal radius of the drum and g is the usual acceleration due to gravity in $\left[\ \mathrm{m/s^2}\right]$. Cascading (figure (2.2d)) and cataracting (figure (2.2e)) flows exhibit an additional gas-like regime that is characterised by very rapid and dilute flows in which the particles interact mainly by collision [Goldhirsch (2003)]. Below the quasi-static regime shown in figure (2.1), the flow is assumed static relative to the rotating drum, i.e. the grains are assumed to be moving with the same angular velocity as the drum, and is often compared to a solid plug moving with the rotating drum −the so-called plug flow.

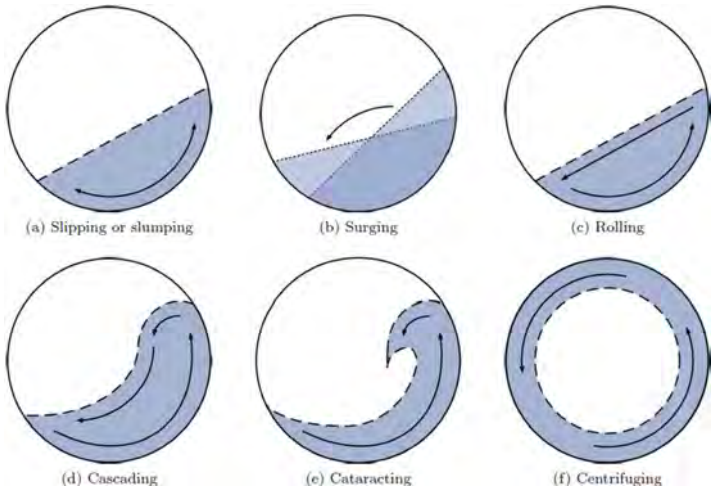

Figure 2.2: Six categories of rotating drum flows in alphabetical order of increasing drum rotational speed or wall friction.

2.2 Measurements in rotating drums

The complicated influence of boundary conditions to the flow in rotating drums, especially near the highest and lowest points of the bed, has resulted in most reported measurements occurring along a line similar to the y-axis shown in figure (2.1) [Nakagawa et al. (1993), Yamane et al. (1998), Ding et al. (2001), Orpe and Khakhar (2001), Midi (2004), and Orpe and Khakhar (2007)]. The choice of this line, which is essentially along the central region of the bed, is motivated by the homogeneity, maximum thickness of the flowing layer and exponential tail, unidirectionality of the flow, and the slow variation of the velocity profile across the layer interfaces.

Many experimental investigations of rotating drum flows have exploited imaging modalities across the electromagnetic spectrum, ranging from transparent end window photographic filming in the visible spectrum, Rogovin and Herbst (1989) and Santomaso et al. (2003), to low wavelength gamma ray techniques, Parker et al. (1997). Particle image velocimetry (PIV)

has provided useful measurements of the ensemble-averaged streamwise velocity profiles in the fluidised layer of slowly rotating drum flows, Jain and Ottino (2002). Nakagawa et al. (1993) used magnetic resonance imaging (MRI) of nearly spherical mustard seeds in a smoothly lined horizontal cylinder to measure the velocity and free surface for speeds operating in the rolling mode; see figure (2.2c). Morrell (1992) employed streak photography of coloured tracers through a transparent end window of a pilot scale tumbling mill to constitute the velocity profile of steel balls. The resulting linear velocity profile formed the key ingredients to his well-known power draught model. Orpe and Khakhar (2001) also employed streakline photography to the flow of mono-sized grains (steel balls, glass beads and sand) in slowly rotating drums and successfully measured the free surface. Positron Emission Particle Tracking (PEPT) has been very successful in studying granular flows in rotating drums that span most of the Froude regimes shown in figure (2.2). Parker et al. (1997) used PEPT in smoothly lined drums operated in the rolling-to-minimally cascading regime to measure a non-linear surface layer and an underlying bed (the rising en-masse region) that deviated from solid body motion due to considerable slip at the drum wall. Ding et al. (2001) overcame the slip problems experienced by Parker et al. (1997) with the use of sand paper (lined along the inner azimuthal wall) to produce measurements consistent with Nakagawa (1994) and Nakagawa et al. (1997). The data also successfully validated their continuum model based on the thin layer approximation.

2.2.1 Scaling relations

Most scaling relations reported in the literature are based on measurements along the central region of the flowing layer, similar to the $y-$ axis shown in figure (2.1). The following assumptions are usually employed when formulating scaling relations:

(i) No cascading or cataracting

(ii) An essentially constant bed repose

(iii) Bed depth (h) is small compared to the drum radius (R) so that $h^2 \ll R^2$

(iv) Rising region exhibits plug flow such that the flux per unit length of drum $Q_r = \left(\frac{\omega}{2}\right)\left[R^2 - h^2\right] \approx \left(\frac{\omega}{2}\right) R^2$

Emergent from the various measurements of rotating drum flows are a mixture of scaling laws, not all in agreement with current models. For example, the recent visco-plastic rheology of dense granular flow [Jop et al. (2006)] suggests that the depth-averaged velocity $\langle v \rangle \propto h^{3/2}$, where h is the flowing layer thickness. However, measurements in rotating drums by Midi (2004) suggest a scaling of $\langle v \rangle \propto h$. Parker et al. (1997) used PEPT measurements in rolling mode flows to conclude $\langle v \rangle \propto h^0$, while Felix et al. (2007) found $\langle v \rangle \propto h^m$, where the exponent m varies with the geometry of the system. Variations in m were also observed by Ancey (1999) in the frictional-collisional regime of flows down rough, inclined channels: for high inclinations of the channel $1 < m < 2$ while for gentle slopes $m \simeq 0$, suggesting that the mean velocity of the flow is constant and hence independent of the flowing layer depth. We note here the similarity with the scaling of Parker et al. (1997). Pignatel et al. (2012) also found a power law scaling similar to Felix et al. (2007). Using a best fitting power law $\left[\frac{h}{d} = 2.86\left(\frac{\langle v \rangle h}{d\sqrt{dg}}\right)^{0.44}\right]$

that was obtained using their entire data set, it is easily shown that $m \approx 1.27$. The work of Orpe and Khakhar (2001) also indirectly implies $\langle v \rangle \propto h^3$. An attractive consequence of the linear scaling $\langle v \rangle \propto h$ is a constant shear rate $\left[\dot{\gamma} = \frac{\langle v \rangle}{h} \equiv \text{constant}\right]$ which Midi (2004) estimated as $0.5\sqrt{\frac{g}{d}}$. The attractiveness relates to the fact that most constitutive relations for the shear stress τ are based on $\dot{\gamma}$, and hence simple constitutive relations can exist.

The angle of repose (θ) in rotating drums have also had mixed scaling relations. At the very low end of the continuous flow regime, Rajchenbach (1990) found that $\theta \propto \omega^2$. Dury et al. (1998) used MRI measurements of mustard seeds, end-window measurements (by looking through acrylic end caps) and Discrete Element (DE) simulations to show a linear dependence ($\theta \propto \omega$) consistent with the continuous flow regime. Sepulveda et al. (2005) reported a linear scaling between the angular span of the granular bed and angular speed of the drum. The microscopic effects of rough particles was shown to increase the angle of repose by 10° over smooth particles across a wide range of rotation speeds. Finally, intimately connected to the angle of repose is the hysteresis between starting and stopping angles associated with steady, continuous flows [Dury et al. (1998) and Forterre and Pouliquen (2008)]. The fact that various scaling relations exists suggest that the underlying mechanisms governing granular flows in rotating drums is not yet fully understood. The problem is further compounded by the limited measurements in the cascading and cataracting Froude regimes where the key rheological measures (angle of repose, flowing layer depth and depth-averaged velocity) become ambiguous.

2.2.2 Tumbling mills

Tumbling mills −the industrial application of rotating drum flows in the minerals industry− are best classified by cataracting (see figure (2.2e)) which typically contains all three flow regimes. An additional characteristic feature of tumbling mills is the radial baffles or lifter bars that facilitate cataracting motion by increasing the effective friction between the azimuthal wall and the granular bed. Govender (2005) used bi-planar xray imaging to track the 3D motion of a representative plastic bead moving within a 142 mm diameter experimental tumbling mill containing 6 mm diameter plastic beads and operated in the cataracting flow regime, figure (2.3(centre)). Despite the high accuracy trajectory fields reported by the authors [Govender et al. (2004)], the constraints imposed by diagnostic xrays and medical protocols for continuous exposure limited the study to very low density materials and insufficient data for computing key rheological parameters like the volume fraction distribution (ϕ). Notwithstanding this limitation, the time-averaged velocity per unit volume of the flow was very accurately calculated from the trajectory (x, y, z, t) of a single tracer under steady, fully developed flow conditions and the ergodic assumption [Wildmann et al. (2000)]. Figure (2.3) also clearly shows the influence of the baffle geometry −the leading face angle of the baffles in this case− on the amount of cataracting induced, and highlights the rich coexistence of Froude regimes that are encountered in industrial granular flow systems.

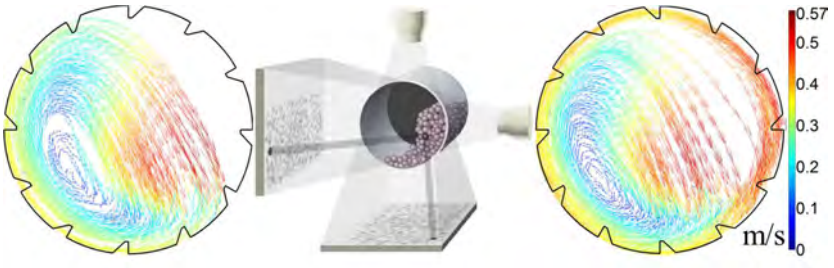

Figure 2.3: Illustration of the biplanar xray imaging technique (centre image) used to track the 3D motion of a representative particle (6 mm diameter plastic bead with a thin layer of silver lacquer painted onto the surface) moving within the bulk of the flowing granular material (6 mm plastic beads). The 142 mm diameter perspex tumbling mill was filled to 40 % and rotated at 78.6 rpm. The resulting time-averaged velocity per unit volume of the flow field (right and left images) clearly shows all Froude regimes being accessed by the tracer [after Govender (2005)].

Morrison (2012) used PEPT to study granular flows in tumbling mills. After constituting the residence time fractional distribution (RTFD) in a similar manner to Wildmann et al. (2000), the resulting distribution was used to measure and numerically model the free surface (dashed white line) and equilibrium surface (solid white line) shown in figure (2.4). The cascading layer (intermediate liquid-like regime) is separated from the rising en-masse layer (static flow regime) by a surface of zero velocity termed the equilibrium surface[1] in the minerals engineering literature [Powell et al. (2003)]. The shoulder denotes the region at the top of the flow where the granules lose contact with the inner drum wall and either cascade down the free surface layer or get projected into free fall.

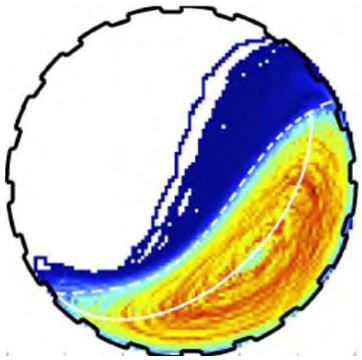

Figure 2.4: Illustrating the free surface (dashed white line) and equilibrium surface (solid white line) of a 5 mm glass bead mixture in a tumbling mill operated in the cataracting flow regime. The residence time fractional distribution was calculated from PEPT data of a representative 5 mm glass bead tracer and formed the basis for measuring and numerically modelling the free surface and equilibrium surface [after Morrison (2012)].

[1]The equilibrium surface projects axially along the length of the drum. Figure (2.4) only shows the front view of the surface.

2.3 Granular flow modelling of rotating drum flows

Beyond rotating drums with rough azimuthal faces (roughness achieved by lining the inner azimuthal wall with granular material) typically studied in the physics literature [Rajchenbach (1990), Zik et al. (1994), Elperin and Vikhansky (1998), Yamane et al. (1998), Puri and Hayakawa (1999), Orpe and Khakhar (2001), and Taberlet et al. (2006)], the case of industrial tumbling mills with lifter bars of varying geometries has only been dealt with empirically in the minerals engineering literature [Hogg and Feurstenau (1972), Harris et al. (1985), and Morrell (1992)]. Rajchenbach (1990) was the first to consider a Bagnoldian [Bagnold (1954)] formulation of granular flow in rotating drum systems. A useful outcome from the model was that the velocity in the thin (but finite sized) free surface layer (with constant thickness x_0) varied as $v_z(x) \propto x^{3/2}$ for the flow and coordinate system illustrated in figure (2.5).

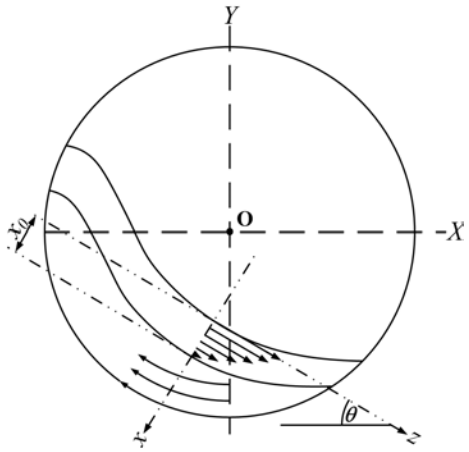

Figure 2.5: Illustration of the velocity profile along a perpendicular to the thin (but finite sized) layer of the free surface. The rising en-masse layer below the surface of zero velocity is assumed to moved like a solid plug.

Motivated by experimental observations of segregation in a bimodal mixture of similar sized glass beads and sand, Zik et al. (1994) proposed a mechanistic model of the free surface shape and segregation. The flow geometry and coordinate system employed by Zik et al. (1994) is similar to figure (2.5). By assuming a thin flowing layer of constant depth (x_0) and approximating it to a Newtonian fluid with a constant viscosity η, the resulting force balance per unit area between gravity and a Coulomb-like frictional force recovers, after integration, the flowing layer velocity $v_z(x) \propto x^2$. A subsequent flux balance (per unit length of the drum) between the flowing layer and the rising bulk under steady flow conditions then leads to the equation of the free surface, equation (2.1).

$$\left(\frac{\phi g \rho_m}{3\eta}\right) x_0^3 \frac{1}{\sqrt{1+\left(\frac{\partial Y_s}{\partial X}\right)^2}} \left(\frac{\partial Y_s}{\partial X} - \tan\theta_0\right) = \frac{1}{2}\omega\left(R^2 - X^2 - Y_s^2\right), \tag{2.1}$$

where ρ_m is the material density, ϕ the volume concentration, $\mu = \tan(\theta_0)$ is related to the limiting friction angle θ_0 in analogy to Coulomb friction acting on the classical block-

on-inclined-plane problem, (X, Y_s) denote the coordinates to the free surface, and the other terms are as previously defined. Figure (2.6) is an illustration of two solution schemes that successfully recover the characteristic S-shape of the free surface: (i) the dashed-dotted line is based on an explicit Runga-Kutta solution according to Dormand and Prince (1980) after the ordinary differential equation was recast into an explicit form. (ii) the solid line was recovered using an implicit solution scheme to solve equation (2.1) together with a model for the filling fraction as described by Tordesillas and Arber (2005). In both explicit and implicit solution, identical parameters were employed; see caption in figure (2.6) for details.

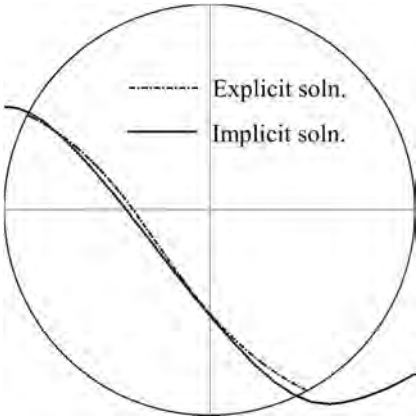

Figure 2.6: Numerical solutions to equation (2.1) for a 150 mm diameter drum with a 30 % filling, $\eta = 5$, $\mu = 0.5$, $\omega = 5.66$, $\phi = 0.58$, and $x_0 = 0.048$. The dashed-dot line is based on an explicit Runga-Kutta solution by Dormand and Prince (1980) and the solid line is based on an implicit solution scheme with an additional model for the filling fraction according to Tordesillas and Arber (2005).

By identifying the small parameter $\varepsilon \propto d/L$ within a Bagnoldian shear stress paradigm and a simple hydrostatic-like pressure, where d is the particle diameter and $2L$ the length of the free surface, Elperin and Vikhansky (1998) derived closed form analytical solutions for the shape of the free surface profile, equation (2.2), and thickness of the flowing layer, equation (2.3).

$$h(z) = \frac{\frac{4}{5}\left(\frac{\omega}{2}\right)^{\frac{6}{5}}\left[C_1 - \left(1-z^2\right)^{\frac{6}{5}}\right] - \sin(\theta)\left(\frac{\omega}{2}\right)^{\frac{2}{5}}\left[C_2 - \left(1-z^2\right)^{\frac{2}{5}}\right]}{\cos(\theta) + \sin(\theta)}, \text{ and} \tag{2.2}$$

$$\delta(z) = \left[\frac{\omega}{2}\left(1-z^2\right)\right]^{\frac{2}{5}}, \tag{2.3}$$

where C_1 and C_2 are integration constants and θ is governed by a Mohr-Coulomb failure criteria at the transition from solid to liquid-like behaviour, i.e. the ratio between shear and normal stresses is constant, for a 30 % fill level and coordinate system as shown in figure (2.7). The free surface $h(z)$ and layer thickness $\delta(z)$ shown in figure (2.7) are based on a 150 mm diameter drum rotated at $\omega = 1.88$ radians per second. The 30 % filling corresponds to

$C_1 = 0.8$ and $C_2 = 1.6$. It is interesting to note the symmetric, bimodal shape of the free surface.

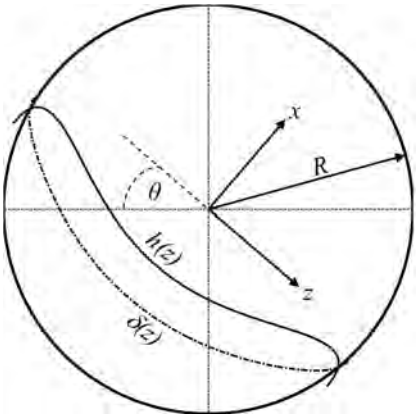

Figure 2.7: Illustration of the free surface profile $h(z)$ and flowing layer thickness $\delta(z)$ according to the model of Elperin and Vikhansky (1998). The plot is based on a 150 mm diameter drum with a 30 % filling, rotating at $\omega = 1.88$ radians per second. The coordinate system is also shown.

Bouchaud et al. (1994) proposed a phenomenological description−the so-called BCRE model− for a small layer of grains rolling across the top of a static region. The time evolution of both layers, i.e. static and rolling layers, is regulated by an exchange parameter that determines dislodgement of static grain (respectively, trapping of mobile grain) probabilities caused by the local slope of the flowing layer being greater (respectively, less) than some neutral slope at which equal probability exists. Boutreux et al. (1998) modified the model for thick flows by including a saturation for the exchange term, that ultimately drives the probability, when the flowing layer thickness is greater than some screening length. The more fundamental hydrodynamic approach of mass and momentum conservation for averaged quantities across the layer depth also leads to evolution equations for the flowing layer thickness. Douady et al. (1999) included a mass exchange mechanism between the flowing and static layer to account for the evolution of the static layer height. Taken together, these conservation equations are commonly referred to as the Saint-Venant hydrodynamic model which describes granular flow through the evolution of the flowing and static layer thickness. Aradian et al. (2002) showed the equivalence of the saturated BCRE model with the more fundamental Saint-Venant hydrodynamic model. de Gennes (1995) notes that the BCRE model is valid only for slowly rotating drums and a flowing layer thicknesses of a few particle diameters. Free surface profiles of fully cascading and cataracting flows are thus expected to be outside the scope of this model. Khakhar et al. (1997) revisited the hydrodynamic approach for depth averaged quantities applied to a slowly rotating drum with a thin, essentially flat, free surface layer atop a fixed bed of particles rotating at the angular speed of the drum. Streakline photographs allowed for the measurement of layer thickness profiles that verified the proposed depth averaged, hydrodynamic model. Orpe and Khakhar (2001) continued the streakline measurements for higher drum rotations and successful measured the S-shaped profile of the free surface. Comparison with the models of Khakhar et al. (1997), Makse (1999) and Elperin and Vikhansky (1998) showed good agreement with layer thickness profiles at low

Froude numbers. At higher Froude numbers, only the model of Khakhar et al. (1997) proved successful in predicting the asymmetric layer thickness and variations in the free surface angle which confirms an S-shaped free surface.

In a similar approach to Zik et al. (1994), Puri and Hayakawa (1999) developed a 2D phenomenological model based on a time-dependent order parameter field −with friction as a central tenet− that appears to predict standard experimental results by Nakagawa (1994). The extension of the friction mechanism to include sidewall effects (end-caps at axial positions $+W/2$ and $-W/2$ from the centre of the drum, length W) was proposed by Taberlet et al. (2003) and Taberlet et al. (2006). Using a balance of momentum for the flowing layer, an approximate linear scaling law linking the local free surface angle (θ), the flowing layer depth (x_0) and the drum width was proposed:

$$\tan(\theta) = \mu_i + \left(\frac{x_0}{W}\right)\mu_w, \tag{2.4}$$

where μ_i is the internal Coulomb friction coefficient that relates the shear and normal stresses at the base of the flowing layer and μ_w accounts for particle-sidewall interactions. Combining the linear scaling with a flux balance between the flowing and rising bulk regions under the assumption of constant shear rate $B = a\sqrt{g/d}$ in the flowing layer, where d is the particle size and $(a = 1)$ an arbitrary constant, produces models for the free surface depth, equation (2.5), and free surface, equation (2.6).

$$x_0(X) = \left[\frac{\omega}{B}\right]^{1/2}\left[R^2 - X^2 - Y_s^2\right]^{1/2}, \text{ and} \tag{2.5}$$

$$\frac{\partial Y_s}{\partial X} = \mu_i + \frac{\mu_w}{W}\left(\frac{\omega}{B}\right)^{1/2}\sqrt{R^2 - X^2 - Y_s^2}, \tag{2.6}$$

where $\tan(\theta) = \frac{\partial Y_s}{\partial X}$ denotes the local slope to the free surface. The extra parameters (B, μ_i, and μ_w) allow solutions for the boundary conditions given in figure (2.6) to be tuned towards either solution. For example, choosing $\mu_i = 0.3$, $\mu_w = 0.52$, and $B = 22$ matches the solution according to Tordesillas and Arber (2005), while setting $\mu_i = 0.25$, $\mu_w = 0.53$, and $B = 10.5$ produces a solution closer (but not exactly) to the implicit curve. Orpe and Khakhar (2007) obtained a similar result by combining the averaged Cauchy equations along the length of the drum with streakline photographic measurements of the bed repose.

2.4 Towards a granular rheology

While the above approaches capture the qualitative features of granular flow within a rotating drum, the absence of a clear rheological description has limited their value. Fortunately progress towards a constitutive law for dense granular flow has emerged in the last decade. Using dimensional analysis of discrete simulation data, da Cruz et al. (2005) showed that the shear stress (τ) verifies a friction law with the resulting friction coefficient (μ) being dependent on a single dimensionless parameter, the *Inertial number* (I):

$$\left|\frac{\tau}{P}\right| = \mu(I) \qquad \text{with} \quad I = \frac{|\dot{\gamma}|d}{\sqrt{P/\rho_m}}, \tag{2.7}$$

where $|\dot{\gamma}|$ is the norm of the shear rate and (P) the confining pressure. By prescribing the inertial number within a homogeneous state, two fundamental dimensionless quantities, the volume concentration (ϕ) and effective friction coefficient (μ), were found to vary linearly with inertial number:

$$\phi(I) = \phi_{max} - aI, \tag{2.8}$$

$$\mu(I) = \mu_{min} + bI \tag{2.9}$$

where $\phi_{max},\ \phi_{min},\ a,\ b$ are constants. Interestingly, the inertial number is also the square of the Savage number or Coulomb number [Savage (1984) and Ancey et al. (1999)].

Midi (2004) used data from different flow geometries to provide a physical interpretation of the inertial number in the dense flow regime ($I > 0.01$): the ratio of the inertial time of rearrangement (confinement time which relates to the confining pressure) $t_{mic} = d\sqrt{\rho_m/p}$ to the time of strain (shear rate or deformation time) $1/\dot{\gamma}$ between contiguous flowing layers of granules. Consistent with the dimensional analysis of da Cruz et al. (2005) the solids concentration ϕ and dimensional stress $\left|\frac{\tau}{P}\right| = \mu$ must be slaved to the inertial number such that the resulting granular flow is completely determined by $\mu(I)$ and $\phi(I)$.

[Jop et al. (2005) and Pouliquen et al. (2006)] showed that equation (2.7) is compatible with their experimentally determined basal friction law [Pouliquen (1999) and Pouliquen and Forterre (2002)] for the choice

$$\mu(I) = \mu_{min} + \frac{(\mu_{max} - \mu_{min})I}{I_0 + I}, \tag{2.10}$$

where $I_0 = 0.279$ is a constant determined by Jop et al. (2005) and (μ_{min} and μ_{max}) are respectively constants relating to the minimum and maximum friction coefficients that bound steady flow. The corresponding functional form of $\phi(I)$ was observed to be linear and fitted as

$$\phi(I) = \phi_{max} + (\phi_{min} - \phi_{max})\, I \tag{2.11}$$

with typical constants given by $\phi_{max} = 0.6$ and $\phi_{min} = 0.4$. Jop et al. (2005) then included this simple rheology, equations (2.7 and 2.10), into the momentum balance equations of surface

flows on heaps (inclined at angle θ to the horizontal) with side walls to obtain equation (2.12).

$$\tan(\theta) = \mu(I(x)) + \mu_w \left(\frac{x}{W}\right), \tag{2.12}$$

where $\mu\left(I(x)\right)$ is given by equation (2.10) with $I(x) = |\dot{\gamma}(x)|\, d/\sqrt{\phi g x \cos\theta}$ now dependent on depth (x) below the free surface of the heap, $\tan(\theta)$ characterises the total effective friction coefficient that accounts for sidewall and internal frictional effects and W is the width of the heap. Figure (2.8) illustrates the new friction law described by equation (2.12) using measured (via PEPT) angles that bound steady flow ($\theta_{\min}$ and $\theta_{\max}$) in tumbling mill experiments conducted in the present thesis and I_0 is similar to that proposed by (Jop et al., 2005).

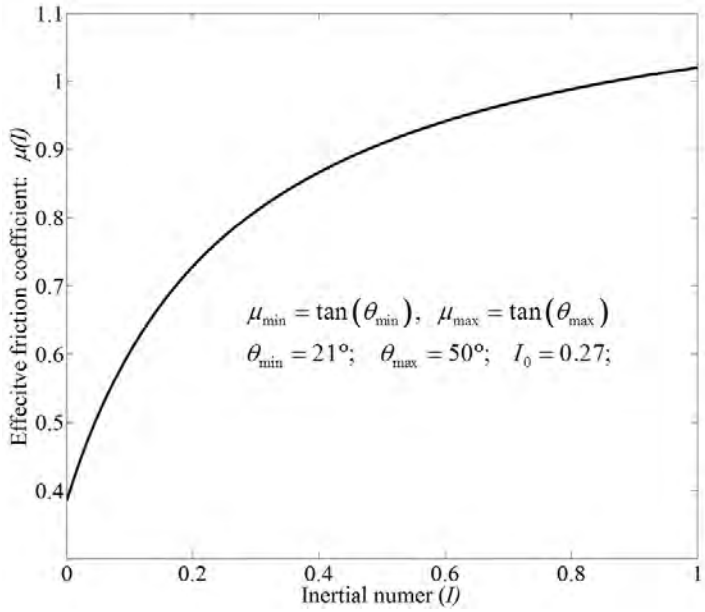

Figure 2.8: Variation of the effective friction coefficient $\mu(I)$ with inertial number as proposed by Jop et al. (2005) for rotating drum data employed in this thesis.

The 3D generalisation of the friction law proposed by Jop et al. (2006) can be summarised in terms of the deviatoric stress tensor τ_{ij} and deviatoric strain rate tensor $\dot{\gamma}^d_{ij}$ under the assumptions that:

(i) small variations of the volume fraction (ϕ) can be neglected (implying that the flow is incompressible), and

(ii) τ_{ij} and $\dot{\gamma}^d_{ij}$ are collinear.

$$\tau_{ij} = \mu\left(I\right) \frac{P}{|\dot{\gamma}^d|} \dot{\gamma}^d_{ij} \qquad \text{with} \quad I = \frac{|\dot{\gamma}|\, d}{\sqrt{\frac{P}{\rho_m}}}, \tag{2.13}$$

where $\tau_{ij} = \sigma_{ij} + P\delta_{ij}$ is the deviatoric part of the stress tensor, $\dot{\gamma}_{ij} = \frac{1}{2}\left(\partial_i \mathrm{v}_j + \partial_j \mathrm{v}_i\right)$ the strain

rate tensor, $\left|\dot{\gamma}^d\right| = \sqrt{\frac{1}{2}\dot{\gamma}_{ij}\dot{\gamma}_{ij}}$ the norm of the deviatoric part $\dot{\gamma}^d_{ij} = \dot{\gamma}_{ij} - \frac{1}{2}\dot{\gamma}_{kk}\delta_{ij}$, $P = \frac{1}{2}\sigma_{kk}$ the local pressure and v_i the components of the velocity.

Flow image analysis studies performed by Chou and Lee (2009) and Orpe and Khakhar (2007) along the midsection of rotating drum flows spanning rolling-to-cataracting successfully recovered the $\mu(I)$-rheology for $I = \dot{\gamma}\sqrt{\frac{d}{g\cos(\theta)}} \in (0;\ 1)$ with the free surface slope $\tan(\theta) = \mu(I)$. Pignatel et al. (2012) also used flow image analysis on rolling mode flows in rotating drums to characterise the $\mu(I)$-rheology in the presence of lateral wall friction. Difficulties in measuring the pressure and parameters relating to the effective $\mu(I)$-rheology led them to approximate the total friction coefficient by the slope to the free surface at midsection and the inertial number by $I = \dot{\gamma}t_{ff}$, where t_{ff} is a derived characteristic time scale which they interpreted as the free fall time scale with no drag. The results showed disagreement with the expected shape of the $\mu(I)$-rheology which they attributed to significant wall friction and a logarithmic decay of the stream-wise velocity that does not satisfy the constant shear rate assumption of the $\mu(I)$-rheology unless non-local extensions are considered, Kamrin and Kovall (2012).

Consistent with the assumptions governing the tensorial formulation, an appropriate procedure for testing the constitutive relation describing the rheology entails plotting $\left[\frac{\tau_{xz}\left|\dot{\gamma}^d\right|}{\dot{\gamma}^d_{xz}P}\right]$ against the inertial number $\left[I = |\dot{\gamma}|\, d/\sqrt{P/\rho_m}\right]$ across the entire granular flow field and checking whether it follows the form of equation (2.12).

By invoking the univocal relation for the volume concentration as stipulated by the dimensional analysis of Midi (2004), assumption (i) can be relaxed without affecting the consistency of the $\mu(I)$-rheology. It is useful to note that other univocal relations have had equal success in describing an effective frictional rheology. In particular, Hatano's (Hatano, 2007) dilatancy law: $\phi = \phi_0 - aI^b$ where $a = 0.11$, $b = 0.56$ and $\phi_0 = 0.6$, has been employed by Lee and Huang (2012) to described a three dimensional flow down an inclined plane that exhibited additional kinetic stresses.

Testing the resulting form of $\left[\frac{\tau_{xz}\left|\dot{\gamma}^d\right|}{\dot{\gamma}^d_{xz}P}\right]$ against the inertial number $\left[I = |\dot{\gamma}|\, d/\sqrt{P/\rho_m}\right]$, is now borne entirely by assumption (ii).

The collinearity assumption −assumption (ii)− is obvious for the unidirectional flows encountered down inclined planes and heaps; however, it breaks down for multidirectional flows, like the rotating drum [(Cortet et al., 2009)]. In light of multidirectional flow within rotating drums, [(Cortet et al., 2009)] expanded the test requirements of the rheology to include:

(i) $\frac{|\tau|}{P} = \mu(I)$,

(ii) τ_{ij} and $\dot{\gamma}^d_{ij}$ have identical principal directions.

According to Cortet et al. (2009) condition (ii) is naturally satisfied in unidirectional flows (like the inclined plane and heap flow) so verifying equation (2.13) reduces to verifying condition (i) only. In multidirectional flows, like that encountered in rotating drum flows, Cortet et al. (2009) calculated the angular difference ($\delta\theta$) between the principal directions of τ_{ij} and $\dot{\gamma}^d_{ij}$ to test the collinearity demanded by condition (ii). He found that ($\delta\theta$) ranges from $\pm 10^\circ$ for inertial numbers ($5 \times 10^{-4} < I < 5 \times 10^{-2}$), corresponding to the "liquid" surface flows,

and up to 35° in the deeper part of the flow, corresponding to smaller inertial numbers $(5 \times 10^{-6} < I < 5 \times 10^{-4})$. He therefore concluded that the constitutive relations proposed in equation (2.13) fails the collinearity test over the whole range of inertial number. This conclusion is further supported by the important dispersion that results from plotting $\left[\frac{\tau_{xz}|\dot{\gamma}^d|}{\dot{\gamma}^d_{xz}P}\right]$ against the inertial number $\left[I = |\dot{\gamma}|\, d/\sqrt{P/\rho_m}\right]$; see figure (2.9). Even when the analysis was restricted to data taken along the center of the drum, an unexpected kink in the curve, figure (2.9d), shows that the proposed rheology fails even along the (assumed) well-behaved central region.

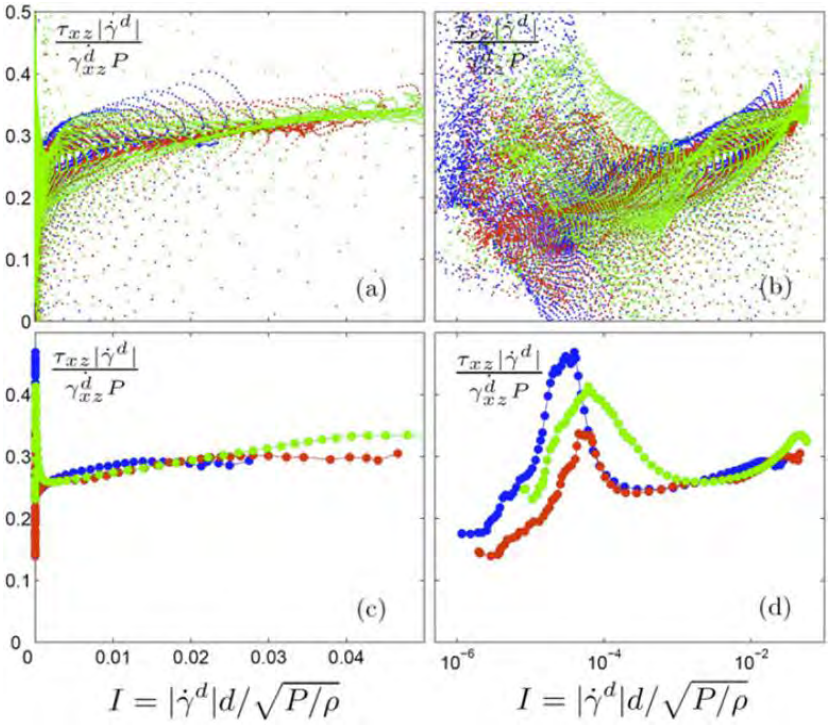

Figure 2.9: Effective friction coefficient as a function of inertial number for three drum rotation rates: Ω = 12rpm (green points), Ω = 6rpm (red points) and Ω = 2rpm (blue points). (a) illustrates the ratio for the entire flow field with (b) showing the same plot for a logarithmic inertial number scale. (c) shows the ratio along the central region of the drum and (d) is the equivalent plot on a linear-log scale. Figures taken directly from Cortet et al. (2009).

Interestingly, the norm of the stress ratio $\frac{|\tau|}{P} = \mu(I)$ follows the frictional rheology described by equation (2.12) for the inertial range $I > 10^{-4}$ with a hysteresis-type jump just below $I = 10^{-4}$. The hysteresis effect is well-known [Forterre and Pouliquen (2008)] for rotating drum flows and highlights a clear limitation of the Jop-rheology to capture the phase transition from solid-like flow to liquid-like flow. Lee and Huang (2012) addressed this limitation by employing rate-independent and rate-dependent components for static and kinetic contributions of the shear stress respectively within a depth-averaged formulation consistent with the Saint-Venant hydrodynamic description. The granular kinetic theory of Jenkins and Richman (1985) was used for the kinetic parts while the static components conformed to the friction law of Jop et al. (2006) and the dilatancy law of Hatano (2007). For a range of effective restitution values as suggested by Jenkins and Zhang (2002), the hysteresis at flow initiation (first turning point

in figure (2.10)) and the transition from liquid-like flow to gas-like flow (second turning point in figure (2.10)) was successfully captured. The authors acknowledge that the discontinuity at the transition to the inertial flow regime (second turning point in figure (2.10)) warrants further study. We note here −deferring details to chapter (4)− that smooth phase transitions are captured in the models developed in this thesis.

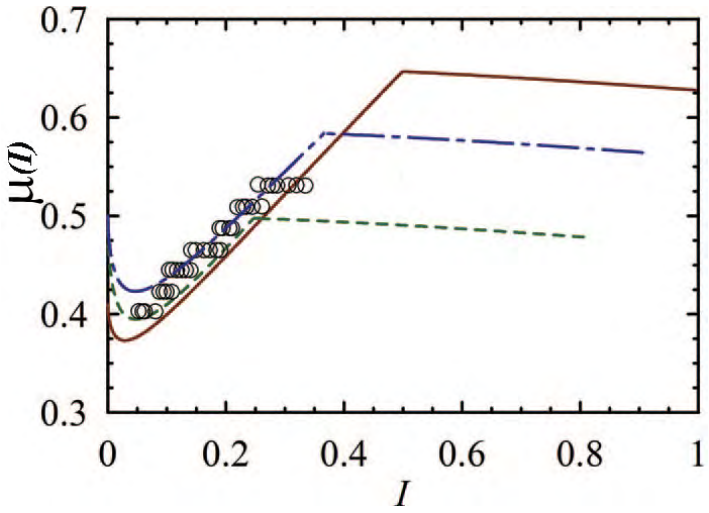

Figure 2.10: Variation of the effective friction coefficient with inertial number. The lines are model predictions for three different effective restitution coefficients while the open circles correspond to the data from Midi (2004). Figure taken from Lee and Huang (2012).

2.5 Summary

In this chapter we have reviewed granular flow in rotating drum systems. Non-invasive measurements in rotating drums have clearly identified a range of scaling relations that contradict current model predictions of the same. The rich co-existence of flow regimes are clearly prevalent in rotating drums, especially when realistic conditions (like tumbling mills) are considered. Again, no current models satisfactorily captures all the observed flow regimes. While the new rheology of Jop et al. (2006) is a major step forward in describing dry granular flows, it does not cope well with the very low and very high inertial numbers. In particular, it fails to capture the hysteresis between the three flow regimes that delineate granular flows. This poses a severe limitation when dealing with systems like tumbling mills that can span all three regimes when cataracting conditions prevail. Despite these limitations, the 3D tensorial formulation of Jop et al. (2006) −which is akin to well known visco-plastic rheologies like the classical Bingham or Herschell-Bulkley fluids− has greatly facilitated the ability to describe the various flow regimes. In this regard, the model of Lee and Huang (2012) is particularly interesting and forms the basis for this thesis.

Chapter 3

Experimental and Data Analysis

The experimental program and analysis schemes undertaken are reported herein. Section (3.1) describes the application of Positron Emission Particle Tracking (PEPT) to tumbling mill flows with further details on the theory of positron annihilation, PEPT and scintillation detectors given respectively in Appendices (A, B and C). Section (3.2) describes the analysis schemes employed to recast the measured coordinates of the single representative tracer ($x_p,\ y_p,\ z_p,\ t_p$) into time-averaged kinematics and distributions amenable to continuum-type modelling. Also included in section (3.2.2) are the important scaling relations and assumptions −derived directly from measurement− that ultimately inform the assumptions employed in the granular rheology models developed in chapter (4).

3.1 The Positron Emission Particle Tracking (PEPT) Technique

Positron Emission Particle Tracking (PEPT) is a non-invasive 3D imaging technique that tracks the motion of a representative grain (the tracer) that has been radio-labelled with a positron emitting radionuclide and allowed to move within the field of view (FoV) of a modified Positron Emission Tomography (PET) scanner. Decay by β^+ emission is quickly followed by annihilation with an electron, producing a pair of 511 KeV back-to-back gamma rays that define a line of response (LoR) passing through (or very close to) the tracer. A chronological series of coordinate pairs mostly corresponding to the endpoints of the LoRs constitutes the raw data. A selection of LoRs are then triangulated into grain coordinates ($x_p,\ y_p,\ z_p,\ t_p$) [Hawkesworth et al. (1986) and Parker et al. (1993)] and constitute the measured data for studying granular flow. Figure (3.1a) is a 2D illustration of a few such LoRs while figure (3.1b) is actual data obtained over several milliseconds of data sampling. The spurious LoRs are removed using an iterative algorithm −see section (B.1) for details− resulting in a redundant set of lines (in 3D) whose intersection (in the least squares sense) defines the best estimate of the tracers position during the chosen time interval (usually a few milliseconds); see figure (3.1c). Typically, the 3D spatial coordinates of the tracer are accurate to within a millimeter at a temporal resolution of a few milliseconds.

The "EXACT3D" (Model: CTI/Siemens 966) PET scanner employed in this work was de-

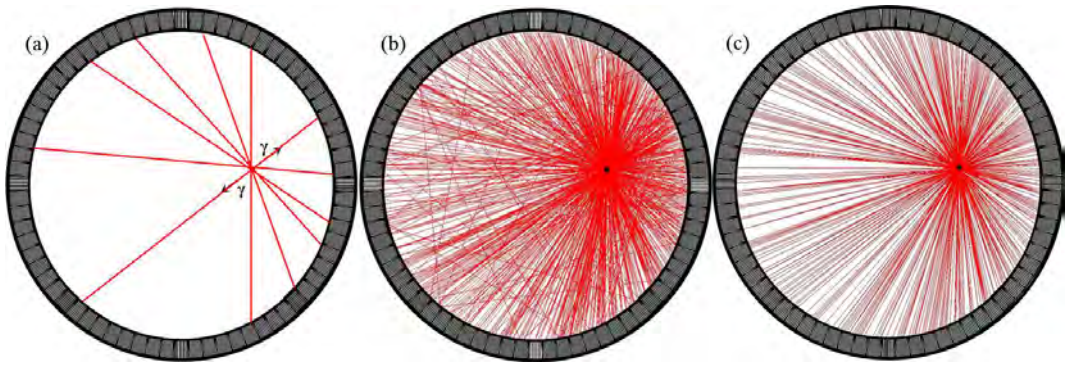

Figure 3.1: (a) Illustration of a selection of lines of response (LoRs) emanating from the tracer particle and terminating on the ring of detector elements. (b) A typical set of LoRs sampled over a few milliseconds. (c) The remaining LoRs after the spurious LoRs have been iteratively removed.

signed with the aim of achieving high sensitivity and resolution using state-of-the-art detectors, figure (3.2). The device consists of 48 rings of standard bismuth germinate detector elements with a usable ring diameter of ≈ 50 cm and an axial FoV of ≈ 23 cm. The I/O and computing hardware can maintain a sustained acquisition rate of up to four million coincidence events per second. The scanner has been used for clinical research at Hammersmith Hospital, London since 1995, and may still be the most sensitive PET scanner in operation today. It is presently housed at the positron imaging facility, PEPT Cape Town, which is located at the South African national accelerator center, iThemba Laboratory for Accelerator Based Science (iThemba LABS).

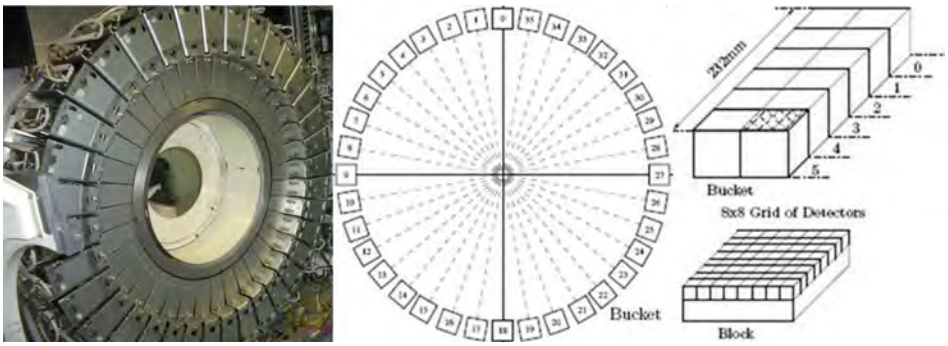

Figure 3.2: The "EXACT3D" PET scanner (left) used at PEPT Cape Town with protective cover removed. The 36 detector buckets (middle), each contain 768 Bismuth Germinate detector elements (right) of area (4.8×4.8) mm^2.

In many PEPT studies the tracer particles are labelled indirectly by attaching a suitable radionuclide to it. In the present study, Ga-68 (half-life of 68 minutes) was adsorbed onto a small resin bead (~ 200 μm) which was then embedded into a representative five millimeter glass bead. Using this method, activities of up to 1.3 mCi was successfully achieved. A tumbling mill with inner diameter $D = 476$ mm and wall thickness of 12 mm was built from high density polyethylene (HDPE; specific density 0.95). The drum was fitted with eighteen aluminium lifter bars and rotated clockwise. The mill was driven axially by a DC drive with a step-down gearbox to achieve the desired mill rotation speeds. Figure (3.3a) shows the experimental tumbling mill within the FoV of the PEPT scanner and figure (3.3b) is a

schematic front view of the drum, illustrating the lifter bar geometry employed in this work.

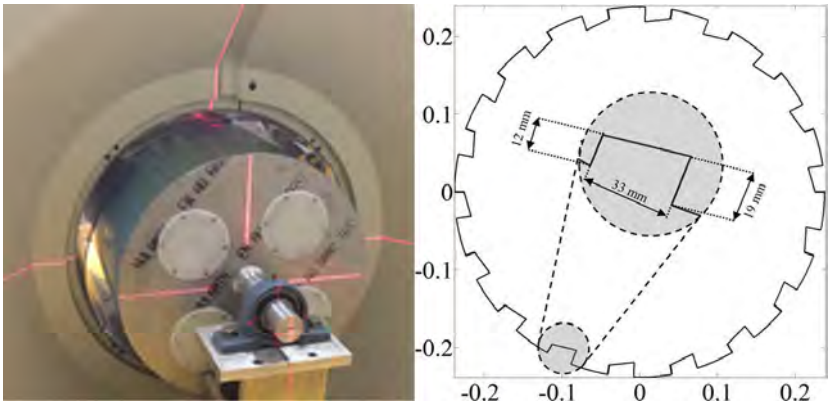

Figure 3.3: (a) Experimental rotating drum within the field of view (FoV) of the PEPT camera. (b) Front view schematic of rotating drum showing the eighteen aluminium lifter bars. The drum was rotated clockwise.

Experiments were performed with mono-sized glass beads of diameter ($d = 5.007 \pm 0.025$ mm) and ($d = 8.004 \pm 0.036$ mm). In both cases the beads occupied 25 % of the drum inner volume. A torque sensor coupled directly to the main drive shaft allowed for direct torque measurements with a near-constant torque indicating that steady flow conditions have been reached. A non-contact, optical tachometer was also used to directly monitor the drum rotation speed which further aided in establishing steady state operation. PEPT data logging only commenced once the torque and speed readings were properly stabilised.

The experimental parameter that was varied in the present work was the mill rotation speed (ω). Two hours worth of data per drum rotation rate was recorded in six twenty minute runs after steady state flow was reached. After each twenty minute recording of data, the drum was stopped and the glass beads remixed. The remixing process ensures that the tracer covers all possible regions of the available granular flow field. In mineral processing the rotation rate of the drum is often expressed as a fraction of the critical speed: The critical speed is the rotational speed at which the outermost layer of granular material begins to centrifuge. It is defined, in revolutions per minute (rpm), by Rose and Sullivan (1957) as:

$$N_c = \frac{1}{2\pi}\sqrt{\frac{2g}{D-2r}} \tag{3.1}$$

where D is the inner diameter of the rotating drum and $r = d/2$ is the radius of a grain in the bed. In the limit that $r \ll D$, which is typical in industrial tumbling mills, the critical speed is usually approximated (in rpm) as:

$$N_c \approx \frac{42.3}{\sqrt{D}}. \tag{3.2}$$

The drum speeds, as a percentage of critical speed $\left(\frac{100\times\text{mill rpm}}{N_c}\right)$, employed in this work were $40 : 5 : 75$ %.

3.2 Data pre-processing

The Lagrangian trajectory data (x_p, y_p, z_p, t_p) determined in the laboratory frame was rotated into the drum coordinate system (the drum center), interpolated uniformly in time, differentiated (twice if necessary) and then recast into 2D trans-axial ensemble averages (per voxel) on the assumption that the system is ergodically represented [Wildmann et al. (2000)] by the single tracer, i.e. the time-averaged quantities (per voxel) derived from a single tracer are equal to the ensemble average (per voxel) of the steady state system. After discretizing the azimuthal plane into a $n \times n$ grid (n^2 is the number of grid cells whose size is usually chosen according to the length scale of the granular flow model being investigated) centered on the mill, the time averaged quantities are then computed within each representative volume element (RVE) of volume $V_{rve} = (D/n \times D/n \times W)$, where W is the drum length and D its diameter. The resultant average per RVE thus determined includes all data along the length of the mill that lies within the volume spanned by the RVE.

To apply continuum mechanics approximations to discrete particle systems like tumbling mills requires a fundamental notion of a mesoscopic volume element. The choice of this RVE must be small compared to the macroscopic length of the flow. Rycroft et al. (2009) use the length of shear banding observed by Midi (2004) to argue that an RVE length of $3d - 5d$ (d is the particle diameter) is reasonable for all but the very exotic flows where the dynamical correlation length can change. Intuitively, the time scale (T) should also be important to the flow description. It therefore seems reasonable to use the average number of particles (N_T) passing through an RVE during time interval ($t = T$) to inform the selection and appropriateness of the RVE size to continuum modelling. For example, consider an RVE such that $D/n = d$. Then under steady flow conditions and assuming spherical particles, the simple view suggests that the maximum number of particles that can be contained in the RVE is $N_s = W/d$. However, for particles passing through the RVE (through the shortest side as is expected for tumbling mills where the flow is predominantly azimuthal) in a time $t = \langle\dot{\gamma}\rangle^{-1}$, where $\dot{\gamma}$ is the shear rate and $\langle\rangle$ denotes an average, the average number of particles passing through the RVE is $N_T = \frac{\langle v\rangle nW}{D\langle\dot{\gamma}\rangle d}$, where $\langle v\rangle$ denotes the average velocity in the mill. Using $n = 100$, $D = 0.476$ m, $\langle v\rangle = 0.6$ ms^{-1}, $\langle\dot{\gamma}\rangle = 9.7$ s^{-1} and $W = 0.480$ m (data within 10 mm from the axial end-walls were excluded) gives $N_T = 1247$ and $N_s = 96$ for 5 mm beads and $N_T = 779$ and $N_s = 60$ for 8 mm beads. We note here that the values of $\langle v\rangle = 0.6$ ms^{-1} and $\langle\dot{\gamma}\rangle = 9.7$ s^{-1} are average values determined across the all pept data set employed in this work. An RVE volume with dimensions $(5 \times 5 \times 480)$ mm^3 was thus considered acceptable for the current PEPT analysis.

3.2.1 Residence time binning

Consider the illustrative trajectory shown in figure (3.4a). It consists of a series of PEPT-derived triangulated points (or simply sample points) along a path in 2D space, shown here as a dashed line (the sample trajectory). The sample trajectory is obtained by fitting a second order Lagrange interpolation polynomial to the sample points. Kinematics of the tracked particle can be obtained by differentiating the piecewise polynomials making up the sample trajectory. In order to recast this information into an Eulerian description of the entire system (i.e. the ensemble) we discretise the space into sample volumes (RVE's) and

average the information associated with the segment of the sample trajectory (the sample segment) that passes through the RVE. We note here for clarity that the average is composed of many segments corresponding to many transits of the tracer through the RVE over the long-time duration of the experiment. Figure (3.4b) shows a 2D grid of bins superimposed on the sample trajectory of figure (3.4a). For the rest of this discussion, we will consider the case of 2D binning, but in general this procedure can be applied in 3D.

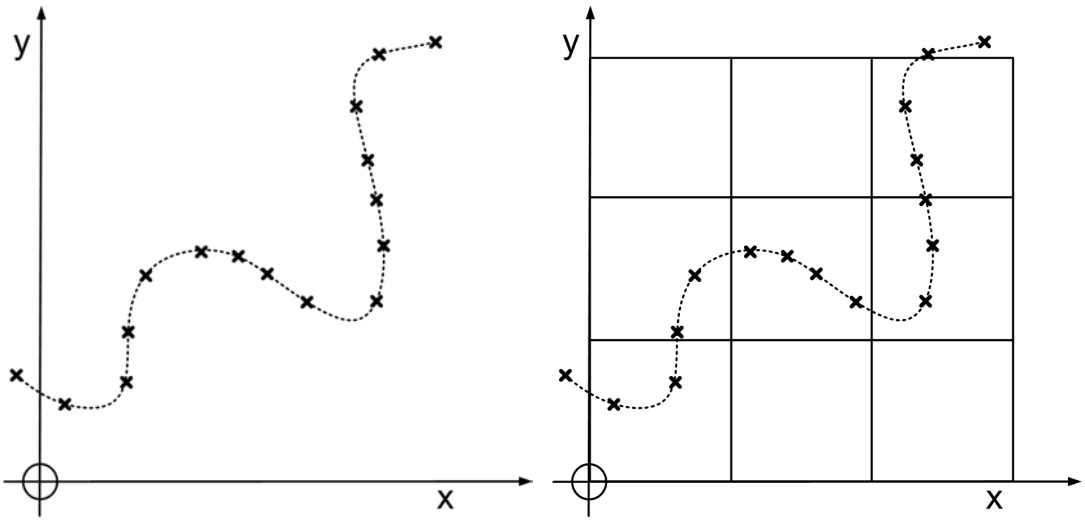

(a) 2D trajectory (b) Superimposed grid

Figure 3.4: An illustrative trajectory in 2D space without (left) and with (right) a binning grid superimposed.

Once the grid has been assigned, the sample points are replaced by the sample trajectory. In particular the times corresponding to the entry and exit points of each sample segment can be calculated, allowing for the estimation of the total time spent $t(k) = \sum_{j=1}^{M} t_j$ in each RVE (denoted by k); M denotes the total number of transits made by the tracer through the k^{th} RVE and j denotes the j^{th} transit. The ergodic assumption then allows the total time spent by a tracked particle in each RVE, normalised to the total duration of the experiment T, to be interpreted as the probability that a particle of that class will be found in that bin at any given instant. The distribution of normalised times spent in each bin is called the probability distribution or residence time distribution (RTD) and given as $F(k) = t(k)/T$. Figure (3.5a) illustrates the times associated with the sample segment endpoints for a single transit through the RVEs and figure (3.5b) is the corresponding Eulerian grid of the residence time per RVE.

Mathematically, the time-averaged x-velocity for a transit j through a given bin is easily shown to be

$$\bar{v}_{x,j} = \frac{x(t_f) - x(t_i)}{t_f - t_i} \tag{3.3}$$

where $x(t) = p_x t^2 - q_x t + r_x$ denotes the second order polynomial. The corresponding time-

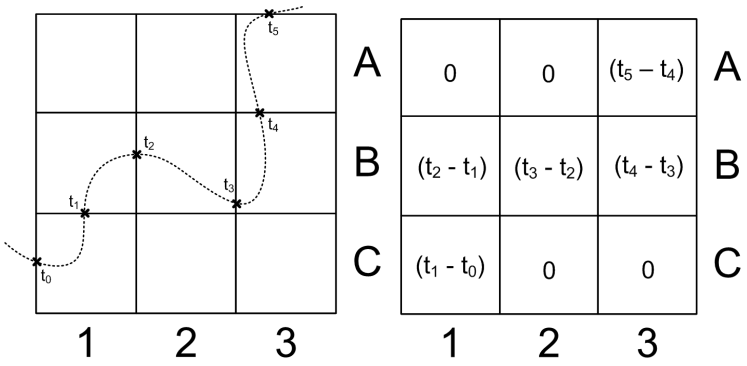

(a) Binned trajectory sampled at bin crossings

(b) Residence times

Figure 3.5: The residence time binning procedure: calculating bin boundary crossing times (left) and thus bin residence times (right).

weighted average x-velocity for each of its N passes through a given bin then yields

$$\bar{v}_x = \frac{\sum_{j=1}^{N}\{x_j(t_f) - x_j(t_i)\}}{T}. \tag{3.4}$$

The time-weighted average of a tracked particle's continuously time-averaged velocity in a given bin is thus very simply given as the sum of the differences between the particle's positions upon entering and then leaving that bin, divided by the total time over which it was tracked.

A similar procedure for the particle's continuous time-averaged x-acceleration yields

$$\bar{a}_{x,j} = 2p_x \tag{3.5}$$

with a corresponding time-weighted average of

$$\bar{a}_x = \frac{2\sum_{j=1}^{N}\Delta t_j p_{x,j}}{T}. \tag{3.6}$$

Wildmann et al. (2000) showed that the RTD (in the k^{th} RVE) is directly proportional to the volume fraction $\phi(k)$ which is given by:

$$\phi(k) = \frac{\pi}{6}\frac{Nd^3}{V_{rve}}F(k) \tag{3.7}$$

where N is the total number of particles in the drum and the other terms are as previously defined.

3.2.2 Time-averaged data

The methodology described in the previous sections were applied to both the 5 mm and 8 mm glass beads. The resulting Eulerian fields form the basis for developing continuum-type modelling. The 5 mm glass bead configuration operated at 55% of critical speed is used to illustrate the 100×100 Eulerian grids and associated analyses that ultimately influence the modelling assumptions employed in chapter (4).

The velocity field, arguably the most important kinematic quantity for continuum-type modelling, is shown in figure (3.6). The high quality velocity field data facilitated the identification of the equilibrium surface (ES): The surface that separates the rising material from the flowing layer; see section (2.2.2) of the literature review for more details.

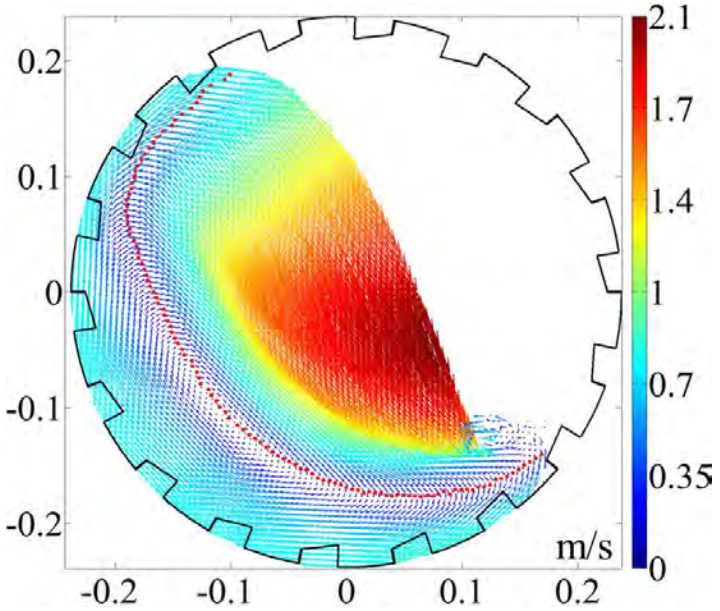

Figure 3.6: Time averaged velocity field of 5 mm glass beads operated at 55% of critical speed. The red dotted curve denotes the surface of zero velocity −termed the equilibrium surface (ES)− that separates the rising en-masse material from the flowing and cataracting layers.

Of equal importance to granular flow modelling is the volume concentration map, as defined by equation (3.7) for PEPT data, shown in figure (3.7a). Applying an edge detection scheme [Canny (1986)] to the resulting solids concentration map allows for the determination of the free surface profile (FS) − dashed line in figure (3.7a). A smoothing spline curve was fitted to the ES data (red dots in figure (3.6)). Figure (3.7a) shows the smoothing spline fit as a dashed-dotted line superimposed on the volume concentration map. The solid lines connecting the FS and ES illustrates the depth of the flowing layer and is measured orthogonal to the free surface. To facilitate the ensuing discussion, Figure (3.7b) shows the ES, FS, selected depth profiles, and a local coordinate system with origin located at the FS such that $\hat{t}$ is parallel to the FS and $\hat{r}$ is perpendicular to the FS and hence directed along the solid line that denotes the depth.

The flowing layer has received much attention in the physics literature [Parker et al. (1997), Midi (2004), Pignatel et al. (2012), Orpe and Khakhar (2001), Felix et al. (2007)]. In addition

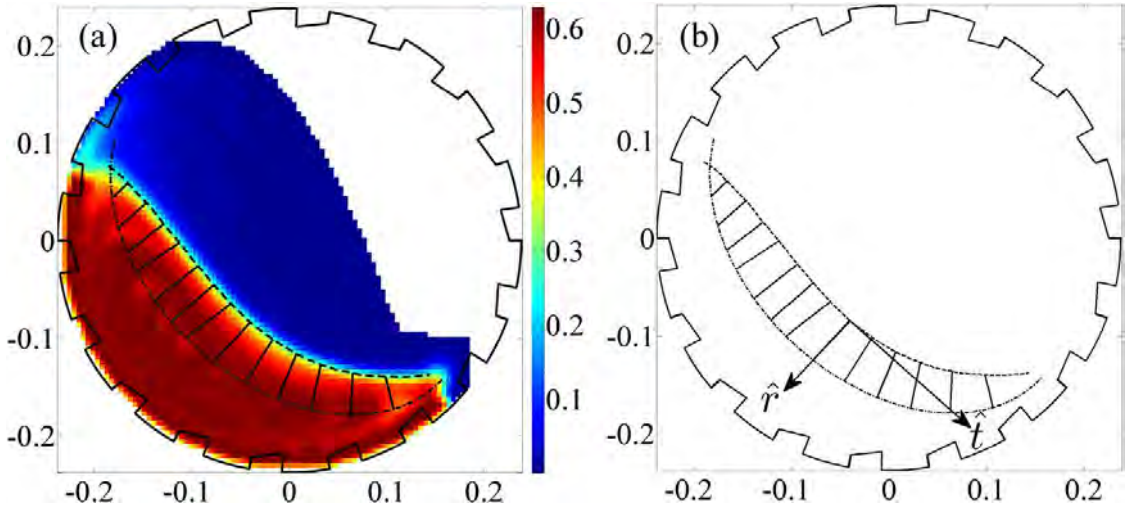

Figure 3.7: (a) Time averaged volume concentration (ϕ) of 5 mm glass beads operated at 55% of critical speed. The black dashed line denotes the free surface profile while the black dashed-dotted line delineates the equilibrium surface. The black solid lines connecting the ES and FS denotes the depth of flowing layer. (b) shows the same depth profile relative to the local coordinate system.

to the lack of a clear scaling law between the flow rate and flowing layer depth (see section (2.2.1) for discussion on scaling), all reported scaling relations are obtained indirectly as follows: For slowly rotating drums with no cascading or cataracting motion, the flux per unit length of the flowing layer $Q_f = \langle v_t \rangle h$, where v_t is the component of the velocity tangent to the free surface. By assuming that the rising region (below the ES) is plug flow and that the square of the depth $h^2 \ll R^2$ (R is the drum radius), the flux in the rising region is easily shown to be $Q_r = \left(\frac{\omega}{2}\right) R^2$. Continuity then allows balance between the flux terms ($Q_f = Q_r$) and $\langle v_t \rangle h \propto \omega$ follows naturally. Subsequent measured correlations between h and ω then facilitate scaling laws between $\langle v_t \rangle$ and h. In this regard Midi (2004) used a wide range of data to obtain the scaling: $\langle v_t \rangle \propto h$. In the present work, the PEPT-derived v_t-profiles shown in figure (3.8) allowed for direct computation of the re-scaled flow rate $Q^* = \frac{\langle v_t \rangle h}{d\sqrt{gd}}$. It is useful to point out that the flow rate calculations performed in this work are not limited to the central region of the flowing layer, as is commonly encountered in the literature, but span the entire layer. In our analysis the flowing layer is discretised into 13 slices as shown in figure (3.8). Plotting $\sqrt{Q^*}$ against the scaled depth $\left(\frac{h}{d}\right)$ for all slices, drum speeds and particle sizes then allows for the testing of the underlying scaling relation. As observed in figure (3.9), the best fitting power law $\left[\sqrt{Q^*} = a\left(\frac{h}{d}\right)^m\right]$ yields $m = 0.86 \pm 0.04$. We note that while our result is close to Midi (2004) (who get $m = 1$), the two results are clearly statistically different. To an order of magnitude approximation, it might be tempting to assume $m = 1$ and in so doing yield a very simplistic result for the shear stress: $\tau =$ constant; however, all literature stress measurements to date suggest otherwise. To avert temptation entirely, we are also reminded of the measurements by Ancey (1999) for steep slopes (as is encountered in this work): $1 < m < 2$. Now assuming that not all the literature is simply wrong, the only logical alternative is to assume that the underlying rheology is likely comprised of multiple flow regimes that interact complexly. We will explore this notion more thoroughly with our PEPT data in the next chapter. Notwithstanding, if we assume a linear scaling, then the

resulting shear rate $\langle\dot{\gamma}\rangle \approx 0.25\sqrt{\frac{g}{d}}$; cf. Midi (2004) who get $\langle\dot{\gamma}\rangle \approx 0.5\sqrt{\frac{g}{d}}$.

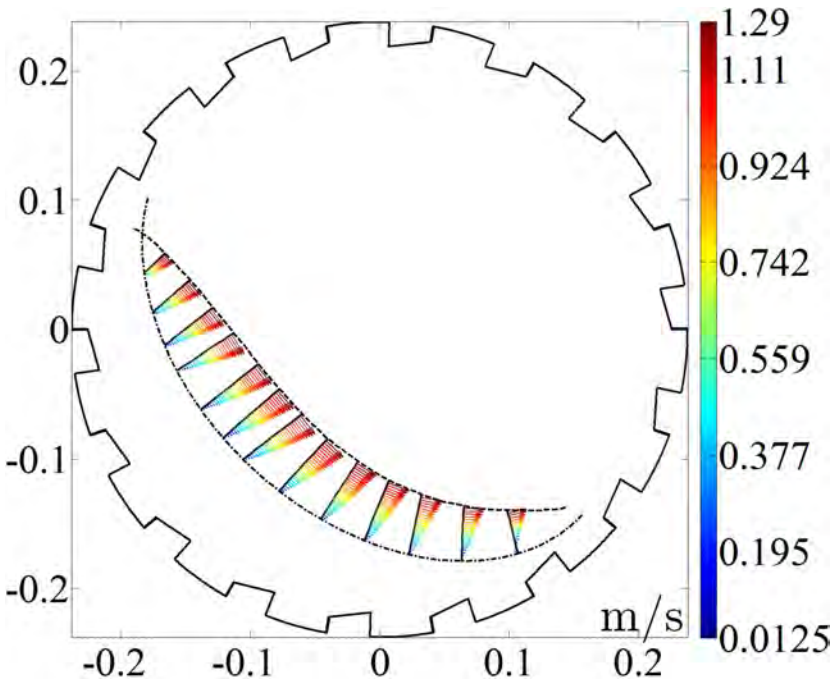

Figure 3.8: PEPT-derived tangential velocity profiles (v_t) taken along the entire flowing layer depth. The orientation of the depth profile measurements are described in figure (3.7b).

Finally, noting that $\frac{D}{d} = \frac{476}{5} = 95.2 \approx 100$ for the 5 mm diameter glass bead data, experiments by Felix et al. (2007) for $\frac{D}{d} = 100$ yields a scaling of $\langle v_t\rangle \propto h^m$ where $m = 5.5 \pm 0.5$. The big differences between the various published scaling relations clearly highlights the need for further experimental work and modelling of rotating drum flows. Table (3.1) summarises the various scaling relations obtained for rotating drum flows.

Author	**Scaling: $\langle v\rangle$ versus h**	**$\lvert\dot{\gamma}\rvert$ estimates**	**Comments/Definitions**
Parker et al. (1997)	$\langle v\rangle \propto h^0$	≈ 0	excessive wall slip
Orpe and Khakhar (2001)	$\langle v\rangle \propto h^3$	$\sqrt{\frac{g\omega}{Md\cos(\theta)}}$	$M \equiv$ fit parameter; $\theta \equiv$ bed repose
Midi (2004)	$\langle v\rangle \propto h$	$\dot{\gamma} \approx 0.5\sqrt{\frac{g}{d}}$	wide range of data
Jop et al. (2006)	$\langle v\rangle \propto h^{3/2}$	depends on Q^*	based on heap flows
Felix et al. (2007)	$\langle v\rangle \propto h^m$	variable	$m = 5.5 \pm 0.5$ for $\frac{D}{d} = 100$
Pignatel et al. (2012)	$\left[\frac{h}{d} = 2.86\left(\frac{\langle v\rangle h}{d\sqrt{dg}}\right)^{0.44}\right] \Rightarrow \langle v\rangle \propto h^{1.27}$	variable	scaling from best fitted power law (all data)
This work	$\langle v\rangle \propto h^{0.86}$	$\dot{\gamma} \approx 0.25\sqrt{\frac{g}{\langle d\rangle}}$	cataracting flows; $m = 0.86 \pm 0.04$; $\langle d\rangle = 6.5$ mm

Table 3.1: Scaling laws for the variation of scaled flow rate ($\sqrt{Q^*}$) with scaled flowing layer depth ($\frac{h}{d}$).

The ratios $\frac{v_r}{(v_t+v_r)}$ and $\frac{v_t}{(v_t+v_r)}$ are shown in figures (3.10a and 3.10b) respectively – v_r is

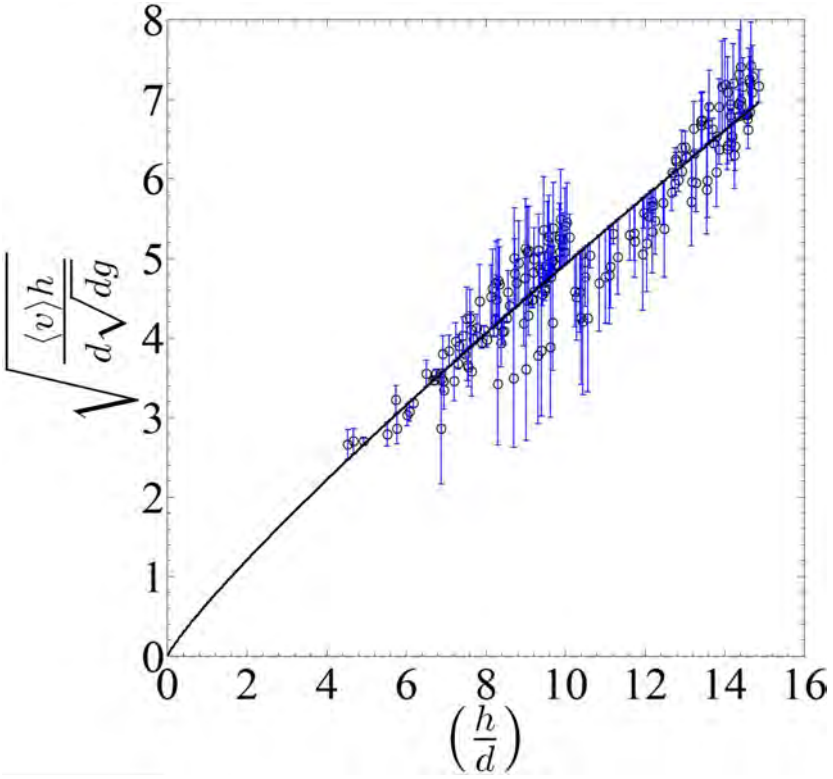

Figure 3.9: Variation of the re-scaled flow rate ($\sqrt{Q^*}$) with scaled depth (h/d) for all drum speeds ($40:5:75\%$ of critical speed) and particle sizes (5 mm and 8 mm diameter beads) investigated in this work. The scaling does work in the sense that all data collapse onto the same curve; however, the form of the collapse does not appear to follow any of the published scaling laws within the uncertainties. Notwithstanding, it can be argued that the scaling is closest to the power law obtained by Midi (2004): $\langle v_t \rangle \propto h$.

negligible except for small regions near the base of the flowing layer closer to the toe and shoulder, and v_t is clearly the dominant component of the velocity. The same result is observed for all drum rotation rates studied in this thesis. It is thus reasonable to assume that $v_r \approx 0$ in any granular flow modelling of the current PEPT data.

3.3 Summary

In this chapter we reported on the PEPT measurement scheme and associated experimental program undertaken to study the flow of granular material in a tumbling mill operated in the cascading and cataracting flow regimes. The Lagrangian data obtained from PEPT triangulation was shown to be suitable for continuum-type modelling with an acceptable RVE size of $5 \times 5 \times 480$ mm^3. The average kinematics per RVE was computed using a second order lagrange interpolation polynomial. The average volume fraction per RVE was computed using the theory developed by Wildmann et al. (2000) for ergodic systems. The velocity and volume fraction distributions facilitated the delineation of the ES, FS, flowing layer depth and associated flow rates. The data conformed to the scaling: $\langle v_t \rangle \propto h^{0.86}$ which is closest to that

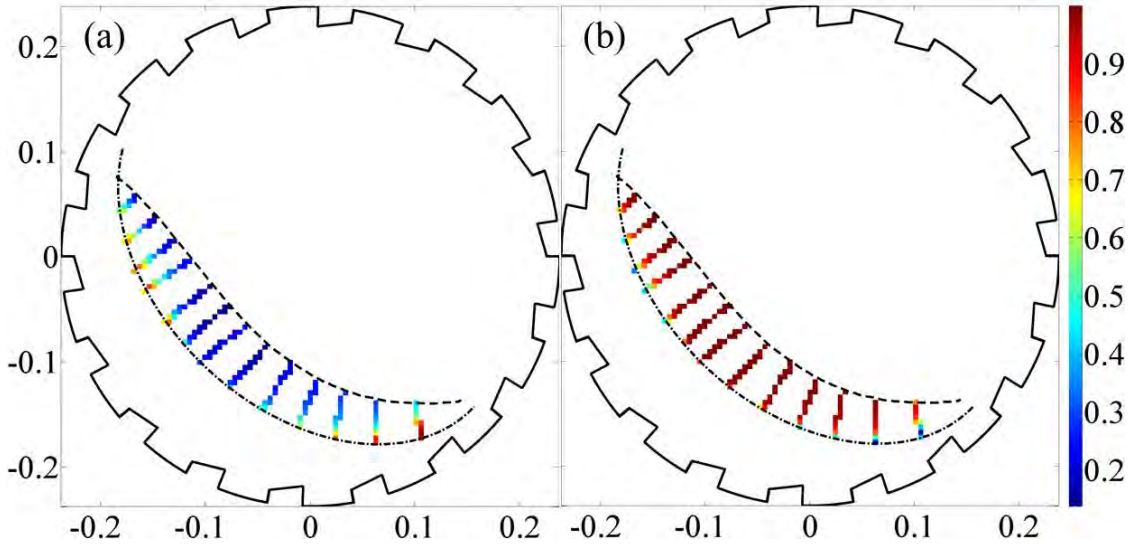

Figure 3.10: Illustrating the relative contributions of v_r and v_t to the velocity profile in the flowing layer. v_r is shown to be negligible except the the very small regions near the toe and shoulder.

obtained by Midi (2004); however, a clear constitutive choice for the shear stress cannot be easily discerned from the data, or indeed the literature. Assuming linear scaling, the average shear rate is given by $\langle\dot{\gamma}\rangle \approx 0.25\sqrt{\frac{g}{d}}$. Finally, the velocity in the flowing layer was shown to be dominated by components parallel to the FS.

Chapter 4

Tumbling Mill Rheology

4.1 Introduction and Motivation

Without a clear route for selecting the constitutive relations governing the shear stress, the only sensible alternative is to identify the relevant flow regimes in the tumbling mill and use the well known literature models to describe them. To this end, we recall that section (2.4) briefly discussed the combination of kinetic and static stresses to yield an effective friction coefficient $\mu(I)$ that successfully captures the known hysteresis between the starting and stopping of steady flows, and the expected transition between the liquid-like (dense) and gaseous-like regime [Lee and Huang (2012)]. The hysteresis in rotating drums corresponds to the difference between starting (θ_1) and stopping (θ_2) repose angles ($\theta_2 < \theta_1$), Forterre and Pouliquen (2008). Intuitively, the second transition from the liquid-like flow (dense regime) to gas-like flow should correspond to a net decrease in the effective friction coefficient given the dilute nature of the flow. This is supported by the fact that the effective friction coefficient described by the kinetic theory of Lun et al. (1984) decreases rapidly for high values of the inertial number where the visco-plastic rheology of Jop et al. (2006) is expected to breakdown. A robust model of the effective friction coefficient should (smoothly) capture these phase transitions. In this regard, while the model of Lee and Huang (2012) is successful in capturing the liquid-gas transition, the sharp discontinuity suggests a deficiency in the description which the authors themselves note as warranting further research. We hypothesise that the inclusion of a turbulent stress and an appropriately chosen description of the solids concentration variation ϕ with inertial number (I) will correct (smooth out) the discontinuity.

Tumbling mills exhibit all three flow regimes. Consider the volume concentration map (ϕ), figure (4.1), constituted by applying equation (3.7) to the PEPT data for the tumbling mill operated at 60% of critical speed. To make more quantitative the ensuing discussion, we limit the analysis to the radial line passing through the central region of the granular bed (black radial line with white labels to facilitate the discussion). Figure (4.2) shows the corresponding plot of ϕ versus normalised drum radius ($\frac{x}{R}$) along the same radial line. As will be noted later in section (4.2.1), coordinate (x) is measured from the free surface; however, given that the radial distance r and depth x coincide through the thickest region of the bed, as shown figure (4.1), $r - x =$ constant. Using either coordinate in the ensuing discussion will therefore not affect the interpretation of profiles. For reasons of numerical convenience we will use

the actual radius (r) in the plots and associated discussions but will refer to it as depth x. Notwithstanding, all calculations involving the depth (x) use the correct value as measured orthogonally from the top of the free surface.

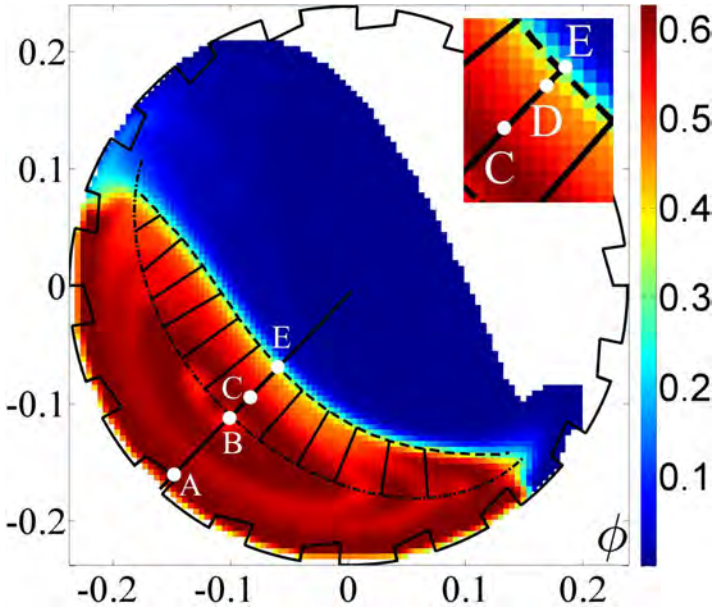

Figure 4.1: Solids concentration variation across the granular bed for the mill rotating at 60% of critical speed. The black solid radial line passes through the thickest region of the flow. Positions A, B, C, D (see zoomed image) and E denote respectively the top of the lifter bars, the ES, the upper limit of the quasi-static regime (or beginning of the dense flow regime), the upper limit of the dense flow regime (or beginning of the purely inertial regime), and the FS.

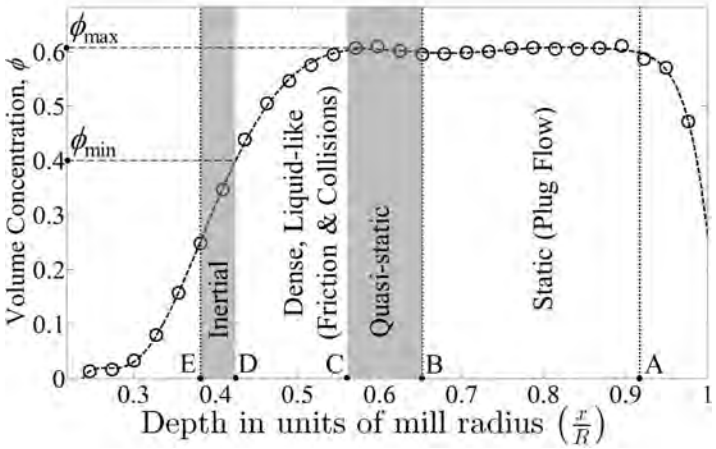

Figure 4.2: Solids concentration variation (ϕ) as a function of normalised (radial) depth $\left(\frac{x}{R}\right)$. The profile is of the black, solid radial line shown in figure (4.1). The various flow regimes are clearly delineated. In particular, the dense (liquid-like) regime non-linearly varies from $\phi_{\min} = 0.4$ to $\phi_{\max} = 0.6$.

Moving radially inwards from the top of the lifter bar (denoted by A) the volume concentration is at a maximum of $\phi_{max} \approx 0.6$. The region within the radial span of the lifter bars ($r > R_A$)

are made complicated by the lifter bars and hence excluded from the current analysis. Future work will focus more quantitatively on this region. The region between A and B characterises the static or plug flow regime in which the material flows with essentially the same angular velocity as the drum. B denotes a point on the equilibrium surface (ES) and marks the end of the plug flow regime. The region between B and C corresponds to the quasi-static flow regime; cf. figure (2.1) which describes the quasi-static regime by the characteristic exponential velocity profile [Midi (2004)]. We note that the quasi-static regime is characterised by $\phi \approx \phi_{max}$ with an ever-so-slight drop in ϕ at the ES (denoted by point B). Stress chains dominate this regime and interactions are purely frictional. The region between C and D (D is shown in the zoomed-in image of figure (4.1)) marks the dense or liquid-like region where ϕ is observed to drop exponentially to $\phi_{min} \approx 0.4$. The choice of $\phi_{min} = 0.4$ is consistent with the leading theory on dense granular flow [Jop et al. (2006), Forterre and Pouliquen (2008)]. With stress chains typically expected to break at around $\phi \approx 0.5$ [Shuyan et al. (2009)], collisional-type interactions are also expected in this region in accordance with the equivalent (and original) work by Bagnold (1954). At $\phi_{\mathrm{FS}} < \phi < 0.4$ −corresponding to the region between D and E− we expect all stress chains to be broken. Inertial-type flow should dominate this region and the only permitted stresses should be kinetic- or collisional-type stresses. Above the FS, ϕ drops steeply to approximately zero which is consistent with the gas-like regime. At the bottom of the flow where the ES and FS appear to converge, we note that the gas-like regime cataracts into the relatively dense region, often referred to as the *toe* in the mineral processing literature. The corresponding velocity field map, figure (4.3), reveals this region to be turbulent with the velocity vectors exhibiting very chaotic behaviour. This is the source of the turbulence. It is difficult to predict how deep into the bed this turbulence propagates; however, given that the cataracting stream appears to collide with the the entire free surface, it is plausible to assume that the very top end of the inertial regime (i.e. the region about the free surface) also exhibits turbulent stresses, even though the effect is likely to drop off further away from the toe region. Notwithstanding, we argue that it exists and should be accounted for in the rheological analysis. Future work should definitely attempt to quantify the propagation length of this turbulence.

4.2 Model formulation

By assuming that the quasi-static (τ_s), kinetic-collision (τ_c) and turbulent (τ_t) shear stresses obey the additive rule [Savage (1998), Shuyan et al. (2009)], the total shear stress (τ) can be expressed as

$$\boldsymbol{\tau} = \boldsymbol{\tau}_s + \boldsymbol{\tau}_c + \boldsymbol{\tau}_t. \tag{4.1}$$

Further, τ_s can be written as the sum of the internal shear stress τ_i and side wall frictional shear stress τ_w, equation (4.1).

$$\boldsymbol{\tau} = \boldsymbol{\tau}_i + \boldsymbol{\tau}_w + \boldsymbol{\tau}_c + \boldsymbol{\tau}_t. \tag{4.2}$$

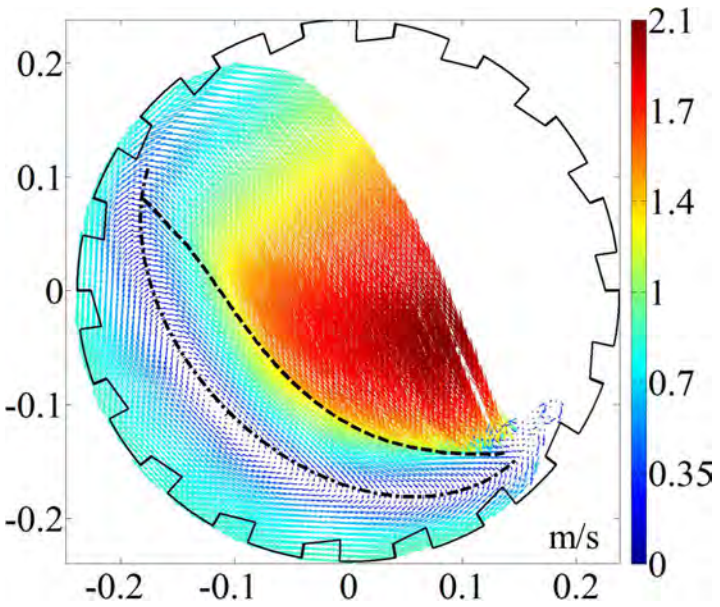

Figure 4.3: Velocity field of the granular bed for the mill rotating at 60% of critical speed. At the bottom of the flow where the ES and FS appear to converge, we note that the gas-like regime cataracts into the relatively dense region. The velocity field vectors appear chaotic in this region, suggesting the possibility of turbulence. In fact, the cataracting interaction with the bed is not limited to the bottom of the flow but actually occurs along most of the free surface.

Internal frictional shear stress τ_i and wall frictional shear stress τ_w play a significant role when the inertial number I of a granular system is very low [Jop et al. (2005), Taberlet et al. (2003), Taberlet et al. (2006)]. At higher inertial numbers, kinetic-collisional τ_c [Bagnold (1954)] and turbulent shear stress τ_t [Takahashi (2009)] begin to play a significant role. Similarly, the total pressure or total normal stress (p) of the system can be expressed as the sum of its constituents.

$$p = p_s + p_c + p_t \tag{4.3}$$

where p_s, p_c and p_t represent quasi-static, kinetic-collisional and turbulent normal stresses respectively. Similar to quasi-static shear stress τ_s, the quasi-static normal stress (p_s) can be written as the sum of normal stresses p_i and p_w in analogy to the internal shear stress τ_i and wall friction shear stress τ_w respectively.

4.2.1 Pressure and Volume concentration

From the definition of the inertial number [Midi (2004)], the total pressure at some location having inertial number I is given by equation (4.4).

$$p = \left(\frac{\dot{\gamma} d}{I}\right)^2 \rho_m \tag{4.4}$$

where ρ_m, d, $\dot{\gamma}$ and I represent material density, size of granular material, shear rate and inertial number respectively. The relationship between the material density ρ_m, volume concentration ϕ and bulk density ρ is given by

$$\rho = \phi \rho_m. \tag{4.5}$$

When the inertial number I increases sufficiently, the granular system can evolve from the dense to the inertial regime, corresponding to a decrease in the total pressure (p) according to equation (4.4). But the increase in inertial number also leads to an increases in inter-particle collisions which means that p_c increases. Mathematical consistency then demands that $p_s + p_t$ be negative to offset the increase in p_c such that the total pressure p decreases. But ($p_s < 0$) is not physical[1]. Therefore, when I increases sufficiently such that kinetic-collisional interactions become relevant, physical consistency demands that

$$\begin{aligned} p_s &\to 0, \text{ and} \\ p &= p_c + p_t. \end{aligned} \tag{4.6}$$

Under high loading, p_s is reported [Lee and Huang (2012), Johnson and Jackson (1987), Johnson et al. (1990), Josserand et al. (2006)] to obey the scaling law: $p_s = p_0 (\phi_0 - \phi_{\min})$ and vanishes in the inertial regime, i.e. when $\phi < \phi_{\min}$; cf. figure (4.2) where $\phi_{\min} \approx 0.4$. ϕ_0 (the volume concentration as $I \to 0$) and p_0 are said to be non-trivially dependent on particle properties, making them difficult to determine.

When I gets sufficiently low, equation (4.4) predicts that the total pressure (p) increases unboundedly which is inconsistent with measurement [Johnson et al. (1990), Josserand et al. (2006)]. Intuitively, we also expect some level of pressure saturation as predict by the *Janssen Effect* [Andreotti et al. (2013)]. The steric hinderance consistent with low inertial numbers also implies that the motion is quasi-static and hence dominated by quasi-static pressure, i.e. $p_s \gg p_t,\ p_k$. Accordingly, to ensure a physically consistent picture requires

$$p = p_s \quad (I \to 0). \tag{4.7}$$

While the conditions expressed by equations (4.6 and 4.7) ensure physical and mathematical consistency, they also signal a deficiency in the inertial number definition to adequately describe the total pressure. Some authors [Takahashi (2009), Lee and Huang (2012)] circumvent these limitations by carefully choosing an appropriate functional form for the volume concentration (ϕ) such that a pragmatic balance between mathematical and physical consistency is satisfied. Hatano (2007) suggests a power law for the dilatancy: $\phi(I) = \phi_{\max} - aI^{\delta}$ which Lee and Huang (2012) claim is more accurate than the linear law by Jop et al. (2005): $\phi(I) = \phi_{\max} + (\phi_{\min} - \phi_{\max})\, I$; see figure (4.4) for a comparative plot of the two models, along with the linear model of da Cruz et al. (2005): $\phi(I) = \phi_{\max} - aI$. We note that all three models remain relatively constant and only appear to decrease (beyond the uncertainties of measurement) for $I > 0.1$. In the models of Hatano (2007) and da Cruz et al. (2005)

[1] Calculations in chapter (5) clearly show that $p_t \ll p_s$ and hence p_t is omitted from the present argument.

$0.5 \leq \phi \leq 0.6$ for the inertial range $10^{-4} \leq I \leq 1$ while the model of Jop et al. (2005) yields $0.4 \leq \phi \leq 0.6$ for the same inertial range. However, 3D measurements by Orpe and Khakhar (2007) (see figure (31a) in their paper for three different particle diameters) in rotating drums suggest that the dense regime spans the inertial range $0 < I < 0.4$ with the upper limit corresponding to the free surface (FS) and estimated as $I_{upper} \approx 0.4$. Imposing $I_{upper} = 0.4$ on the models of Hatano (2007), da Cruz et al. (2005) and Jop et al. (2005) implies that the allowed range of volume fraction is $0.52 < \phi < 0.6$. But the measured volume fraction in the dense regime for tumbling mills is clearly shown in figure (4.2) to span $0.2 < \phi \leq 0.6$ for the 60% of critical speed data. Clearly the three models [Jop et al. (2005), da Cruz et al. (2005), Lee and Huang (2012)] do not span a wide enough range of the volume concentration for adequately addressing tumbling mill flows and are arguably better suited to the quasi-static regime.

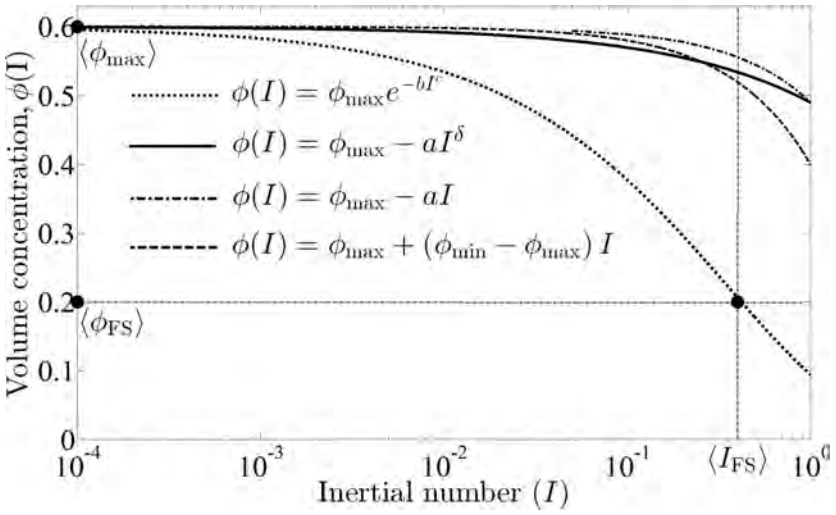

Figure 4.4: Variation of volume concentration (ϕ) with inertial number (I) according to the models of da Cruz et al. (2005) (dashed-dotted line), Jop et al. (2006) (dashed line), Hatano (2007) (solid line; parameters according to Lee and Huang (2012)), and the empirical model developed in this work (dotted line).

We thus propose an empirical dilatancy model consistent with the experimental findings from PEPT:

$$\phi(I) = \phi_{\max} \exp(-bI^c). \tag{4.8}$$

The coefficients ($b = 1.348$) and ($c = 0.6014$) are chosen such that at the free surface (FS):

1. The average inertial number $\langle I_{FS}\rangle = 0.4$ in consistency with the 3D measurements of Orpe and Khakhar (2007), and
2. the average volume concentration $\langle\phi_{FS}\rangle = 0.2$ in accordance with the average value determined over all PEPT data analysed in this thesis; see figure (4.5) for the free surface range employed in estimating $\langle\phi_{FS}\rangle$.

Figure (4.4) shows the proposed model along with the previously described literature models [Hatano (2007), da Cruz et al. (2005), Jop et al. (2005)].

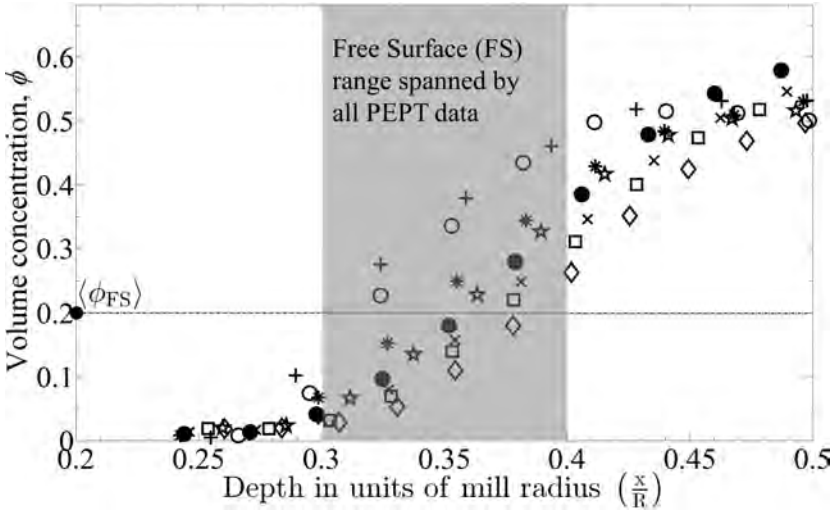

Figure 4.5: Illustration of the average volume concentration about the free surface, as obtained from PEPT data of tumbling mills operated across a wide range of drum speeds (in % of critical speed): $(40 : 5 : 75)\%$. The average data is determined along the radial line passing through the thickest region of the flow as shown in figure (4.1).

Substituting equation (4.8) into equation (4.4) then gives an appropriate model for total pressure:

$$p = \rho_m \left[\frac{b}{\ln\left(\frac{\phi_{\max}}{\phi}\right)}\right]^{2/c} (\dot{\gamma} d)^2 . \tag{4.9}$$

Intuitively, free surface flows should be subject to gravitational pressure. Consequently, most literature models write the total pressure as simply

$$p = \rho g h(\theta) \cos(\theta). \tag{4.10}$$

Notwithstanding, we favour equation (4.9) for the pressure based on the fact that the inputs to the calculation are accurate and consistent with literature. The following points summarise the motivation:

1. The inertial number is reasonably well predicted by the volume concentration model given by equation (4.8). In particular, the prediction is consistent with literature values at the free surface [Orpe and Khakhar (2007)].
2. The shear rate is accurately recovered from PEPT data.
3. The regions classified as pure inertial ($\phi < 0.4$), and indeed the regions where stress chains just break down ($\phi < 0.5$), cannot be simply hydrostatic-like as collisional stresses also exist in these ϕ-regimes.

It is also important to point out that an explicit model for total pressure is not needed to formulate the effective friction coefficient $\mu(I)$. The next chapter will, however, utilise

equation (4.9).

Figure (4.6) shows the local coordinate system ($x,\ z$) oriented at angle θ with $h = h(\theta)$ denoting the local depth of flowing layer.

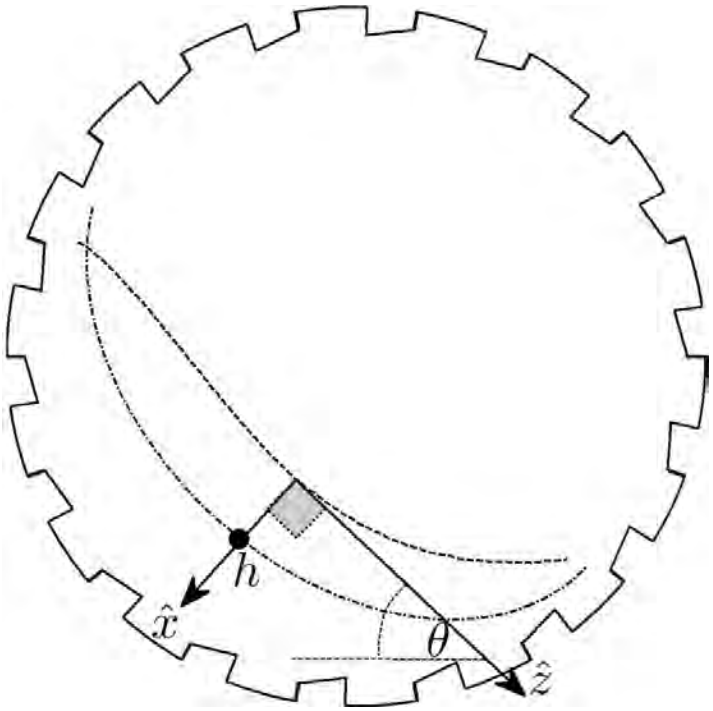

Figure 4.6: Illustration of the local coordinate system employed in the present work. The origin is located on the top of the free surface layer with $\hat{z}$ aligning tangentially to the free surface and oriented at angle θ to the horizontal; and $\hat{x}$ orthogonally to the surface. The position at $(h\hat{x}, 0)$ denotes the bottom of the flowing layer along the equilibrium surface such that $x(h, \theta)$ gives the magnitude of the local depth (h).

4.2.2 Stress constituents

The kinetic-collision shear stress τ_c is well described by Bagnold (1954) using collisional arguments that were later confirmed by Forterre and Pouliquen (2008) from pure dimensional analysis.

$$\tau_c = \alpha \rho_m \left(\lambda d\right)^2 \left(\frac{\partial \mathrm{v}_z}{\partial x}\right)^2 \tag{4.11}$$

where ρ_m, d and λ represent material density, diameter of the grain and linear grain density respectively. The shear rate $\left(\frac{\partial \mathrm{v}_z}{\partial x}\right)$ is based on the local velocity (v_z) where $\hat{z}$ is tangent to the free surface as shown in figure (4.6).

The proportionality constant (α) is set to 1 for convenience. The linear grain density λ of the granular system can be defined in terms of the radial distributed function (g_0) [Savage and Hutter (1998)] and volume concentration (ϕ):

$$g_0 = \frac{1 - \frac{7}{16}\phi}{\left(1 - \frac{\phi}{\phi_c}\right)^2}. \tag{4.12}$$

The linear grain density function λ is related to g_0 as

$$\begin{aligned} \lambda &= g_0 - 1 \\ &= \frac{1 - \frac{7}{16}\phi}{\left(1 - \frac{\phi}{\phi_c}\right)^2} - 1 \end{aligned} \tag{4.13}$$

where $\phi_c = 0.63$. According to the granular flow investigations by Bagnold (1954), Armanini et al. (2005) and Roufail et al. (2012), the normal pressure $p_c \simeq \left(\frac{1}{3}\right)\tau_c$. Using this experimentally confirmed approximation then yields

$$p_c = \frac{1}{3}\rho_m \left(\lambda d\right)^2 \left(\frac{\partial \mathrm{v}_z}{\partial x}\right)^2. \tag{4.14}$$

Finally, the turbulent shear stress (τ_t), can be analogously obtained from Prandtl's mixing theory −the so-called Prandtl closure: $\eta_t = \rho l^2 \left(\frac{\partial \mathrm{v}_z}{\partial x}\right)$; see Takahashi (2009) for more details− to yield

$$\tau_t = \rho l^2 \left(\frac{\partial \mathrm{v}_z}{\partial x}\right)^2 \tag{4.15}$$

where η_t is the turbulent viscosity, ρ is the bulk density of the granular particles, and l the mixing or coherence length that relates to the size of some clusters in the flow. According to Ashida et al. (1985) and Hotta (2012), the definition of mixing or coherence length l can be defined as:

$$l = k_t \rho d^2 \left(\frac{1 - \phi}{\phi}\right)^{\frac{2}{3}} \tag{4.16}$$

where k_t is the ratio between the shape parameters of the granular particles and the interstitial space [Suzuki et al. (2003), Hotta (2012)]. Midi (2004) note that their heap flow data (no rotating drum data was used so we choose their heap data which is qualitatively similar to the rotating drum system) yields an exponential increase in coherence length with bed depth where $l \sim 10d$. Informed by their findings, we pragmatically[2] choose $\langle l \rangle = 16d$ which yields $k_t \simeq 2.3$. Substituting $\rho = \rho_m \phi$ into equation (4.16) yields the following for the turbulent stress τ_t:

[2]the pragmatic choice yields an average effective friction coefficient that matches Orpe and Khakhar (2007) and current PEPT data at the FS.

$$\tau_t = k_t \rho_m d^2 \phi^{\frac{1}{3}} (1-\phi)^{\frac{2}{3}} \left(\frac{\partial \mathrm{v}_z}{\partial x} \right)^2 . \tag{4.17}$$

The expression for the normal component of the turbulent stress (p_t) is obtained from Hotta (2012) and given by equation (4.18):

$$p_t = k_t \rho_m d^2 \phi^{\frac{1}{3}} (1-\phi)^{\frac{2}{3}} \left(\frac{\partial \mathrm{v}_z}{\partial x} \right)^2 . \tag{4.18}$$

From equations (4.17 and 4.18), we observe that the expressions for τ_t and p_t are identical.

As mentioned earlier, the expression for the quasi-static shear stress (τ_s) can be written as

$$\tau_s = \tau_i + \tau_w \tag{4.19}$$

where τ_i is internal frictional shear stress and τ_w is wall frictional shear stress. We choose the internal shear stress description of Jop et al. (2006) because of internal frictional stress is strongly argued by many leading authors [Jop et al. (2006), Orpe and Khakhar (2007), Lee and Huang (2012), Pignatel et al. (2012)] to dominate the dense flow regime. With this assertion, the internal friction coefficient μ_i proposed by Jop et al. (2006) is:

$$\mu_i (I) = \mu_1 + \frac{\mu_2 - \mu_1}{I_0/I + 1} \tag{4.20}$$

where $I_0 = 0.279$, μ_2, and μ_1 are constants and they depend on the granular material. The internal frictional shear stress τ_i is then given by

$$\tau_i = \left[\mu_1 + \frac{\mu_2 - \mu_1}{I_0/I + 1} \right] p_s \tag{4.21}$$

where p_s is the pressure associated with τ_s. Similarly, the expression for the wall frictional shear stress is given by

$$\tau_w = \mu_w \left(\frac{x}{L} \right) p_s \tag{4.22}$$

where $\mu_w \left(\frac{x}{L} \right)$ is the wall frictional coefficient proposed by [Taberlet et al. (2003)]. In this expression μ_w, x and L represent the frictional coefficient of side walls, depth and length of the rotating drum respectively. Accordingly,

$$\tau_s = \left[\mu_1 + \frac{\mu_2 - \mu_1}{I_0/I + 1} \right] p_s + \mu_w \frac{x}{L} p_s \tag{4.23}$$

where $p_s = p - p_c - p_t$. The total shear stress τ is then obtained by adding its constituents τ_s, τ_c and τ_t.

$$\begin{aligned}\tau &= \mu_i(I)\, p_s + \mu_w \left(\frac{x}{L}\right) p_s + \rho_m (\lambda d)^2 \dot{\gamma}^2 + k_t \rho d^2 \phi^{\frac{1}{3}} (1-\phi)^{\frac{2}{3}} \dot{\gamma}^2 \\ &= \left[\mu_i(I) + \mu_w \left(\frac{x}{L}\right)\right](p - p_c - p_t) + \rho_m (\lambda d)^2 \dot{\gamma}^2 + k_t \rho d^2 \phi^{\frac{1}{3}} (1-\phi)^{\frac{2}{3}} \dot{\gamma}^2\end{aligned} \tag{4.24}$$

Taking the ratio between the total shear stress τ and total pressure p then yields equation (4.25):

$$\begin{aligned}\frac{\tau}{p} = &\left[\mu_i(I) + \mu_w \left(\frac{x}{L}\right)\right]\left[1 - \frac{3}{p}\rho_m (\lambda d)^2 \dot{\gamma}^2 - \frac{1}{p} k_t \rho_m d^2 \phi^{\frac{1}{3}} (1-\phi)^{\frac{2}{3}} \dot{\gamma}^2\right] + \frac{1}{p}\rho_m (\lambda d)^2 \dot{\gamma}^2 \\ &+ \frac{1}{p} k_t \rho_m d^2 \phi^{\frac{1}{3}} (1-\phi)^{\frac{2}{3}} \dot{\gamma}^2\end{aligned} \tag{4.25}$$

The square of the inertial number I can be written as:

$$I^2 = \frac{\dot{\gamma}^2 d^2}{p/\rho_m}. \tag{4.26}$$

The ratio obtained from equations (4.26 and 4.25) is called the effective friction coefficient $\mu(I)$ for the rotating drum flow.

$$\frac{\tau}{p} = \left[\mu_i(I) + \mu_w \left(\frac{x}{L}\right)\right]\left[1 - 3\lambda^2 I^2 - k_t \phi \left(\frac{1-\phi}{\phi}\right)^{\frac{2}{3}} I^2\right] + \lambda^2 I^2 + k_t \phi \left(\frac{1-\phi}{\phi}\right)^{\frac{2}{3}} I^2 \tag{4.27}$$

thus implies

$$\mu(I) = \left[\mu_i(I) + \mu_w \left(\frac{x}{L}\right)\right]\left[1 - 3\lambda^2 I^2 - k_t \phi \left(\frac{1-\phi}{\phi}\right)^{\frac{2}{3}} I^2\right] + \lambda^2 I^2 + k_t \phi \left(\frac{1-\phi}{\phi}\right)^{\frac{2}{3}} I^2. \tag{4.28}$$

Rearranging gives

$$\begin{aligned}\mu(I) = &\mu_i(I)\left[1 - 3\lambda^2 I^2 - k_t \phi \left(\frac{1-\phi}{\phi}\right)^{\frac{2}{3}} I^2\right] + \mu_w \frac{x}{L}\left[1 - 3\lambda^2 I^2 - k_t \phi \left(\frac{1-\phi}{\phi}\right)^{\frac{2}{3}} I^2\right] \\ &+ \lambda^2 I^2 + k_t \phi \left(\frac{1-\phi}{\phi}\right)^{\frac{2}{3}} I^2.\end{aligned} \tag{4.29}$$

The effective friction coefficient $\mu(I)$ can be written in a compact form as:

$$\mu\left(I\right)=\widehat{\mu}_i\left(I\right)+\widehat{\mu}_w\left(I\right)\frac{x}{L}+\lambda^2 I^2\left[1+\frac{1}{\lambda^2}k_t\phi^{\frac{1}{3}}\left(1-\phi\right)^{\frac{2}{3}}\right] \tag{4.30}$$

where $\widehat{\mu}_i\left(I\right)$ is the effective internal frictional coefficient and is expressed by equation (4.31). Similarly, $\widehat{\mu}_w\left(I\right)$ expressed by equation (4.32) can be called effective wall frictional coefficient.

$$\widehat{\mu}_i\left(I\right)=\mu_i\left(I\right)\left[1-3\lambda^2 I^2-k_t\phi^{\frac{1}{3}}\left(1-\phi\right)^{\frac{2}{3}}I^2\right]. \tag{4.31}$$

$$\widehat{\mu}_w\left(I\right)=\mu_w\left[1-3\lambda^2 I^2-k_t\phi^{\frac{1}{3}}\left(1-\phi\right)^{\frac{2}{3}}I^2\right]. \tag{4.32}$$

If we neglect the influences of turbulent shear stress then the effective friction coefficient becomes

$$\mu\left(I\right)=\mu_i\left(I\right)\left[1-3\lambda^2 I^2\right]+\mu_w\frac{x}{L}\left[1-3\lambda^2 I^2\right]+\lambda^2 I^2 \tag{4.33}$$

To illustrate the form of equation (4.29) we use the average values for the tumbling mill system employed in this work, table (4.1).

Parameter	**Values**	**Description**
$\langle\theta_1\rangle$	21°	stopping angle of steady flow
$\langle\theta_2\rangle$	50°	starting angle of steady flow
$\langle x\rangle$	2.5×10^{-2} m	average bed depth
l	$15d$	related to mixing length
d	5×10^{-3} m	particle diameter
L	0.480 m	Effective length of drum
$\phi(I)=\phi_{\max}e^{-1.848I^{0.6014}}$	for $I\in[0;\ 1]$	Empirical model
μ_w	0.7	sidewall friction coefficient

Table 4.1: Average parameters used in equation (4.32) to plot figure (4.7).

From figure (4.7) we note the following important observations:

1. The hysteresis effect is successfully captured at the transition from the quasi-static to

dense flow regime. The corresponding inertial number at this phase transition (see inset in figure (4.7)) is $\langle I_{\mathrm{ES}} \rangle = 0.007$.

2. The second phase transition from the dense to gas-like regime is successfully and smoothly captured. The corresponding inertial number $\langle I_{\mathrm{FS}} \rangle = 0.4$ is consistent with the measurements of Orpe and Khakhar (2007) and equation (4.8) that predicts the measured solids concentration of $\langle \phi_{FS} \rangle = 0.2$ at this same inertial number; see figure (4.4) for confirmation.
3. The quasi-static regime occurs at $I \leq 0.007$.
4. The dense flow regime occurs at $0.007 < I < 0.4$.
5. The pure inertial regime occurs at values of I that satisfy $(I_{FS} - I) \ll 1$, i.e. very close to the free surface. It is also reasonable to expect that this inertial region could continue above the free surface layer where it is conceivable that kinetic-collisional stresses could persist.

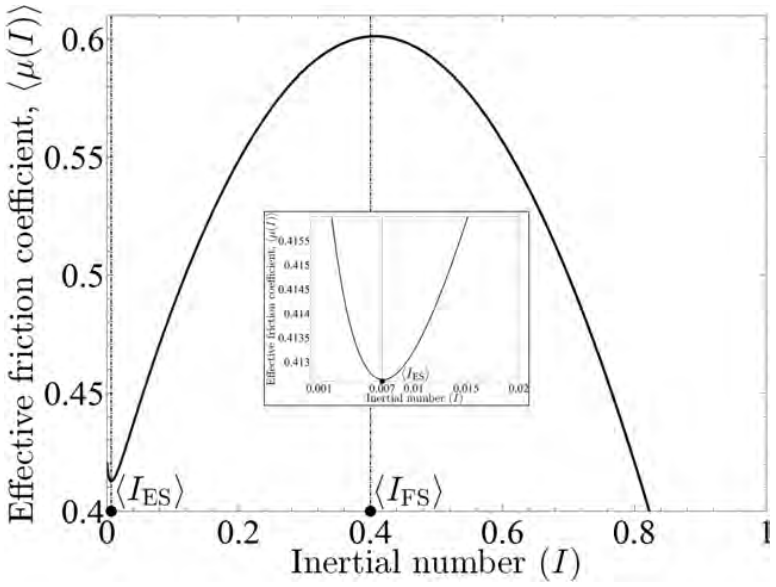

Figure 4.7: A plot of equation (4.29) using average values from table (4.1). The variation of $\langle \mu(I) \rangle$ shows that both phase transitions −from quasi-static to dense flow (see subplot where $\langle I \rangle_{\mathrm{ES}} = 0.007$); and from liquid-like to gas-like flow ($\langle I \rangle_{\mathrm{FS}} = 0.4$)− are smoothly captured at inertial numbers that correspond to volume concentration measurements derived from PEPT data.

4.3 Summary

In this chapter we developed an effective friction coefficient, equation (4.29), based on frictional (both internal and wall), kinetic-collisional and turbulent stresses. An empirical model for the volume concentration variation with inertial number, equation (4.8), is supported by PEPT measurements. The average rheology predicted by equation (4.29) appears consistent with literature [Orpe and Khakhar (2007)] and in its quantitative prediction of the two expected phase transitions.

Chapter 5

Power Dissipation

5.1 Introduction

Comminution is an industrial process that reduces the mean size of the particles within a tumbling mill as well as alters their size distribution. The mean size and width of the particle distribution is the one that highly influences the outcome of the grinding process [Fahlström (1962)]. Furthermore, the mineralogical properties of the resident particles, which can vary during mill operation, influence the operating conditions of the grinding mill. This implies that the effective operational setting of the tumbling mill will vary with time.

Types of tumbling mills that are currently employed for grinding are ball/rod and autogenous mills. The particular type of tumbling mill used depends on the type of ore to be comminuted. In rod and ball type tumbling mills, steel balls are added to the charge[1] to assist with the grinding process, whereas in the autogenous tumbling mills, ore alone is the charge medium.

In general, constructing realistically-proportioned mills for research purposes is not possible because construction and maintenance are uneconomical and manpower intensive. Instead, lab-scale tumbling mill experiments were performed [Powell et al. (2003)] for validating computer-based simulations using the discrete element method [McBride et al. (2004)]. We adapted a similar type of lab scale tumbling mill in order to collect validation data and propose a new visco-plastic model of granular flow which estimates energy dissipation within the rotating drum system.

Milling involves very high power consumption compared to other methods of comminution, and therefore it is beneficial to study its power dissipation mechanisms to remain cost effective and efficient. Nearly 3% of the electricity produced worldwide is used in comminution processes [Morrison and Cleary (2008)]. We need to have a good understanding of mill operations and know what operating conditions to change in order to optimise the grinding process. Quantitative understanding of power consumption requires high quality experimental data and the development of mechanistically sound models of granular rheology.

[1] The granular material within a comminution circuit are often termed the charge in analogy to charge in an electric circuit.

Construction of a model for granular flow inside a rotating mill is not a simple task. As described in the previous chapter, a new visco-plastic rheology has been proposed to investigate granular flow. The power dissipation calculation strongly depends on the correct rheological characterisation, which, in the context of this study implies an accurate accounting of the stresses that dominate in tumbling mill environments. The model for power dissipation coupled with the experimental data obtained from PEPT allow us to calculate the power dissipation in tumbling mills.

5.2 Energy balance for athermal granular flows in rotating drums

In this section we develop the differential energy balance for athermal systems, equation (5.11), based upon the formalism described in Bird et al. (2002). The balance equations are then split into shear and normal parts, and expanded using the stresses and underlying rheology developed in chapter (4). Figure (5.1) illustrates the continuum approximation (zoomed image illustrates the relevant unit volume) applied in this work along with the coordinate system.

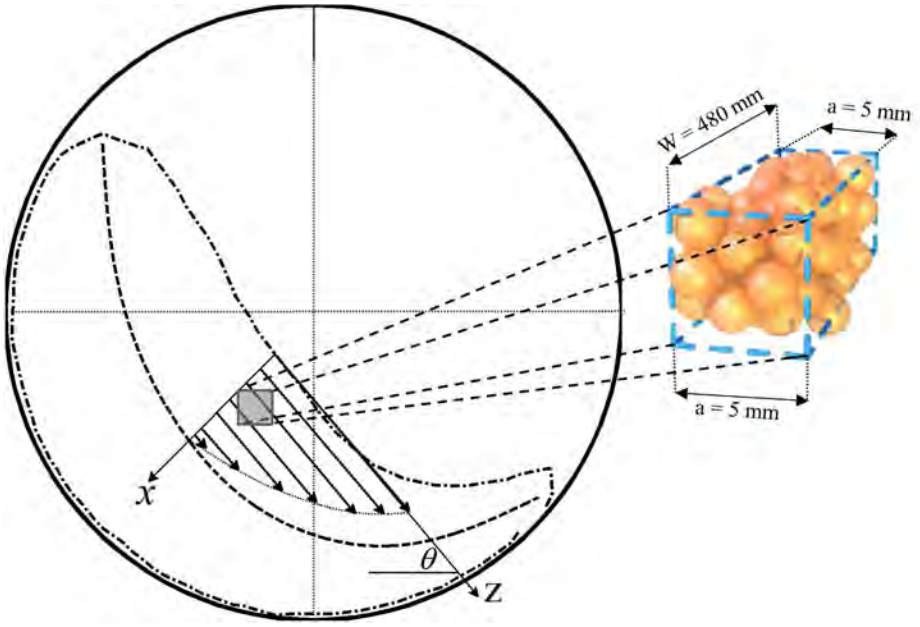

Figure 5.1: Illustrating the local coordinate system (previously defined in figure (4.6)) and the representative volume element (RVE) employed in the current continuum modelling approximation of granular flow. W = 500 − 20 denotes the effective length of the drum as described in section (3.2).

Consider the differential energy balance given by equation (5.1) for a unit volume of granular material in steady granular flow within a rotating mill.

$$\rho \frac{D}{Dt}\left(\frac{1}{2}\mathrm{v}^2\right) = -\mathbf{v}.\boldsymbol{\nabla} p - \mathbf{v}.\left(\boldsymbol{\nabla}.\boldsymbol{\tau}\right) + \left(\mathbf{v}.\boldsymbol{F}\right) \tag{5.1}$$

where $\mathbf{v}$ is the velocity of the granular material, p is the total pressure, $\boldsymbol{\tau}$ is the total shear

stress and $\boldsymbol{F}$ is the external force acting on the granular particles.

The equation is derived from the momentum balance equations with the important assumption that granular balance equations apply at the length (and time) scales of the unit volume [Bird et al. (2002)]. The granular medium is also assumed to be an athermal system. Accordingly, there is no degradation of mechanical energy into thermal energy in the sense that thermal fluctuations are microscopic and not discernable at the mesoscopic scale for which the current modelling is performed. Viscous heat dissipation is thus excluded apriori in this work. Consequently, the term $(\boldsymbol{\tau} : \boldsymbol{\nabla}\mathbf{v})$ that represents the rate of irreversible conversion from kinetic to internal energy is insignificant and excluded apriori from equation (5.1). Equation (5.2) thus follows naturally using well known identities as described in Bird et al. (2002). We will take full utility of equation (5.2) in realising the various shear terms.

$$(\boldsymbol{\nabla}.[\boldsymbol{\tau}.\mathbf{v}]) = (\mathbf{v}.[\boldsymbol{\nabla}.\boldsymbol{\tau}]) \tag{5.2}$$

The left hand side of equation (5.1) represents the rate of increase of kinetic energy, and vanishes when the granular flow reaches steady state. The three terms on the right hand side of equation (5.1) represent the rate of work done by pressure (p), viscous shear stress ($\boldsymbol{\tau}$) and gravitational force $\rho\mathbf{g}$ respectively.

5.2.1 Model assumptions

Considering the azimuthal (xz) perspective of the volume element, figure (5.2), the following assumptions are made in this work:

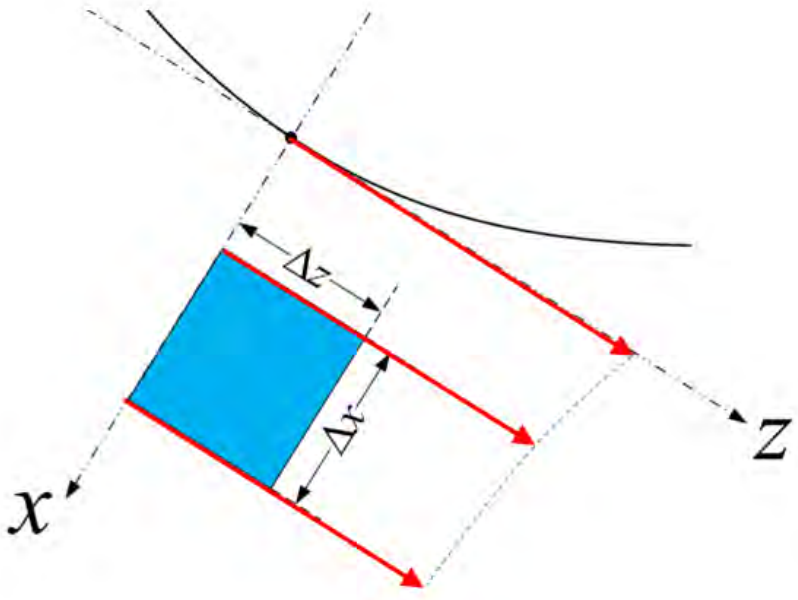

Figure 5.2: Diagramatic representation of the Lagrangian coordinate system that moves along the free surface of the charge.

1. Steady state granular flow exists over short distances of the order of the natural length scale, i.e particle diameter. Therefore, motive and dissipative stresses balance across the volume element, leading to:

$$\rho \frac{D}{Dt}\left(\frac{1}{2}\mathrm{v}^2\right) = 0. \tag{5.3}$$

2. Axial flow is negligible due to the batch nature of the PEPT experiments ($\mathrm{v}_y = 0$) implying pure azimuthal flow.

$$\mathrm{v}_z = \mathrm{v}_z\left(x\right) \tag{5.4}$$

   where $\mathrm{v}_z\left(x\right)$ is independent of $y-$ and $x-$ coordinates.

3. The findings from figure (3.10) clearly confirms that $\mathrm{v}_x \simeq 0$.

4. From the above assumptions, it can be easily proven that the only non-zero components of $\boldsymbol{\tau}$ are τ_{xz} and τ_{zx}. Assuming $\boldsymbol{\tau}$ is a symmetric tensor then implies:

$$\tau_{xz} = \tau_{zx} \tag{5.5}$$

   The granular system thus has effectively only one non-zero stress component that acts along the tangential direction. We note that this shear stress does not depend on the z coordinate, because the tangential velocity and hence the shear rate depend only on the x coordinate.

5. The external force $\boldsymbol{F}$ is defined by $\boldsymbol{F} = m\boldsymbol{g}$.

5.2.2 Differential power density

Basic tensorial manipulation of $(\mathbf{v}.\left[\boldsymbol{\nabla}.\boldsymbol{\tau}\right])$ yields:

$$\begin{aligned}\mathbf{v}.\left[\boldsymbol{\nabla}.\boldsymbol{\tau}\right] &= \mathbf{v}_x\left[\boldsymbol{\nabla}.\boldsymbol{\tau}\right]_x + \mathbf{v}_z.\left[\boldsymbol{\nabla}.\boldsymbol{\tau}\right]_z \\ &= \mathrm{v}_x\left(\frac{\partial \tau_{zx}}{\partial z}\right) + \mathrm{v}_z\left(\frac{\partial \tau_{xz}}{\partial x}\right),\end{aligned} \tag{5.6}$$

which simplifies further to equation (5.7) given the z coordinate independence of τ_{xz}.

$$\mathbf{v}.\left[\boldsymbol{\nabla}.\boldsymbol{\tau}\right] = \mathrm{v}_z\left(\frac{\partial \tau_{xz}}{\partial x}\right). \tag{5.7}$$

The right hand side of equation (5.7) involves a gradient of the shear rate (since shear stress is constitutively proportional to shear rate), which tends to be unreliable with PEPT data. Fortunately, equation (5.2) permits the use of the equivalent expression $(\boldsymbol{\nabla}.[\boldsymbol{\tau}.\mathbf{v}])$ for the power dissipation calculations, which evaluates as follows:

$$\boldsymbol{\nabla}.\left[\mathbf{v}.\boldsymbol{\tau}\right] = \left(\frac{\partial \mathrm{v}_z}{\partial x}\right)\tau_{xz} + \mathrm{v}_z\left(\frac{\partial \tau_{xz}}{\partial x}\right). \tag{5.8}$$

We can then write the shear term of differential power density as:

$$\left(\frac{\partial^3 B_{\mathrm{shear}}}{\partial x \partial y \partial z}\right) = \left(\frac{\partial \mathrm{v}_z}{\partial x}\right)\tau_{xz} + \mathrm{v}_z\left(\frac{\partial \tau_{xz}}{\partial x}\right). \tag{5.9}$$

Similarly, the compressive term of differential power density is given by:

$$\left(\frac{\partial^3 B_{\mathrm{comp}}}{\partial x \partial y \partial z}\right) = \mathrm{v}_x\left(\frac{\partial p}{\partial x}\right) \tag{5.10}$$

5.2.3 Power density balance

From equations (5.1), (5.9) and (5.10), we obtain the differential power density:

$$\mathrm{v}_z \rho \mathrm{g} \sin\theta = \left[\left(\frac{\partial \mathrm{v}_z}{\partial x}\right)\tau + \mathrm{v}_z\left(\frac{\partial \tau}{\partial x}\right)\right] + \mathrm{v}_x\left(\frac{\partial p}{\partial x}\right) \tag{5.11}$$

where the total shear stress and pressure have been defined in chapter (4). The objective from hereon is to develop equation (5.11) to the point that the measurements from PEPT (velocity, shear rate, volume concentration, and geometric features of the granular flow) allow for the full evaluation of the power density per unit volume.

To complete the calculation of the power density requires the following quantities:

(i) The tangential velocity: $v_z(x)$, which can then be used to

(ii) compute the shear rate: $\left(\frac{\partial \mathrm{v}_z}{\partial x}\right) = \dot{\gamma}$.

(iii) The gradient of the total pressure: $\left(\frac{\partial \mathrm{p}}{\partial x}\right)$, and

(iv) the gradient of the total shear stress: $\left(\frac{\partial \tau}{\partial x}\right)$.

(i) is obtained directly from PEPT data. Taking the (numerical) derivative of (i) with respect to x then yields (ii). To determine (iii) we consider the gradient of the total pressure, as given by equation (4.9), with respect to x:

$$\frac{\partial p}{\partial x} = 2\rho_m d^2 \dot{\gamma}\left[\frac{b}{\ln\frac{\phi_0}{\phi_i}}\right]^{2/c}\left(\frac{\partial \dot{\gamma}}{\partial x}\right) + 2\rho_m d^2 \frac{b^{2/c}}{c}\dot{\gamma}^2 \ln\left[\ln\frac{\phi_0}{\phi_i}\right]^{-\frac{2+c}{c}}\left(\frac{\phi_0}{\phi_i^2}\right)\left(\frac{\partial \phi_i}{\partial x}\right). \tag{5.12}$$

To facilitate the ensuing discussion, we compact our notation as follows:

$$\mathbb{G} = 2\rho_m d^2 \dot{\gamma} \left[\frac{b}{\ln \frac{\phi_0}{\phi_i}} \right]^{2/c} \left(\frac{\partial \dot{\gamma}}{\partial x} \right) + 2\rho_m d^2 \frac{b^{2/c}}{c} \dot{\gamma}^2 \ln \left[\ln \frac{\phi_0}{\phi_i} \right]^{-\frac{2+c}{c}} \left(\frac{\phi_0}{\phi_i^2} \right) \left(\frac{\partial \phi_i}{\partial x} \right), \tag{5.13}$$

$$\mathbb{H} = 6d^2 \rho_m \left[\lambda \dot{\gamma}^2 \left(\frac{\partial \lambda}{\partial x} \right) + \lambda^2 \dot{\gamma} \left(\frac{\partial \dot{\gamma}}{\partial x} \right) \right], \tag{5.14}$$

$$\mathbb{J} = 2k_t \rho_m d^2 \phi_i^{\frac{1}{3}} \dot{\gamma} \left(1 - \phi_i\right)^{\frac{2}{3}} \left(\frac{\partial \dot{\gamma}}{\partial x} \right), \tag{5.15}$$

and

$$\mathbb{K} = k_t \rho_m d^2 \dot{\gamma}^2 \left[-\frac{2}{3} \left(\frac{\phi_i}{1 - \phi_i} \right)^{\frac{1}{3}} + \frac{1}{3} \left(\frac{1 - \phi_i}{\phi_i} \right)^{\frac{2}{3}} \right] \left(\frac{\partial \phi_i}{\partial x} \right) \tag{5.16}$$

such that:

$$\begin{aligned} \left(\frac{\partial p_s}{\partial x} \right) &= \left[\frac{\partial}{\partial x} \left(p - p_c - p_t \right) \right] \\ &= \mathbb{G} - \mathbb{H} - \mathbb{J} - \mathbb{K}. \end{aligned} \tag{5.17}$$

We note that:

1. $\mathbb{G} = \frac{\partial p}{\partial x}$,
2. $\mathbb{H} = \frac{\partial p_c}{\partial x}$,
3. $\mathbb{J} + \mathbb{K} = \frac{\partial p_t}{\partial x}$,
4. $\mathbb{G} - \mathbb{H} - \mathbb{J} - \mathbb{K} = \frac{\partial p_s}{\partial x}$

The terms within $\mathbb{G}$, $\mathbb{H}$, $\mathbb{J}$, and $\mathbb{K}$ also require further expansion. In this regard

$$\left(\frac{\partial \phi_i}{\partial x} \right) = -bc\phi_i I^{c-1} \left(\frac{\partial I}{\partial x} \right), \tag{5.18}$$

where we have used the empirical dilatancy law, equation (4.8), for the volume concentration. Equation (5.18) can also be used for direct computation of $\frac{\partial I}{\partial x}$. In this case, $\phi(x)$ is measured using PEPT data and $\frac{\partial \phi}{\partial x}$ is determined numerically. Similarly, $\frac{\partial \lambda}{\partial x}$ gives:

$$\left(\frac{\partial \lambda}{\partial x}\right) = \frac{1}{\mathbb{C}}\left(\mathbb{A} - \mathbb{B}\right)\left(\frac{\partial \phi_i}{\partial x}\right) \tag{5.19}$$

where

$$\mathbb{A} = -\frac{7}{16}\left(1 - \frac{\phi_i}{\phi_c}\right)^2, \tag{5.20}$$

$$\mathbb{B} = \frac{2}{\phi_c}\left(1 - \frac{7\phi_i}{16}\right)\left(1 - \frac{\phi_i}{\phi_c}\right) \tag{5.21}$$

and

$$\mathbb{C} = \left(1 - \frac{\phi_i}{\phi_c}\right)^4. \tag{5.22}$$

Finally, (iv) yields:

$$\begin{aligned}\left(\frac{\partial \tau}{\partial x}\right) &= \frac{\partial}{\partial x}\left(\tau_i + \tau_w + \tau_c + \tau_t\right) \\ &= \mathbb{Q} + \mathbb{R} + \frac{1}{3}\mathbb{H} + \mathbb{J} + \mathbb{K}\end{aligned} \tag{5.23}$$

where

$$\mathbb{Q} = p_s\left(\frac{\partial \mu_i}{\partial x}\right) + \mu_i\left(\frac{\partial p_s}{\partial x}\right) \tag{5.24}$$

and

$$\mathbb{R} = \mu_w\frac{p_s}{L} + \mu_w\left(\frac{x}{L}\right)\left(\frac{\partial p_s}{\partial x}\right). \tag{5.25}$$

5.3 Illustration of model predictions & related PEPT outputs

In this section we show the results of the stresses and associated PEPT input data for the mill operated with 5 mm glass beads at 60 % of critical speed. Given that 60 % of critical speed

is approximately the average speed (average speed is 58 %) employed in this work, it should quantify the average predictions from the previously developed models. In the interest of a more quantitative exposition, we limit our analysis to the central radial line (locally oriented at angle θ to the free surface) as shown previously in figure (4.1).

The PEPT inputs to the stress calculations are:

1. Volume concentration profile $\phi(x)$ − figure (5.3a), and the associated
2. Inertial number profile $I(x)$ − figure (5.3c).
3. Velocity profile $v_z(x)$ − figure (5.3b), and the associated
4. Shear rate profile $\dot{\gamma}(x)$ − figure (5.3d).

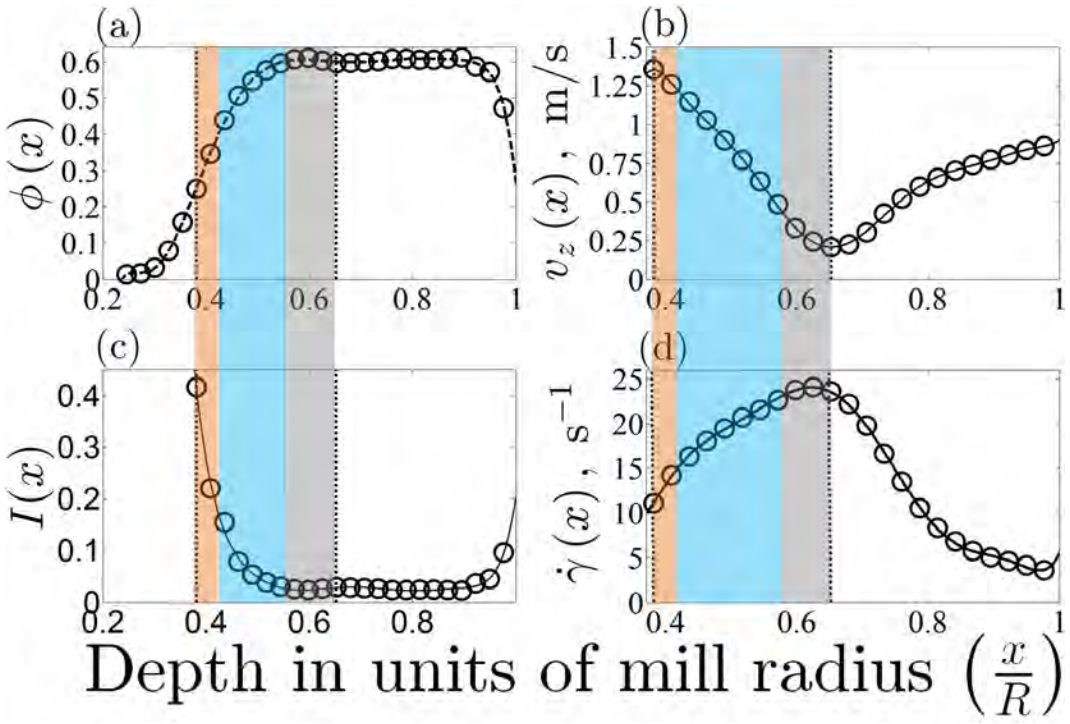

Figure 5.3: PEPT derived profiles along the radial line (oriented at angle θ to the horizontal) passing through the thickest region of the flow: (a) volume concentration $\phi(x, \theta)$, (b) tangential velocity $v_z(x, \theta)$, inertial number $I(x, \theta)$, and shear rate $\dot{\gamma}(x, \theta)$. The shaded regions delineate the quasi-static (gray), dense (blue), and inertial (orange) flow regimes.

The corresponding stress components are shown in figure (5.4).

Along the thickest region of the flow, the following conclusions may be drawn:

1. the average normal stress dominates over the average shear stress by a factor of approximately three, i.e. $p \sim 3\tau$.
2. The maximum stress occurs about the interface between the quasi-static and liquid-like regime.

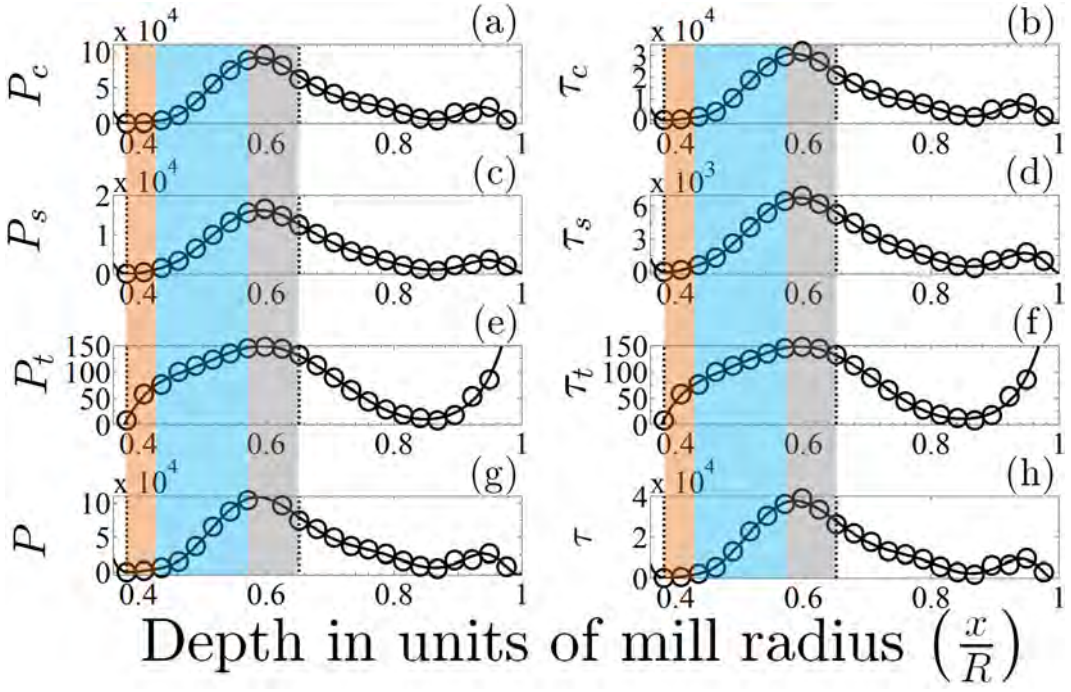

Figure 5.4: PEPT-derived normal and shear stress profiles along the radial line (oriented at angle θ to the horizontal) passing through the thickest region of the flow are shown in the first and second columns respectively. The top three rows indicate the collisional (P_c, τ_c), frictional (P_s, τ_s) and turbulent (P_t, τ_t) components of the shear and normal stresses respectively, while the bottom row shows the total normal ($P = P_c + P_s + P_t$) and shear ($\tau = \tau_c + \tau_s + \tau_t$) stress. The shaded regions delineate the quasi-static (gray), dense (blue), and inertial (orange) flow regimes.

3. The inertial regime is comprised almost entirely of turbulent stresses albeit relatively small contributions.

4. The shear rate at the free surface is clearly non-zero; cf. Midi (2004) who make the observation.

5. The stresses at the free surface (FS) are very small, but arguably not zero.

6. To a first order approximation, the stress profile in each flow regime varies linearly with depth.

7. The inertial number drops exponentially from the free surface to the bottom of the dense regime. Going deeper into the bed (across the quasi-static and so-called plug flow regime), the inertial number appears to remain constant. Accordingly, the collisional stresses in these regions are small and vary very little. Of equal importance is the fact that $I(x)$ varies relatively smoothly with x. Derivatives are thus reliable and easily determined from the PEPT data.

8. The region about the lifter bars exhibit negligible stresses except for a bit of turbulence. It is thus reasonable to assume plug flow in this region; however, the rest of the rising layer seems more akin to creeping flow.

The effective friction coefficient $\left[\mu(x) = \frac{\tau(x)}{p(x)}\right]$ tracks very closely the shape of the inertial

number $[I(x)]$ over the same depth profile; see figure (5.5). The dense (liquid-like) regime is characterised by an essentially constant value of $\mu(x) \approx 0.35$. The same value persists into the quasi-static regime. The inertial regime is characterised by an exponential growth in $\mu(x)$ in the range $0.35 < \mu(x) < 0.65$. This is not surprising given the strong dependence of the $\mu(x)$ with $I(x)$; cf. Orpe and Khakhar (2007) who get $\mu_{\text{ES}} \approx 0.3$ at the bottom of dense flowing layer and $\mu_{\text{FS}} \approx 0.6$ at the free surface.

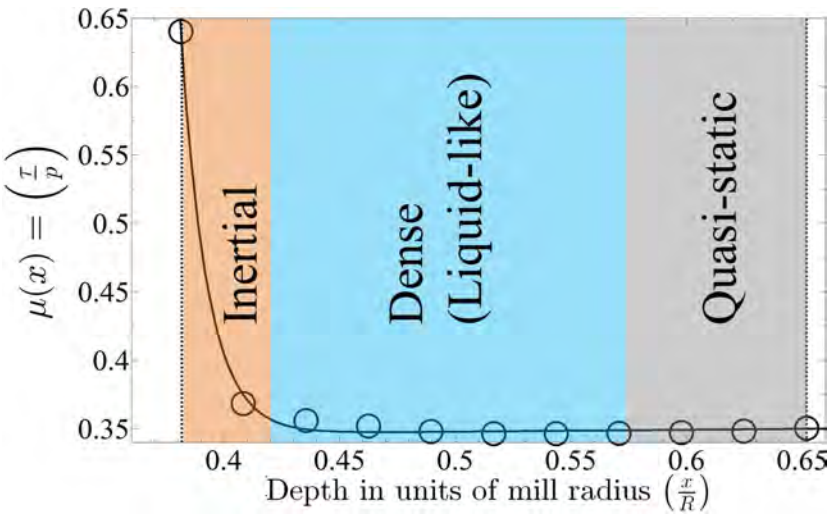

Figure 5.5: Variation of the effective friction coefficient $\mu(x)$ along the radial line (oriented at angle θ to the horizontal) passing through the thickest region of the flow.

The corresponding power density for the shear and normal components of the stress are given in figure (5.6) for the mill operated at 60% of critical speed. The following observations are made:

1. The highest power dissipation occurs in the quasi-static regime
2. The inertial regime depicts negligible power dissipation
3. The transition from the quasi-static region to the plug flow region is accompanied by a rapid drop in power dissipation. At approximately four particle layers below the equilibrium surface, the power dissipation stabilises and drops of gently with increasing depth towards the azimuthal boundaries.
4. Interestingly, despite the fact that $p \sim 3\tau$, the shear power dissipation dominates over the normal (compressive) power dissipation by a factor of seventeen, i.e.

$$\left(\frac{\partial^3 B_{\text{shear}}}{\partial x \partial y \partial z}\right) \sim 17 \left(\frac{\partial^3 B_{\text{comp}}}{\partial x \partial y \partial z}\right). \tag{5.26}$$

This is largely influenced by the fact that $\frac{v_x}{v_z} \ll 1$ as confirmed in figure (3.10). Unfortunately, the extent of the proposed theory does not account for (compressive) stresses above the von Mises yielding limit where we expect complex loading and stress behaviour to exist. To be clear, the current theories of granular flow [Midi (2004), Jop et al. (2006), Orpe and Khakhar (2007)], and indeed the work presented herein, is strictly valid far below the von Mises limit. The reader is thus cautioned to not infer too much by way

of damage or fracture from the proposed description. Rather, the current description should serve as a proxy for where damage (and in general comminution) is most likely to occur.

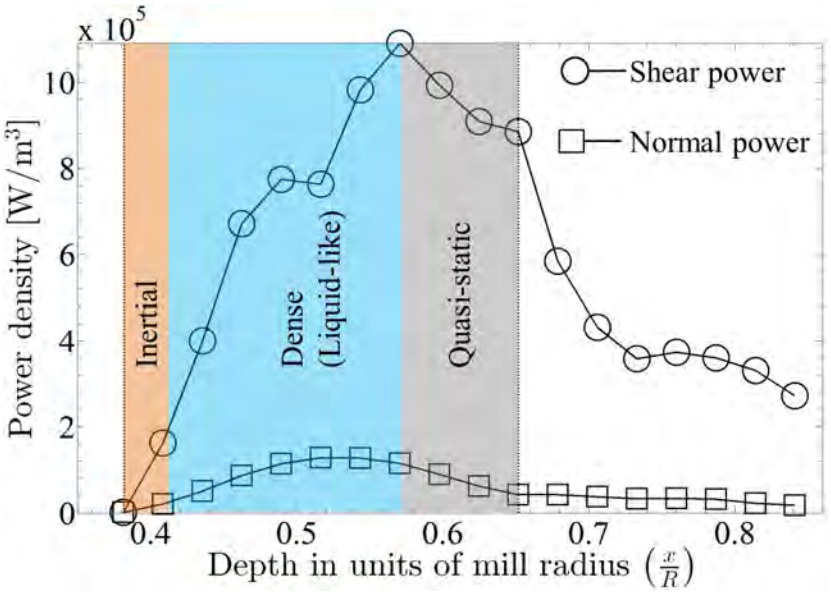

Figure 5.6: Variation of the shear (circles) and normal (squares) power density along the radial line (oriented at angle θ to the horizontal) passing through the thickest region of the flow.

Finally, the variation of the normalised mixing length $\left(\frac{l}{d}\right)$ with bed depth can be directly computed using the Prandtl closure to give: $\frac{l}{d} = \left(\frac{1}{d\dot{\gamma}}\right)\sqrt{\frac{\tau_t}{\phi\rho_{\mathrm{m}}}}$. Figure (5.7) shows the plot: The mixing length increases rapidly from the free surface to the bottom of the inertial regime, then drops exponentially through the dense and quasi-static regime before eventually asymptoting into the plug flow regime; cf. Midi (2004) who observe an exponential increase from the FS to the bottom of the quasi-static regime albeit for heap flow data. We note that our picture is more consistent with other authors [Takahashi (2009), Ashida et al. (1985), Hotta (2012)] and indeed the physical expectation that turbulence should drop off steeply with increasing bed depth (and correspondingly with increasing volume concentration). The influence of the total stress on the overall mixing length is also interesting, figure (5.8): The mixing length is observed to again increase rapidly from the free surface to the bottom of the inertial regime, and then drops linearly through the dense and quasi-static regime.

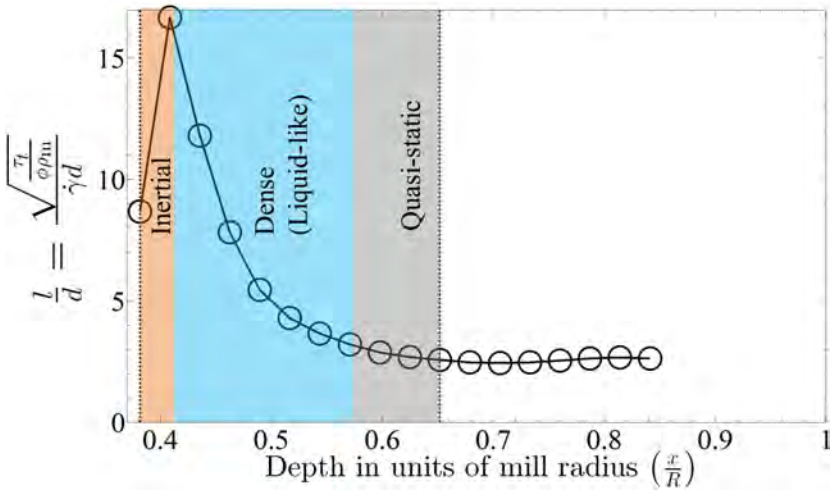

Figure 5.7: Variation of mixing length (l) along the radial line (oriented at angle θ to the horizontal) passing through the thickest region of the flow using only the turbulent shear stress according to equation (4.15).

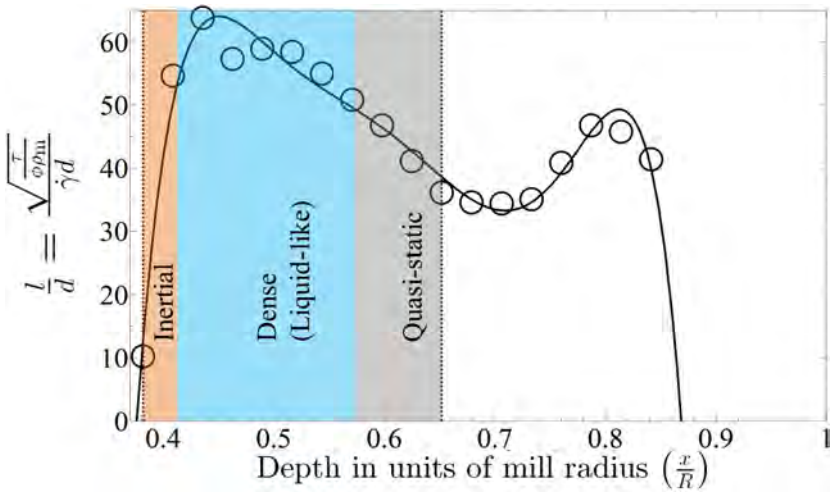

Figure 5.8: Variation of mixing length (l) along the radial line (oriented at angle θ to the horizontal) passing through the thickest region of the flow using the total shear stress.

Chapter 6

Discussion of 5 mm & 8 mm data

6.1 Introduction

The data is analysed in two forms for both the 5 mm and 8 mm PEPT data gathered over the speed range 40 : 5 : 75 % of critical speed: (i) Using the time-averaging scheme described in section (3.2.2), 2D azimuthal maps are obtained. (ii) The profiles along the radial line (oriented at angle θ to the horizontal) passing through the thickest region of the flow is also used to facilitate more quantitative discussions on the rheology, related flow regimes, dominant stresses and power density. It is argued by many authors [Midi (2004), Jop et al. (2006), Meier et al. (2007), Orpe and Khakhar (2007), Pignatel et al. (2012)] that most of the important physics governing granular flows can be discerned from quantitative investigation of the thickest part of the granular bed where a rich combination of flow regimes coexist. We thus perform a similar analysis in this chapter and append the 2D azimuthal maps to Appendix (4). It should be stressed that while these 2D maps do not form an integral part of the present discussion, they do complement the descriptions given herein.

The radial lines presented herein coincide (within the uncertainties) to the maximum depth profile measured orthogonal to the tangent line at the corresponding free surface point. The reader is referred to figure (4.1) for an illustration of the aforementioned radial line. Although not directly relevant to the current work, the point corresponding to the interface between the rising and flowing layer −point B in figure (4.1)− is often referred to as the center of circulation (CoC) in the minerals engineering literature and denotes the point about which all the material (or charge) appears to circulate. Where necessary, we will adopt the same jargon in the interest of efficient exposition.

Given that the models presented in chapters (4 and 5) do not include the gas-like regime, located above the free surface layer, we exclude apriori this region from the current analysis. Accordingly, both the 2D azimuthal maps presented in Appendix (4) and the radial profiles through the CoC span the plug flow, quasi-static, dense (liquid-like) and inertial regimes only.

6.2 Volume concentration

Figures (D.1 and D.2) show the azimuthal distribution of the volume concentration for the 5 mm and 8 mm PEPT data. While the actual data per RVE is useful for detailed calculations, a quantitative discussion is better achieved using the profiles along the radial line passing through the CoC. As shown in figures (6.1a and 6.1b), the volume concentrations (ϕ) monotonically increases with depth (x) up to a volume concentration of $\phi \approx 0.6$, remaining relatively constant with further increases in depth. The location of the FS and ES varies with mill speed. The range spanned by the free surface (FS) and equilibrium surface (ES) are illustrated in figures (6.1a and 6.1b) as gray bands with the 8 mm PEPT data exhibiting wider bands. On average the variation of ϕ appears independent of particle size. An unexpected dip in the volume concentration is noticed for the lowest (40 %) and highest (75 %) critical speeds around the location of the ES. The most likely conclusion is that the PEPT data may be spurious in this region. Excluding the spurious data and combining the plots for both the 5 mm and 8 mm runs across all mill speeds, as done in figure (6.2), the three flow regimes can be delineated as follows:

1. The quasi-static regime is located between the maximum and minimum positions of the ES (denoted as vertical black dashed lines). The corresponding volume fraction range is: $\phi_{qs} \approx 0.6$.
2. The inertial regime is located between the maximum and minimum positions of the FS (denoted as vertical black dashed-dotted lines). The corresponding volume fraction range is: $\phi_i \in [0;\ 0.4]$.
3. The dense (liquid-like) regime is then naturally found between the quasi-static and inertial regime. The corresponding volume fraction range is: $\phi_d \in [0.4;\ 0.6]$.

We note that these conclusions are consistent with the discussion in chapter (4) where only the 5 mm data, operated at 60 % of critical speed, was used. Notably, the 60 % of critical speed configuration is approximately the average speed used in the current PEPT investigations. It is therefore reasonable to expect agreement between the average taken over all data and the average configuration.

6.3 Tangential velocity

Figures (D.3 and D.4) show the tangential velocity distributions of the 5 mm and 8 mm diameter beads respectively. Both particle sizes exhibit similar trends through the thickest region of the bed; see figures (6.3a and 6.3b): Starting at the FS, the velocity decreases to a minimum value at the ES. With further increases in depth, the velocity starts to increase (in the opposite direction) until it matches (approximately) the tangential speed of the lifter bar. The slight dip in the velocity near the drum wall is indicative of possible slip caused by the angled lifter bars. In this regard the 5 mm beads experience wall slip at (40 %, 55 %, 65 %) of critical speed while the 8 mm beads only appear to slip for the 40 % of critical speed. The slip is arguably the source of fluctuations near the wall that ultimately produce spurious PEPT data. This may be the cause of the low volume concentrations measured along the drum wall for both particle sizes.

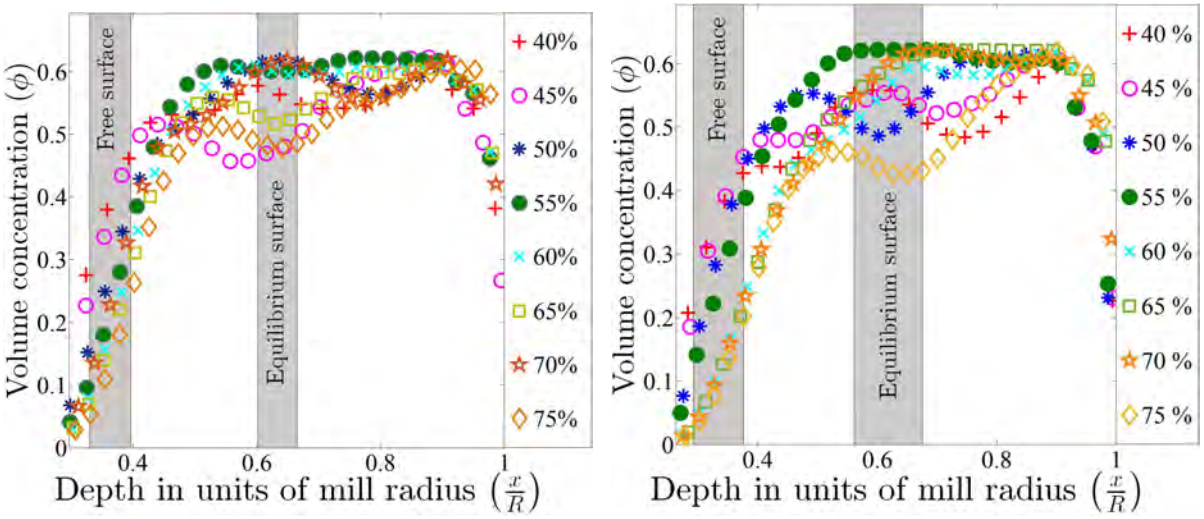

(a) 5 mm diameter glass bead data derived from PEPT.

(b) 8 mm diameter glass bead data derived from PEPT.

Figure 6.1: Variation of volume concentration along the radial line passing through the CoC.

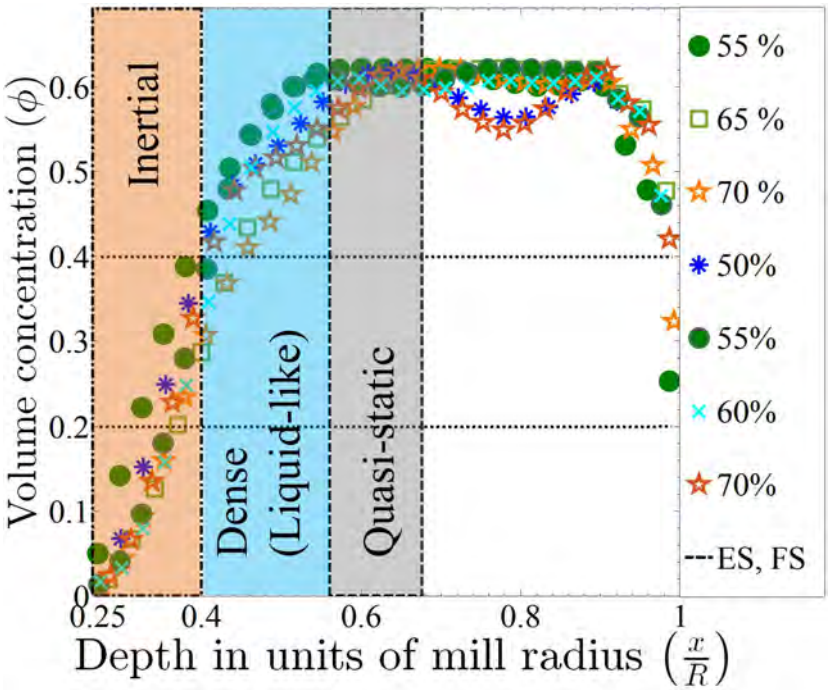

Figure 6.2: Illustration of flow regimes superimposed on the volume concentration data for both the 5mm and 8mm glass beads across all speeds investigated. The highest (75 %) and lowest (40 %) speed data have been removed due to unrealistic ϕ-values about the ES.

6.4 Shear rate

Figures (D.5 and D.6) show the azimuthal distribution of the shear rate for the 5 mm and 8 mm beads respectively. Along the line passing through the CoC, the following is discerned

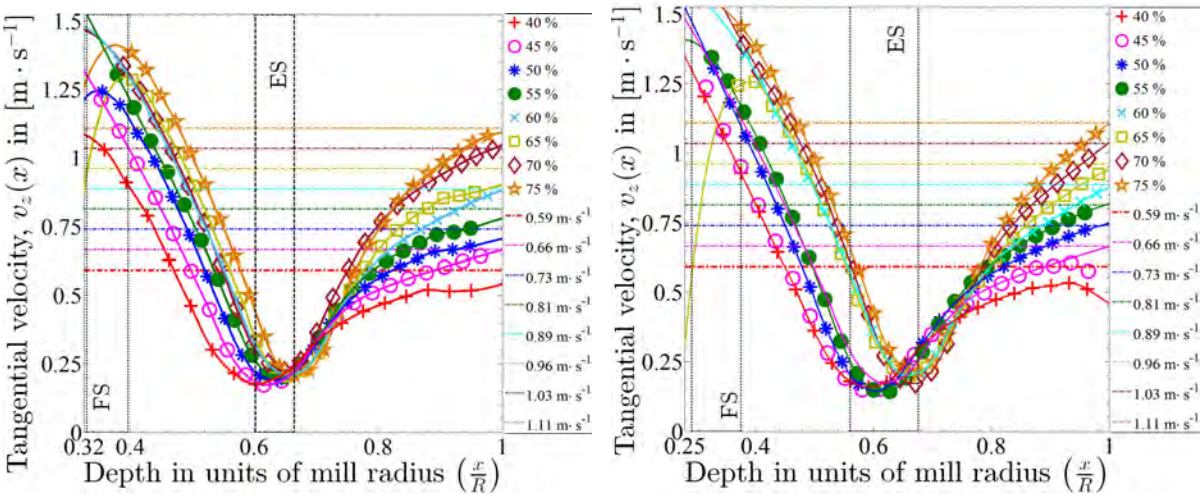

(a) 5 mm diameter glass bead data derived from PEPT.

(b) 8 mm diameter glass bead data derived from PEPT.

Figure 6.3: Variation of tangential velocity along the radial line passing through the CoC. The horizontal lines denote the tangential speed of the drum for the corresponding PEPT data. In the absence of slip between the drum and the glass beads the respective PEPT data profiles intersect (or come close to) the corresponding horizontal line at $\frac{x}{R} = 1$.

from figures (6.4a and 6.4b):

1. The 8 mm charge produce a non-zero shear rate at the FS for all mill speeds while the 5 mm charge produces $\dot{\gamma}_{5\mathrm{mm}} > 0$ at (45 %, 55 %, 60, %, 70 %) and $\dot{\gamma}_{5\mathrm{mm}} = 0$ for (40 %, 50 %, 65, %, 75 %).
2. Due to slip experienced along the inner wall of the drum, the 5 mm charge exhibits (unrealistically) high shear rates while the 8 mm charge appears to converge towards zero in consistency with the no slip observations made from the velocity data.
3. Both the 5 mm and 8 mm data span a similar shear rate range with average values $\sim 10\ \mathrm{s}^{-1}$. This result is of the same order of magnitude as the scaling result obtained in section (3.2.2): $\langle\dot{\gamma}\rangle \approx 0.25\sqrt{\frac{g}{d}}$.

6.5 Inertial number

Figures (D.7 and D.8) show the azimuthal distribution of the inertial number for the 5 mm and 8 mm beads respectively. Visual inspection of figures (6.5a and 6.5b) suggest that the inertial number varies similarly for the 5 mm and 8 mm PEPT data along the line passing through the CoC. Combining the 5 mm and 8 mm data in figure (6.6) then facilitates the following observations:

1. The inertial regime spans a wide range of the inertial number: $0.1 < I < 0.5$.
2. The dense regime is dominated by low inertial numbers ($I < 0.3$) near the ES. Closer

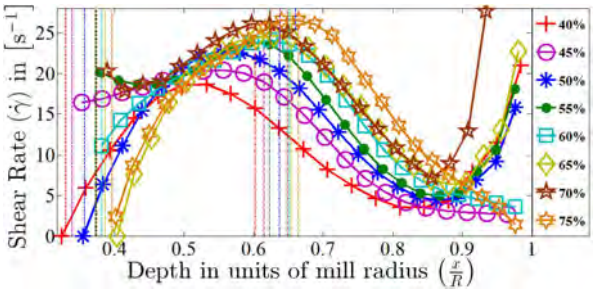

(a) 5 mm diameter glass bead data derived from PEPT.

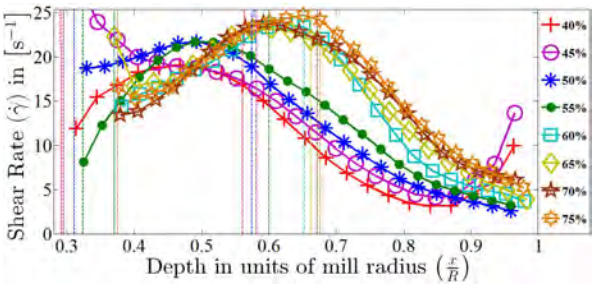

(b) 8 mm diameter glass bead data derived from PEPT.

Figure 6.4: Variation of shear rate along the radial line passing through the CoC.

to the FS, the inertial number grows exponentially to the point that the interface layer becomes statistically indistinguishable by inertial number alone.

3. The quasi-static regime is predominantly at $I \approx 0.1$ with a relatively large variance that makes the interface layer (between quasi-static and dense) statistically difficult to delineate. It is precisely these large variances that make granular flows difficult to quantify and clearly classify.

4. The 5 mm and 8 mm data are statistically equivalent in terms of the inertial number variation along the thickest region of the bed.

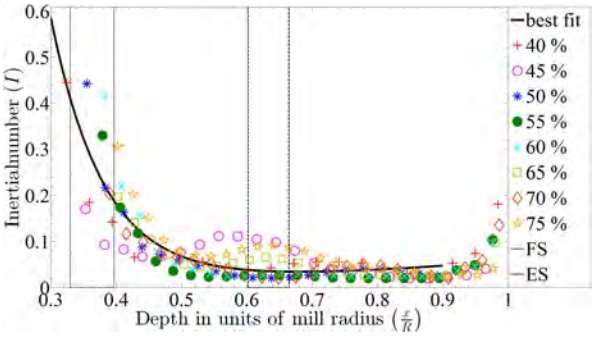

(a) 5 mm diameter glass bead data derived from PEPT.

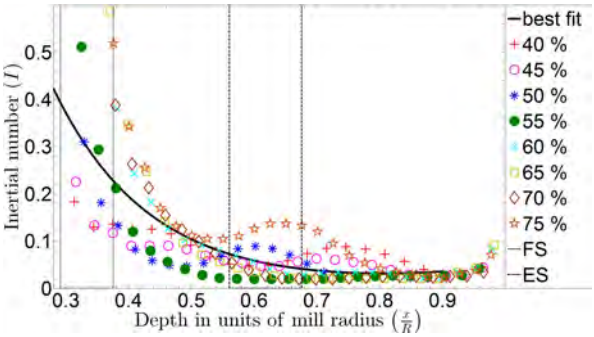

(b) 8 mm diameter glass bead data derived from PEPT.

Figure 6.5: Variation of inertial number along the radial line passing through the CoC.

6.6 Stress

Figures (6.7 and 6.8) show the normal ($P_c,\ P_s,\ P_t,\ P$) and shear ($\tau_c,\ \tau_s,\ \tau_t,\ \tau$) stresses along the depth profile passing through the CoC for all drum speeds employed in studying the granular flow of the 5 mm and 8 mm charge respectively. To facilitate the ensuing discussion, we delineate the profile into the usual four regimes as follows:

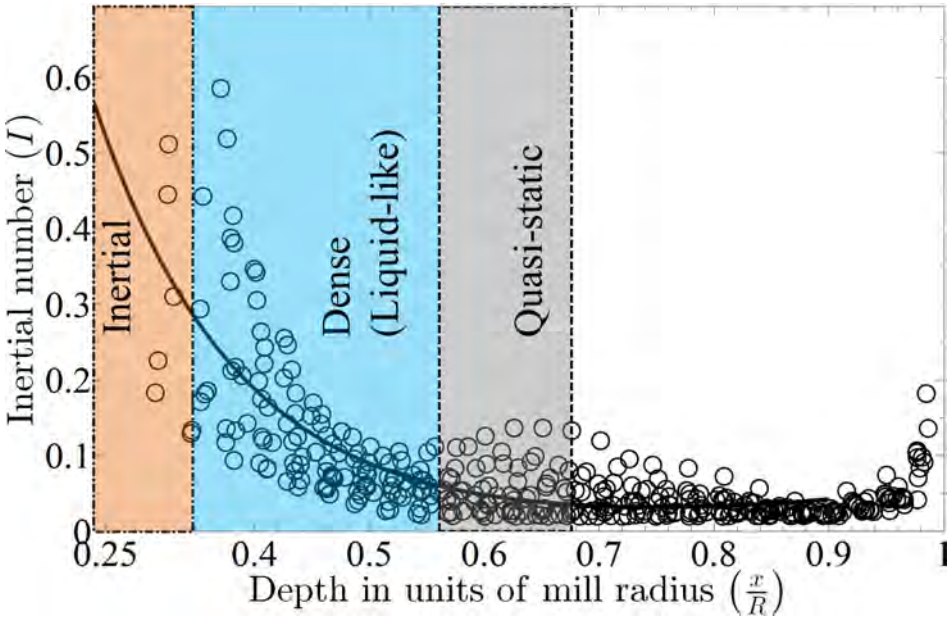

Figure 6.6: Illustration of flow regimes superimposed on the inertial number profiles derived from both the 5mm and 8mm glass beads across all drum speeds investigated.

1. The region falling between the maximum and minimum radial positions of the ES (vertical black dotted lines) denote the quasi-static regime.
2. The region falling between the maximum and minimum radial positions of the FS (vertical black dashed-dotted lines) denote the (pure) inertial regime.
3. The region lying between maximum radial position of the FS and minimum radial position of the ES defines the dense (liquid-like) regime.
4. Radial locations greater than that of the maximum ES define the plug flow regime.

Along the aforementioned radial line, the following conclusions may be drawn:

1. the average normal stress $\langle p \rangle$ dominates over the average shear stress $\langle \tau \rangle$ by a factor of approximately three, i.e. $\langle p \rangle \sim 3\langle \tau \rangle$.
2. The maximum stress occurs about the interface between the quasi-static and liquid-like regime.
3. The inertial regime is comprised almost entirely of turbulent stresses albeit relatively small contributions.
4. The stresses at the free surface (FS) are very small, but arguably not zero.
5. To a first order approximation, the stress profile in each flow regime varies linearly with depth.
6. The inertial number drops exponentially from the free surface to the bottom of the dense regime for all data investigated. Going deeper into the bed (across the quasi-static and so-called plug flow regime), the inertial number appears to remain constant. Accordingly, the collisional stresses in these regions are small and vary very little.

7. The region about the lifter bars is characterised by a slight increase in stresses relative to the rest of the plug flow regime for the 5 mm data. The 8 mm data is less susceptible to this increase. Given that slip is more prevalent in the 5 mm data than the 8 mm data, it is reasonable to assume that the cause of the sudden increase in stresses is largely influence by slip.

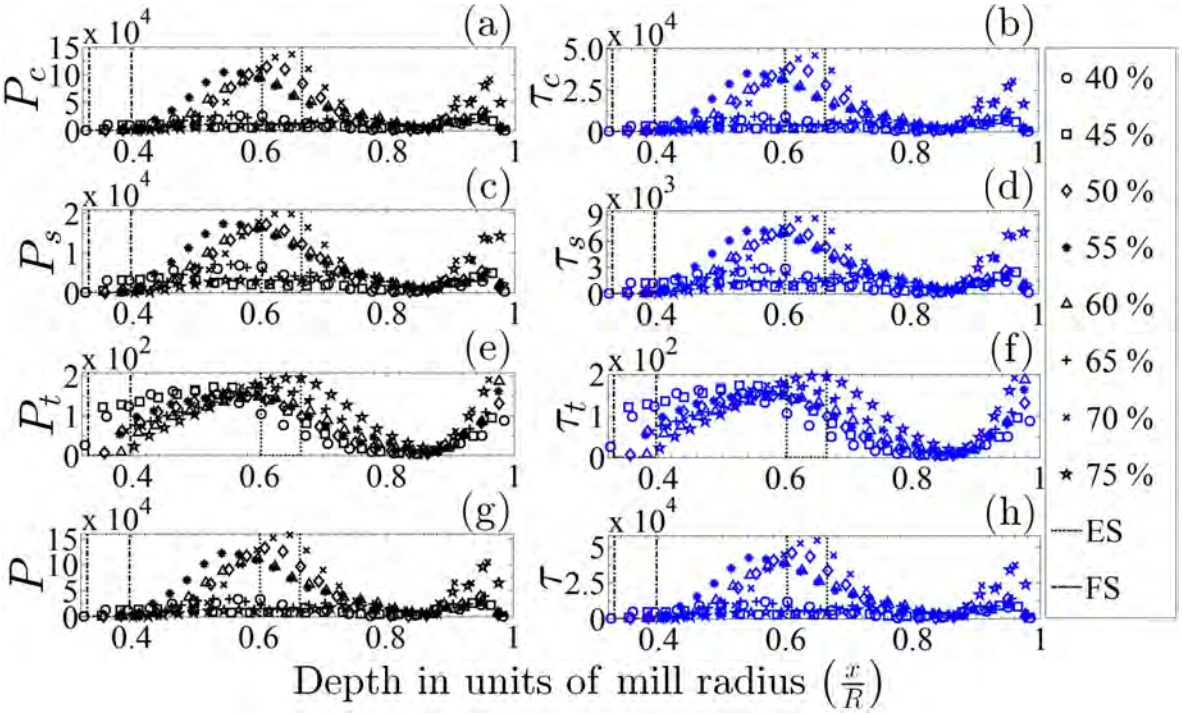

Figure 6.7: Shear and normal stress profiles along the radial line passing through the CoC for the 5 mm glass bead data.

The effective friction coefficient $\left[\mu(x) = \frac{\tau(x)}{p(x)}\right]$ clearly captures the relative contribution of shear and normal stresses to the granular rheology; see figure (6.9). The dense (liquid-like) regime is characterised by an essentially constant value of $\mu(x) \approx 0.35$. The same value persists into the quasi-static regime. The inertial regime is characterised by an exponential growth in $\mu(x)$ in the range $0.35 < \mu(x) < 0.65$. This is not surprising given the strong dependence of the $\mu(x)$ with $I(x)$; cf. Orpe and Khakhar (2007) who get $\mu_{\text{ES}} \approx 0.3$ at the bottom of dense flowing layer and $\mu_{\text{FS}} \approx 0.6$ at the free surface.

6.7 Power dissipation

The power density due to the shear and normal components of the stress are given in figures (6.10 and 6.11) for the usual radial profile employed in this work. The following observations are made:

1. For the 5 mm glass bead data:
   (a) $\langle \frac{\partial^3 B_{\text{normal}}}{\partial x \partial y \partial z} \rangle = 5.8 \times 10^4 \ \frac{\text{W}}{\text{m}^3}$

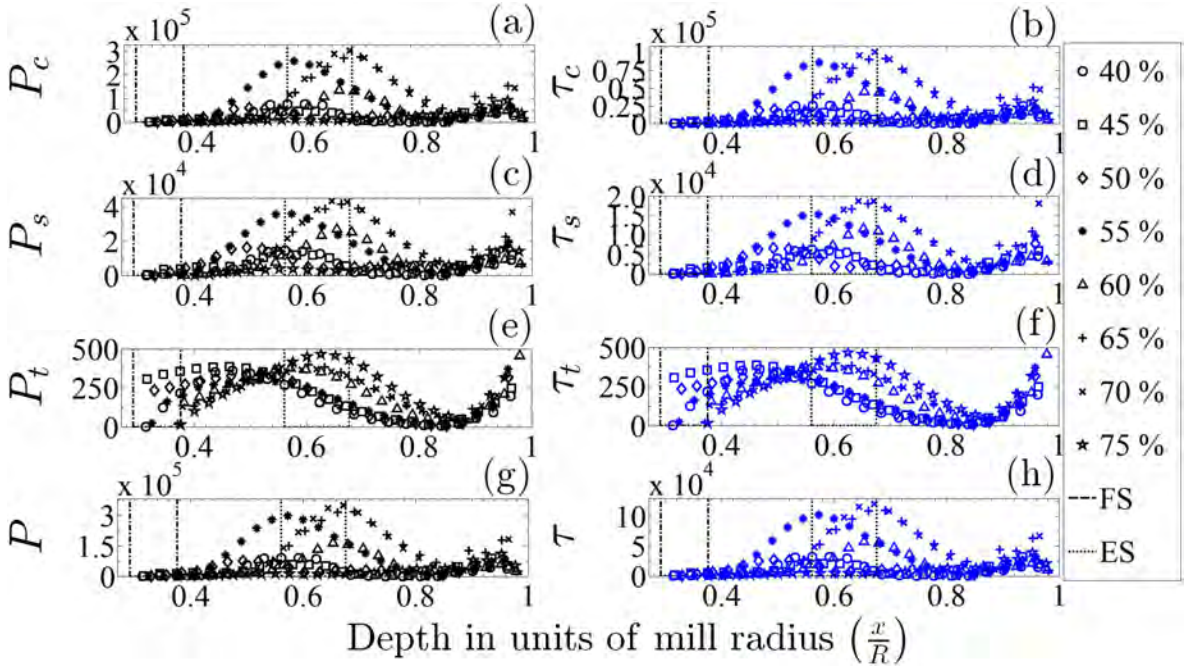

Figure 6.8: Shear and normal stress profiles along the radial line passing through the CoC for the 8 mm glass bead data.

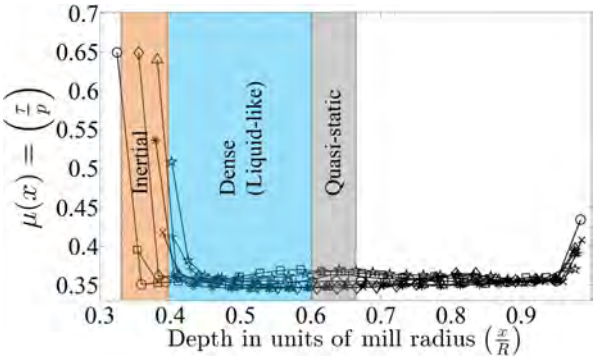

(a) 5 mm diameter glass bead data derived from PEPT.

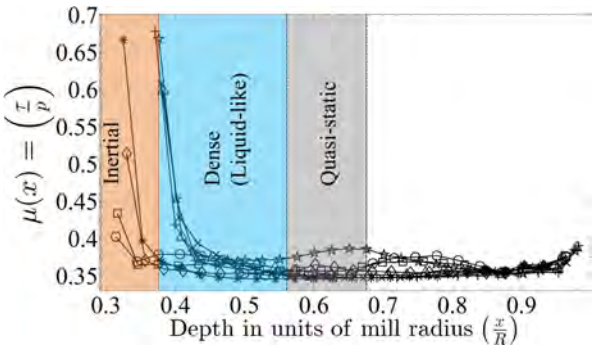

(b) 8 mm diameter glass bead data derived from PEPT.

Figure 6.9: Variation of the effective friction coefficient $\mu(x)$ along the radial line (oriented at angle θ to the horizontal) passing through the thickest region of the flow.

(b) $\langle \frac{\partial^3 B_{\text{shear}}}{\partial x \partial y \partial z} \rangle = 5.1 \times 10^5 \ \frac{\text{W}}{\text{m}^3}$

(c) Shear power density is maximised at the interfaces between flow regimes with a (surprising) maximum achieved by the 55 % critical speed.

(d) Normal power density is relatively flat across the flow regimes, except for the 55 % and 70 % critical speeds that peak respectively in the dense and quasi-static regimes.

2. For the 8 mm glass bead data:

(a) $\langle \frac{\partial^3 B_{\text{normal}}}{\partial x \partial y \partial z} \rangle = 5.3 \times 10^4 \ \frac{\text{W}}{\text{m}^3}$

(b) $\langle \frac{\partial^3 B_{\text{shear}}}{\partial x \partial y \partial z} \rangle = 6.5 \times 10^5 \ \frac{\text{W}}{\text{m}^3}$

(c) Shear power density grows rapidly from the inertial regime, peaks in the dense (for lower speeds) and quasi-static (for higher speeds), and then drops off rapidly in the plug flow regime.

(d) Normal power density remains relatively low and flat from the inertial to quasi-static regimes. At around the interface between the quasi-static and plug flow regimes it suddenly grows with peaks occurring in the plug flow regime.

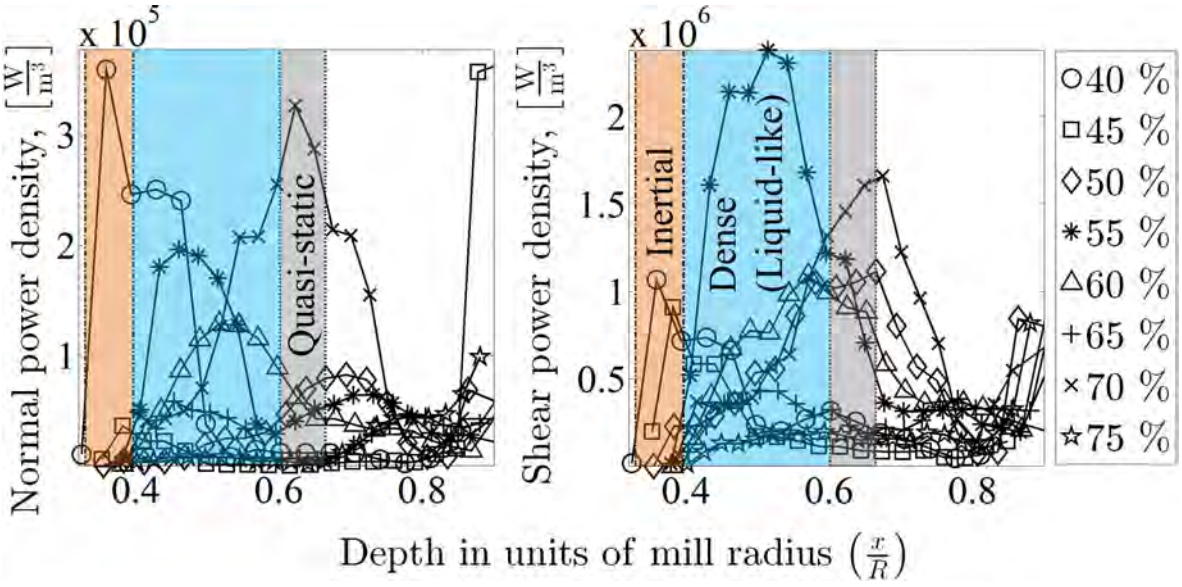

Figure 6.10: Power density of 5 mm glass beads

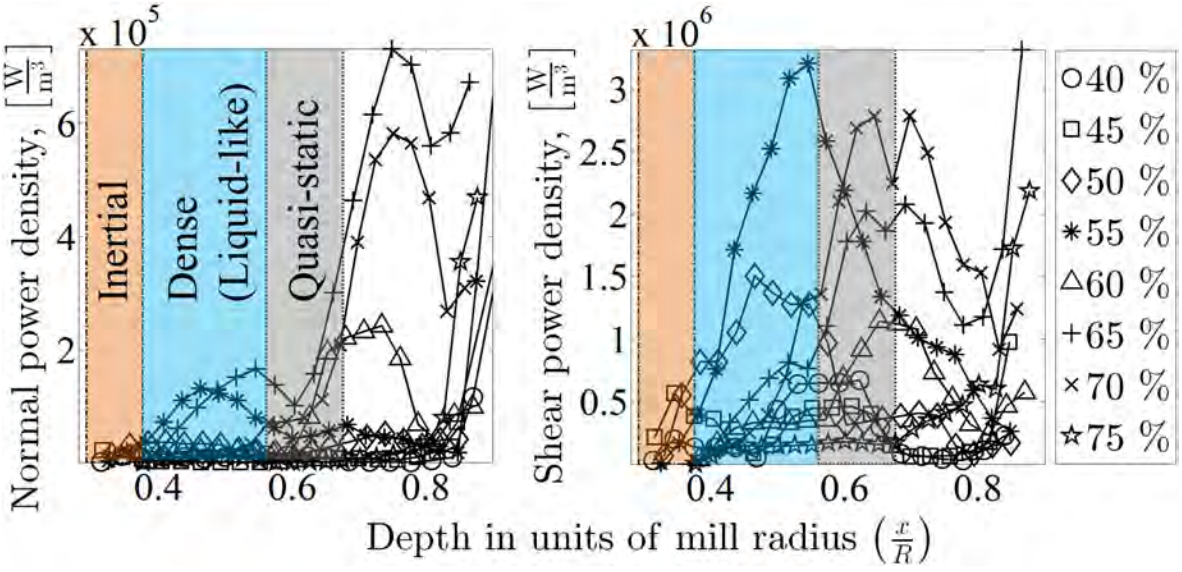

Figure 6.11: Power density of 8 mm glass beads

Chapter 7

Conclusions

Positron Emission Particle Tracking (PEPT) was successfully employed to study the flow of 5 mm and 8 mm glass beads in an experimental tumbling mill fitted with angled lifter bars and operated in the speed range $40:5:75$ % of critical speed. The resulting trajectory information was repackaged into a continuum description with a suitable representative volume element (RVE) of dimensions $(5 \times 5 \times 480)$ mm^3. The kinematics and volume concentration per RVE were determined using Lagrange interpolation polynomials and the methodology of Wildmann et al. (2000) respectively.

The flowing layer exhibited stream-wise flow that conformed to the scaling law: $\langle v_t \rangle \propto h^{0.86\pm0.04}$ which is similar to that obtained by Midi (2004). The associated average shear rate under linear scaling conditions is given by $\langle \dot{\gamma} \rangle \approx 0.25\sqrt{\frac{g}{d}}$.

An inspection of the volume concentration (ϕ) variation through the thickest part of bed strongly suggested the existence of (i) a quasi-static regime ($\phi \approx 0.6$), (ii) a dense (liquid-like) regime ($0.4 < \phi < 0.6$) that allowed for frictional- and collisional-type stresses, (iii) and a purely inertial regime ($\phi < 0.4$) that has negligible stress chains and is dominated by collisions, albeit very few given the low concentration. The rising regime was assumed to follow plug flow. The observed turbulent toe region of the bed, coupled with the notion that the associated propagation length could be large given that the cataracting stream interacts chaotically with the entire free surface, facilitated the introduction of a turbulent stress into the ensuing granular rheology formulation.

Incorporating the inertial number (I) dependence into our formulation, we propose an empirical model for the variation of the volume concentration: $\phi(I) = \phi_{\max} \exp(-bI^c)$, with ($b = 1.348$) and ($c = 0.6014$) chosen carefully to match both the present data and leading experimental observations of Orpe and Khakhar (2007). The resulting rheology includes the local rheology of Jop et al. (2006) for the internal frictional stresses in densely flowing regions, the kinetic-collisional stresses in the dense and inertial regimes as popularised by Bagnold (1954) and a turbulent stress inspired by many authors [Takahashi (2009), Hotta (2012), Suzuki et al. (2003), Ashida et al. (1985)] to successfully recover the effective friction coefficient:

$$\mu(I) = \mu_i(I)\left[1 - 3\lambda^2 I^2 - k_t\phi\left(\frac{1-\phi}{\phi}\right)^{\frac{2}{3}} I^2\right] + \mu_w \frac{x}{L}\left[1 - 3\lambda^2 I^2 - k_t\phi\left(\frac{1-\phi}{\phi}\right)^{\frac{2}{3}} I^2\right] + \lambda^2 I^2 + k_t\phi\left(\frac{1-\phi}{\phi}\right)^{\frac{2}{3}} I^2. \tag{7.1}$$

The success of the model is clearly captured in figure (7.1) and related to:

1. the smooth prediction of the expected hysteresis at the transition between the quasi-static and dense flow regimes,
2. the smooth prediction of the second phase transition from the dense to gas-like regime, and
3. the realistic average values of the effective friction coefficient ($\langle\mu\rangle$) and the corresponding inertial number ($\langle I\rangle$) predicted at the two phase transitions.

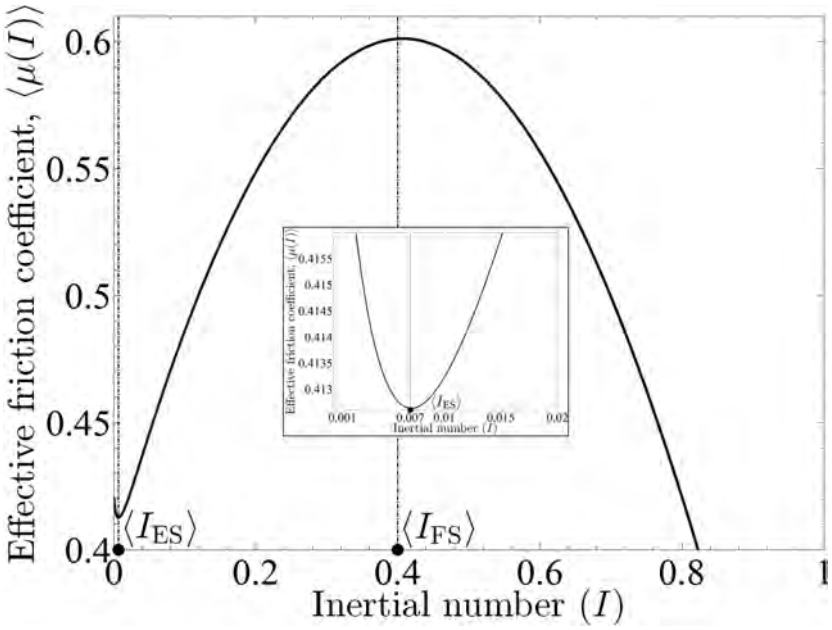

Figure 7.1: A plot of equation (4.29) using average values from table (4.1). The variation of $\langle\mu(I)\rangle$ shows that both phase transitions −from quasi-static to dense flow (see subplot where $\langle I\rangle_{\rm ES} = 0.007$); and from liquid-like to gas-like flow ($\langle I\rangle_{\rm FS} = 0.4$)− are smoothly captured at inertial numbers that correspond to volume concentration measurements derived from PEPT data.

The new rheology was then incorporated into an athermal energy balance to recover the power density due to normal and shear stresses. The model was applied to the existing PEPT data to yield the following main conclusions:

1. Shear power density is an order of magnitude higher than normal power density, suggesting that the dominate mode of flow dissipation is shear. This is largely influenced by the fact that $\frac{v_x}{v_z} \ll 1$. Unfortunately, the extent of the proposed theory does not account for (compressive) stresses above the von Mises yielding limit where we expect

complex loading and stress behaviour to exist. To be clear, the current theories of granular flow [Midi (2004), Jop et al. (2006), Orpe and Khakhar (2007)], and indeed the work presented herein, is strictly valid far below the von Mises limit. The reader is thus cautioned to not infer too much by way of damage or fracture from the proposed description. Rather, the current description should serve as a proxy for where damage (and in general comminution) is most likely to occur.

2. Shear rate and slip have major influences on flow dissipation with the latter often producing non-trivial effects.

3. Lifter bars present a complex frictional surface to the adjacent granular layer, producing high levels of slip for the 5 mm beads and negligible slip for the 8 mm beads.

4. Notwithstanding these complications, the effective rheology, as indicated by the effective friction coefficient $\mu(I, x)$, remains largely the same for both the 5 mm and 8 mm glass beads.

5. Turbulence contributes negligibly to the overall flow dissipation but is nonetheless essential to recovering a heuristically consist rheology for tumbling mills.

6. Although only briefly discussed in section (5.3), the variation of the coherence length through the bed strongly supports the need for a non-local description of granular rheology. This is particular true since the variation does not agree with leading descriptions [Midi (2004)] albeit that these descriptions where not determined in tumbling mill geometries. Future developments in granular flow theory is very likely to incorporate coherence length into the description of length scales.

Finally, future work should aim to extend the range of PEPT experiments to fully span the flow rate regimes not covered in the present work. This is best achieved by using different (possibly smaller) tracer sizes in the PEPT work. The use of tracers smaller than, say, 1 mm in diameter is extremely attractive from a modelling and scaling perspective, but poses a significant challenge to tracer production processes from a durability and track-ability point of view. Drum filling levels can also aid in this endeavour as it ultimately influences the bed depth in the scaling. Assuming that these challenges can be surmounted, an important theoretical step would be towards the development of a constitutive stress ansatz that matches the measured scaling laws. Comparison with full tensorial formulations should also be tackled via Discrete Element Method (DEM) simulations. In this regard, the continuum repackaging schemes described by Goldhirsch (2003) and Andreotti et al. (2013) are very useful in recasting discrete micro-scale information from DEM into continuum descriptions of the full stress tensor. The task is then to interrogate the validity of the constitutive relations developed in this work by comparing them to the full tensorial description. Following a bottom-up approach, PEPT data spanning a wide range of the phase space can be very instructive in distilling out the underlying scaling laws governing the granular rheology of tumbling mills. The scaling laws ultimately dictate the permissible forms of the constitutive relations in the sense that any constitutive choice must yield the law after integration. PEPT Cape Town is uniquely placed to meet this challenge.

Bibliography

Ancey, C., 1999. Dry granular flow down an inclined channel: Experimental investigations on the frictional-collisional regime. J. Rheol 43, 1673–1699.

Ancey, C., Coussot, P., Evesque, P., 1999. A theoretical framework for very concentrated granular suspensions in a steady simple shear flow. J. Rheol 43, 1673–1699.

Andreotti, B., Forterre, Y., Pouliquen, O., 2013. Granular media: Between Fluid and Solid. Cambridge University Press.

Aradian, A., Raphael, E., de Gennes, P.-G., 2002. Surface flows of granular material: A short introduction to some recent models. C.R. Acad. Sci. Ser IV: Phys., Astrophys. 3, 187–197.

Armanini, A., Capart, H., Fraccarollo, L., Larcher, M., 2005. Rheological stratification in experimental free-surface flows of granular-liquid mixtures. Journal of Fluid Mechanics 532, 269–319.

Ashida, K., Egashira, S., Kamiya, H., Sasaki, H., 1985. The friction law and moving velocity of a soil block on slopes. Tech. rep., Kyoto University.

Bagnold, R. A., 1954. Experiments on a Gravity-Free Dispersion of Large Solid Spheres in a Newtonian Fluid under Shear. Proceedings of the American Royal Society of London. Series A, Mathematical and Physical Sciences 225, 49–63.

Bailey, D. L., Karp, J. S., Surti, S., 2005a. Positron Emission Tomography. Springer- Verlag, London.

Bailey, D. L., Townsend, D. W., Valk, P. E., Maisey, M. N. (Eds.), 2005b. Positron Emission Tomography. Springer-Verlag London Ltd.

Bird, R. W., Steward, W. E., Lightfoot, E. N., 2002. Transport Phenomena (Second Edition). John Willy & Sons, Inc, New York.

Bouchaud, J.-P., Cates, M., Prakash, J., Edwards, S., 1994. A model for the dynamics of sandpile surfaces. Journal de Physique I (France) 4, 1383–1410.

Boutreux, T., Raphael, E., de Gennes, P.-G., 1998. Surface flows of granular materials: A modified picture for thick avalanches. Physical Review E 58(4), 4692–4699.

Bridgwater, J., Forrest, S., Parker, D. J., 2004. Pept for Agglomeration? Powder Technology 140(3), 187–193.

Burnham, C. A., Brownell, G. L., 1972. A Multi Crystal Positron Camera. IEEE Transaction on Nulcear Science 19(3), 201–205.

Canny, J., 1986. A computational approach to edge detection. IEEE Transactions on Pattern Analysis and Machine Intelligence PAMI-8, 679–698.

Cho, A. H., Farukhi, M. R., 1977. Bismuth Germanate as a Potential Scintillation Detector in Positron Cameras. Journal of Nuclear Medicine 18, 840–844.

Chou, H.-T., Lee, C.-F., 2009. Cross-sectional and axial flow characteristics of dry granular material in rotating drums. Granular Matter 11, 13–32.

Cortet, P.-P., Bonamy, D., Daviaud, F., Dauchot, O., Dubrulle, B., Renouf, M., 2009. Relevance of visco-plastic theory in a multi-directional inhomogeneous granular flow. European Physical Letters 88, 14001.

da Cruz, F., Emam, M., Prochnow, M.and Roux, J. N., Chevoir, F., 2005. Rheo-physics of dense granular materials. Phys. Rev. E 72, 021309.

de Gennes, P.-G., 1995. Dynamique superficielle d'un materiau granulaire. C.R. Acad. Sci. Ser II b: Surface and interface physics 321, 501–506.

Derenzo, S. E., Budinger, T. F., Cahoon, J. L., Greenberg, L. W., Huesman, R. H., Vuletich, T., 1979. The Donner 280-Crystalrystal High Resolution Positron Tomography. Nuclear Science, IEEE Transactions on 26(2), 2790–2793.

Derenzo, S. E., Huesman, R. H., Cahoon, J. L., Geyer, A. B., Moses, W. W., Uber, D. C., Vuletich, T. F., Budinger, T. F., 1988. A Positron Tomograph with 600 Bgo Crystals and 2.6 mm Resolution. IEEE Transactions on Nuclear Science 35(1), 659–664.

Ding, Y. L., Seville, J. P. K., Forster, R., Parker, D. J., 2001. Solids Motion in Rolling Mode Rotating Drums operated at Low to Medium Rotational Speeds. Chemical Engineering Science 56(5), 1769–1780.

Dormand, J., Prince, P., 1980. A family of embedded runge-kutta formulae. Journal of Computational and Applied Mathematics 6(1), 19–26.

Douady, A., Andreotti, B., Daerr, A., 1999. On granular surface flow equations. The European Physical Journal B 11, 131–142.

Dury, C., Ristow, G., Moss, J., Nakagawa, M., 1998. Boundary effects on the angle of repose in rotating cylinders. Physical Review E 57, 4491–4497.

Elperin, T., Vikhansky, A., 1998. Granular Flow in a Rotating Cylindrical Drum. Europhysics Letters 42(6), 619–623.

Ervin, B., Podgorsak, E. B., 2010. Radiation Physics for Medical Physicists. Springer Heidelberg Dordrecht, London, New York.

Fahlström, H., 1962. Autogenous grinding at assbo. world mining. World Mining 15(10), 28–32.

Fan, X., P. D., Smith, M., 2006. Labelling a Single Particle for Positron Emission Particle Tracking Using Direct Activation and Ion-Exchange Techniques. Nuclear Instruments and Methods in Physics Research A 562, 167–172.

Felix, G., Falk, V., D'Ortano, U., 2007. Granular flows in a rotating drum: the scaling law between velocity and thickness of the flow. Eur. Phys. J. E 22, 25–31.

Fermi, E., 1934. Versuch Einer Theorie Der Beta Strahlen.i. Z.Physics 88 (3-4), 161–177.

Forterre, Y., Pouliquen, O., 2008. Flows of Dense Granular Media. Annu. Rev. Fluid Mech. 40, 1–24.

Goldhirsch, I., 2003. Rapid granular flows. Annu. Rev. Fluid Mech. 35, 267–293.

Govender, I., 2005. X-Ray Motion Analysis of Charge Particles in A Laboratory Mill. Ph.D. thesis, University of Cape Town, Cape Town.

Govender, I., McBride, A., Powell, M., 2004. Improved experimental tracking techniques for validating discrete element method simulations of tumbling mills. Experimental Mechanics 6, 593–607.

Habte, F., Olcott, P. D., Levin, C. S., Foudray, A. M. K., 2005. Investigation of Scintillation Light Multiplexing for PET Detectors Based on Position Sensitive Avalanche Photodiodes. In: IEEE Nuclear Science Symposium Conference Record.

Harris, C., Schnock, E., Arbiter, N., 1985. Grinding mill power consumption. Miner. Process. And technol. Rev. 1, 297–345.

Hartley, R., Schaffalitzky, F., 2004. Minimization in Geometric Reconstruction Problems. Computer Vision and Pattern Recognition 68(2), 504–509.

Hartley, R., Zisserman, A., 2004. Multiple View Geometry in Computer Vision. Cambridge University Press, U.K.

Hatano, T., 2007. Power law friction in closely packed granular materials. Phys. Rev. E 75 (6), 060301(R).

Hawkesworth, M. R., O'Dwyer, M., Walker, J., Fowles, P., Heritage, J., Stewart, P., Witcomb, R., Bateman, J., Connolly, J., Stephenson, R., 1986. A positron camera for industrial application. Nuclear Instruments and Methods A 253, 145–157.

Henein, H., Brimacombe, J. K., Watkinson, A. P., 1983. Experimental Studies of Transverse Bed Motion in Rotary Kilns. Met. Trans. B 14B, 191–205.

Hogg, R., Feurstenau, D., 1972. Power relationships for tumbling mills. SME-AIME Transactions 252, 418–423.

Hotta, N., 2012. Basal interstitial water pressure in laboratory debris flows over a rigid bed in an open channel. Nat. Hazards Earth Syst 12, 2499–2505.

Humm, J. L., Rosenfeld, A., Guerra, A., 2003. From PET Detectors to PET Scannars. European Journal of Nuclear Medicine and Molecular Imaging 30, 1574–1597.

Jain, N., Ottino, J.M. abd Lueptow, R., 2002. An experimental study of the flowing granular layer in a rotating tumbler. Physics of Fluids 14 (2), 572–582.

Jenkins, J., Zhang, C., 2002. Kinetic theory for identical, frictional, nearly elastic spheres. Phys. Fluids 14 (3), 1228–1235.

Jenkins, T., Richman, W., 1985. Grads 13-moment system for a dense gas of inelastic spheres. Arch. Rat. Mech. Anal 87, 355–377.

John, M. O., Fessler, J. A., 1997. Positron Emission Tomography. IEEE Singnal Processing Magazine 14(1), 43–55.

Johnson, P., Jackson, R., 1987. Frictional-collisional constitutive relations for granular materials, with application to plane shearing. J. Fluid Mech. 176 (67), 67–93.

Johnson, P., Nott, P., Jackson, R., 1990. Frictional-collisional equations of motion for particulate flows and their application to chutes. Journal of Fluid Mechanics 210, 501–535.

Jop, P., Forterre, Y., Pouliquen, O., 2005. Crucial role of side walls for granular surface flows: consequences for the rheology. J. Fluid Mech. 541, 167–192.

Jop, P., Forterre, Y., Pouliquen, O., 2006. A constitutive Law for Dense Granular Flows. Nature 441(8), 727–730.

Josserand, C., Lagree, P., Lhuillier, D., 2006. Granular pressure and the thickness of a layer jamming on a rough incline. Europhysics Letters 73, 363–369.

Kamrin, K., Kovall, G., 2012. Nonlocal constitutive relation for steady granular flow. Physical Review Letters 108(17), 178301–5.

Khakhar, D. V. V., Mccarthy, J. J., Shinbrot, T., Ottino, J. M., 1997. Transverse flow and mixing of granular materials in a rotating cylinder. Physics of. Fluids 9, 31–43.

Lee, C. H., Huang, C. J., 2012. Kinetic theory based model of dense granular flows down inclined planes. Physics of Fluids 24, 073303.

Levin, C. S., Hoffman, E. J., 1999. Calculation of Positron Range and its Effects on the Fundamental Limit of Positron Emission Tomography System Spatial Resolution. Phy. Med. Biol 44, 781–799.

Levin, C. S., Hoffman, E. J., Cherry, S. R., 1997. Ieee Medical Imaging Conference. In: Positron Range Calculation and its Effect on Positron Emission Tomography.

Lun, C., Savage, S., Jeffrey, D., Chpeurniy, N., 1984. Kinetic theory for granular flow: inelastic particles in couette flow and slightly inelastic particles in a general flow field. Journal of Fluid Mechanics 140, 223–256.

Makse, H. A., 1999. Continuous Avalanche Segregation of Granular Mixtures in Thin Rotating Drums. Physical Review Letters 83(16), 3186–3189.

McBride, A., Govender, I., Powell, M., Cloete, T., 2004. Contributions to the experimental validation of the discrete element method applied to tumbling mills. Engineering Computations 21, 119–136.

Meier, S., Lueptow, R., Ottino, J., 2007. A dynamical system approach to mixing and segregation of granular materials in tumblers. Advances in Physics 56(5), 757–827.

Mellmann, J., 2001. The Transverse Motion of Solids in Rotating Cylindersforms of Motion and Transition Behavior. Powder Technology 18(3), 251–270.

Midi, G. D. R., 2004. On dense granular flows. Eur. Phys. J. E 14, 341–365.

Morrell, S. ., 1992. Prediction of Grinding Mill Power. Trans. Inst. Min. Metall. (Section C:Mineral Process. Extr. Metall.) 101, C25–C32.

Morrison, A., 2012. Using positron emission particle tracking (pept) to investigate the motion of granular media in a laboratory-scale tumbling mill. Master's thesis, Dept. of Physics, University of Cape Town.

Morrison, D., Cleary, W., 2008. Towards a virtual comminution machine. Minerals Engineering 21(11), 770–781.

Moses, W. W., Derenzo, S. E., 1994. Design Studies for a PET Detector Module Using a PIN Photodiode to Measure Depth of Interaction. IEEE Transaction on Nulcear Science 41, 1441–1446.

Moszynski, M., Balcerzyk, M., Czarnacki, W., Kapusta, M., W. Klamra, W., Syntfeld, A., M. Szawlowski, M., 2004. Intrinsic Energy Resolution and Light Yield Nonproportionality of Bgo. IEEE Transactions on Nuclear Science 51(3), 1074–1079.

Mott, N. F., Massey, H. S. W., 1933. The Theory of Atomic Collisions. Clarendon, Oxford.

Murthy, K., Thompson, C. J., Liu-Hinz, C., D., J., 1994. A Study of the Light Output and Energy Resolution of Small BGO crystals. In: In proceeding of: Nuclear Science Symposium and Medical Imaging Conference.

Nakagawa, M., 1994. Axial Segregation of Granular Flows in a Horizontal Rotating Cylinder. Chemical Engineering Science 49(15), 2540–2544.

Nakagawa, M., Altobelli, S. A., Caprihan, A., Fukushima, 1997. Nmr Measurement and Approximate Derivation of the Velocity Depth Profile of Granular Flow in a Rotating, Partially Filled, Horizontal Cylinder. Powders and Grains 52(23), 447–450.

Nakagawa, M., Altobelli, S. A., Caprihan, A., Fukushima, E., Jeong, E. K., 1993. Noninvasive Measurements of Granular Flows by Magnetic Resonance Imaging. Experiments in Fluids 16(1), 54–60.

Nordberg, K., 2009. The Triangulation Tensor. Computer Vision and Image Understanding 113(9), 935–945.

Oliensis, J., 2002. Exact Two-Image Structure From Motion. IEEE Transactions on Pattern Analysis and Machine Intelligence 24(12), 1618–1633.

Orpe, A. V., Khakhar, D. V. V., 2001. Scaling relations for granular flow in quasitwo-dimensional rotating cylinders. Physical Review E 64(3), 1–13.

Orpe, A. V., Khakhar, D. V. V., 2007. Rheology of surface granular flows. Journal of Fluid Mechanics 571, 1–32.

Parker, D., Dijkstra, A. E., Martin, T. W., Seville, J. P. K., 1997. Positron emission particle tracking studies of spherical particle motion in rotating drums. Chemical Engineering Science 52 (13), 2011–2022.

Parker, D. J., Broadent, C. J., Fowles, P., Hawkesworth, M. R., McNeil, G. T., 1993. Positron emission particle tracking - a technique for studying flow within engineering equipment. Nuclear Instruments Methods in Physics Research 326(3), 592–607.

Peng, H., Levin, C. S., 2012. Study of pet intrinsic spatial resolution and contrast recovery improvement for pet mri systems. Phys.Med.Biol. 57, 101–115.

Phelps, M. E., 2006. Physics:Intrumentation and Scanner. Springer, USA.

Phelps, M. E., Hoffman, E. J., Huang, D., Kuhl, S. C., 1978. A new computerized tomographic imaging system for positron-emitting radiopharmaceuticals. Jounal of Nuclear Medicne 19(6), 635–647.

Pignatel, F., Asselin, C., Krieger, L., Christov, I., Ottino, J., Lueptow, R., 2012. Parameters and scalings for dry and immersed granular flowing layers in rotating tumblers. Physical Review E 86(1), 001304–12.

Pouliquen, O., 1999. Scaling laws in granular flows down rough inclined plane. Physics of Fluids 11(3), 542–548.

Pouliquen, O., Cassar, C., Jop, P.and Forterre, Y., Nicolas, T., 2006. Flow of dense granular material: Towards a simple constitutive laws. Journal of Statistical Mechanics 2006, 7–20.

Pouliquen, O., Chevoir, F., 2002. Dense flows of dry granular material. C. R. Physique 3, 163–175.

Pouliquen, O., Forterre, Y., 2002. Friction law for dense granular flows: Application to the motion of a mass down a rough inclined plane. J. Fluid Mech 453, 133–151.

Powell, M. S., McBride, T., Govender, I., 2003. Application of dem outputs to refining applied sag mills mode. Proceedings International Mineral Processing Congress (IMPC) XXII 1, 325–334.

Puri, S., Hayakawa, H., 1999. Dynamical Behaviour of Rotated Granular Mixtures. Physica A: Statistical Mechanics and its Applications 270(1-2), 115–124.

Rajchenbach, J., 1990. Flow in Powders: From Discrete Avalanches to Continuous Regim. Physical Review Letters 65(18), 2221–2225.

Rogovin, Z., Herbst, J., 1989. Charge motion in a semi-autogeneous grinding mill. Minerals and Metallurgical Processing 6, 18–23.

Rose, H., Sullivan, R., 1957. A treatise on the Internal Mechanics of Ball, Tube and Rod mills. Constable, London.

Roufail, R., Klein, B., Radziszewski, P., 2012. Morphological Features and Discrete Element Method (Dem) Forces Produced in High Speed Stirred Mill. In: Xxvi International Mineral Processing Congress (IMPC) Proceedings.

Roux, J. N.and Combe, G., 2002. Quasistatic rheology and the oorigin of strain. Comptes Rendus Physique 3(2), 131–140.

Rycroft, C., Kamrin, K., Bazant, M., 2009. Assessing continuum postulates in simulations of granular flow. Journal of the mechanics and physics of solids 57, 828–839.

Saha, G. B., 2004. Basics of PET Imaging. Springer Science Business Media, USA.

Saha, G. B., 2010. Basics of PET Imaging (Second Edition). Springer New York Dordrecht Heidelberg London.

Santomaso, A., Ding, Y., Lickiss, J., York, D., 2003. Investigation of the granular behaviour in a rotating drum operated over a wide range of rotational speed. Transactions of the Institute of Chemical Engineers 81, 936–945.

Savage, S., 1998. Analysis of slow high-concentration flows of granular materials. J. Fluid Mech 377, 1–26.

Savage, S., Hutter, K., 1998. The motion of a finite mass of granular material down a rough incline. J. Fluid Mech 199, 177–215.

Savage, S. B., 1984. The mechanics of repid flows. Adv. Appl. Mech. 24, 289–366.

Sepulveda, N., Krstulovic, G., Rica, S., 2005. Scaling laws in granular continuous avalanches in a rotating drum. Physica A: Statistical Mechanics and its Applications 356, 178–183.

Shuyan, W., Xiang, L., Huilin, L., Long, Y., Dan, S., Yurong, H., Yonglong, 2009. Numerical simulations of flow behavior of gas and particles in spouted beds using frfriction-kinetc ststress model. Power Technology 196, 184–193.

Suzuki, T., Hotta, N., Miyamoto, K., 2003. Influence of riverbed roughness on debris flows. J. Erosion Contr. Eng 56, 5–13.

Taberlet, N., Richard, P., Hinch, E. J., 2006. S Shape of a Granular Pile in a Rotating Drum. Physical Review E 73 (5), 3–6.

Taberlet, N., Richard, P., Valance, A., Losert, W., Pasini, J. M., Jenkins, J. T., R., D., 2003. Superstable Granular Heap in a Thin Channel. Physical Review Letters 91(26), 264301.1–264301.5.

Takahashi, T., 2009. A Review of Japanese Debris Flow Research. International Journal of Erosion Control Engineering 2(1), 1–14.

Tordesillas, A., Arber, D., 2005. Capturing the s in segregation: a simple model of flowing granular mixtures in rotating drums. International Journal of Mathematical Education in Science and Engineering Computations 36 (8), 861–877.

Wildmann, R., Huntley, J., Hansen, J.-P., Parker, D., Allen, D., 2000. Single-particle motion in three dimensional vibrofluidised beds. Phys. Rev. E 62, 3826–3835.

Wills, A., 1997. Mineral processing technology: an introduction to the practical aspects of ore treatment and mineral recovery. Oxford.

Wu, C. S., Moskowski, S. A., 1966. Beta Decay. Interscience, Now York.

Yamane, K., Nakagawa, M., Altobeli, S. A., Tanaka, T., Tsuji, Y., 1998. Steady Particulate Flows in a Horizontal Rotating Cylinder. Physics of Fluids 10, 1419–1427.

Yao, S., Lin, W., Ong, P., Lu, Z., 2005. Contrast signal to noise ratio for image quality assessment. Image Processing, 2005. ICIP 2005. IEEE International Conference 1, 397–400.

Zik, O., Levine, D., Lipson, S. G., Shtrikman, S., Stavans, J., 1994. Rotational Induced Segregation of Granular Materials. Physical Review Letters 73(5), 644–649.

Appendix A

Theory of Positron-Electron Annihilation

The positron was first postulated by Paul A.M. Dirac in 1928. Its existence was subsequently confirmed experimentally by Carl Anderson in 1932. Both Dirac and Anderson were awarded the Nobel Prize in physics for their notable contributions to the scientific world. Consequently, this momentous discovery resulted in extensive developments within the branches of physics and mathematical sciences. The interaction of a positron with matter has the perculiar result of producing two photons moving in opposite directions each with an energy of 511 keV. This phenonemon occurs within a material into which a positron emitting radionuclide is inserted.

A.1 The Positron

The positron is the anti-particle conjugate of the electron, emitted in a β^{-1} decay. Positrons are produced by two processes; namely, pair production, and nuclear transmutation. My focus will be solely on the latter of these two processes.

A.2 Nuclear Transmutation

Positrons are positively charged particles that are emitted from the parent nucleus as a by-product of radioactive decay. Positrons which emerge from the parent nucleus are not mono-energetic; rather, they exhibit a continuous spectrum of kinetic energy, with a maximum, $[Q_{max}]$, consistent with the positron decay energy [Ervin and Podgorsak (2010)]. The observation of this continuous energy spectrum was interpreted as a glaring violation of the energy conservation law. Resolving this blatant violation proved highly intractable for several years. In 1930, Pauli postulated the presence of the neutrino in order to explain the continuous energy spectra observed for both electrons and positrons produced in beta decay. Fermi developed the theory of beta decay in 1934, and coined the term neutrino. Given the emission of this third particle; namely, the neutrino or antineutrino, the apparent momentum and energy violation of the decay process was resolved [Ervin and Podgorsak (2010)]. Both the

neutrino and antineutrino were expected to have essentially zero rest masses, neutral charge and move at the speed of light. They were also expected to be exclusively associated with weak-interactions; hence, confirming their existence would prove extremely difficult. Notwithstanding these considerations, several experimental procedures were blueprinted in order to confirm the existence of the neutrino particle, supposedly produced during Fermi's beta decay.

$$ {}^{Z}_{A}X \rightarrow {}^{Z-1}_{A} Y + {}^{1}_{0}\beta^{+} + \nu + Q \tag{A.1} $$

where Q is the energy released during the decay process. The parent atom, X, is proton rich and decays to a less volatile state with the conversion of a proton into a neutron. Having emitted from the parent nucleus, the energy of the positron changes from its initial value to other continuous energies distributed over a smooth continuum. The peak value of the continuum delineates the maximum possible energy of the emitted positron. Upon emission from the parent nucleus, the kinetic energy of the positron decreases due to Coulomb interactions with the surrounding matter. Consequently the positron deviates from its initial trajectory due to these electromagnetic interactions, which are classified into the following two major types:

1. Interactions with atomic electrons are categorised into inelastic and elastic scattering. Inelastic collisions are the dominant mechanism via which the positron's kinetic energy is decreased.

2. Similarly, the interactions with nuclei are categorised into inelastic scattering and elastic scattering.

The probability of an emitted positron, $N(E)$, assuming a value within the energy range, $(E, E + dE)$, per unit time, is determined by the Fermi function, the coupling strength between the initial and final states of the decay process, the shape factor and the atomic number of the daughter nucleus [Fermi (1934)].

$$ N(E) = \frac{GE}{c^5} p(E_0 - E)^2 F(Z_d, E) |M_{fi}|^2 S(K, K_\nu) \tag{A.2} $$

where Z_d is the atomic number of the daughter nucleus, E_0 is the energy of the emitted positron, G is the coupling constant, and c is the speed of light. The Fermi function, $F(Z_d, E)$, accounts for the Coulomb interaction between the daughter and the emitted positron. Actually, the Coulomb field of the daughter nucleus accelerates the positron emitted from the parent nucleus. $|M_{fi}|$ is the matrix element which represents the allowed transitions and the strength thereof. The shape factor $S(K_l, K_\nu)$ ameliorates the matrix element for the forbidden mode of decay. $p(E_0 - E)^2$ is the statistical factor obtained from the density of the final states of the emitted particles. The relativistic Fermi function or Coulomb correction factor, in terms of positron energy, E, and momentum, p, is given by [Fermi (1934)]:

$$ F(Z, E) = \left[\frac{2(1 + H)}{2H!}\right] (2pw)^{2H-2} e^{\pi\xi} |(H - 1 + i\xi)!|^2 \tag{A.3} $$

where the constant H for a given decay is described in terms of the fine structure constant α:

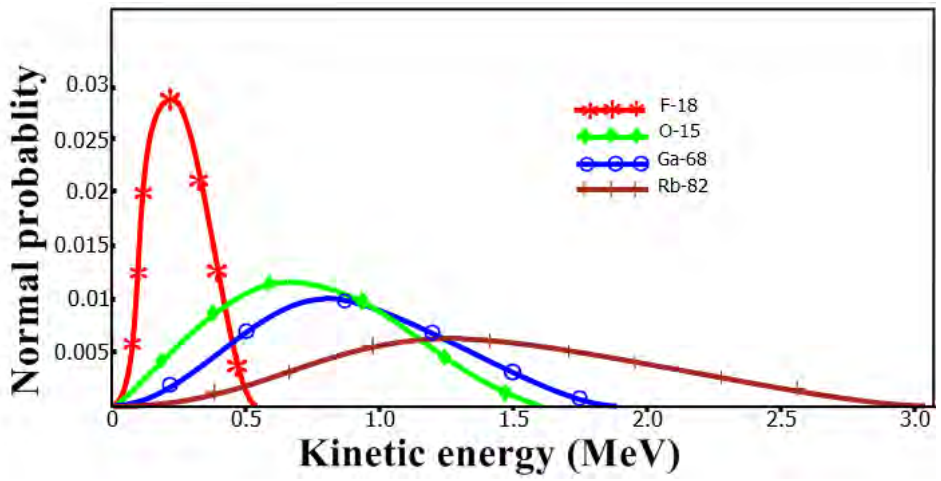

Figure A.1: The theoretical distribution of positron emission energy spectra after normalization.

$$H = \left(1 - \alpha^2 Z^2\right) \tag{A.4}$$

and the constant w is expressible in terms of the nuclear radius, R, the mass of the positron, m, and Planck's constant, h:

$$w = \frac{2Rmc}{h} \tag{A.5}$$

also the constant ξ is defined as a dependency of velocity of the positron V as:

$$\xi = -\frac{2mZe^2}{hV} \tag{A.6}$$

where V is the velocity of the emitted positron. Therefore, in the relativistic case, the Fermi function is based on the atomic number of the daughter nucleus, the kinetic energy of the emitted positron, and the fine structure constant. The Fermi function for the non-relativistic case is given by [Mott and Massey (1933)]:

$$F\left(Z, E\right) = \frac{2\pi\xi}{\left(1 - e^{-2\pi\xi}\right)} \tag{A.7}$$

Evidently, for the non-relativistic case, the Fermi function is dependent on both the atomic number of the daughter nucleus and the kinetic energy of the emitted positron. The energy spectrum of the emitted positron is derived analytically by [Peng and Levin (2012)], using the method developed by [Wu and Moskowski (1966)].

The normalised spectra of emitted positrons from ^{18}F, ^{15}O, ^{68}Ga and ^{82}Rb are illustrated in figure (A.1).

A.3 Features of the Positron Decay

Generally, positron emitters are utilised in nuclear medicine in order to produce more precise functional images of the organs and for the investigation of the physical properties of solids by means of an imaging method-employing particle tracking-called positron emission tomography (PET). PET images play a vital role in medical imaging as they accumulate detailed information about the metabolic functions of organs, based on the activity of a radionuclide injected into the patient. The positrons emitted from the target organ have an extremely short mean free path; consequently, they successfully interact with the tissue of the organ, annihilating with electrons to produce gamma photons. The gamma photons emanating from the organ, as a consequence of these annihilations, are exploited for usage in image processing. Radionuclides utilized in PET scanning are produced via the process of bombardment, during which a stable nuclide is bombarded with high energy protons emitted from a cyclotron. The preferred radionuclide, depends on the time of scanning required to obtain a sufficient number of images and on the organ to be scanned. Similarly, the preference of radionuclide in engineering physics is based on the time required to extract detailed information from the tracking of the radionuclide-particle or tracer particle and the half-life of said tracer.

A.4 Decay Energy of Positron

The energy Q of the emitted positron from a parent nucleus is given by:

$$Q = \{M\,(Z, A) - M\,[(Z-1, A) + 2m_e]\}c^2 \tag{A.8}$$

where $M\,(Z, A)$ and $M\,(Z-1, A)$ are the atomic mass of the parent nucleus and daughter nucleus, respectively. The binding energy of the electron with the nucleus is assumed to be negligible. For positron emission to occur, the following condition must be satisfied:

$$M(Z, A)c^2 > M(Z-1, A)c^2 + 2m_e c^2 \tag{A.9}$$

where $m_e c^2 = 0.511$ MeV is the rest mass energy of emitted positron.

A.5 Positron Emission from ${}^{7}_{13}N$

The decay mode of parent nucleus of ${}^{7}_{13}N$ into daughter nuclei ${}^{6}_{13}C$ is given by:

$${}^{7}_{13}N \rightarrow {}^{6}_{13}\,C + {}^{1}_{0}\,\beta^{+} + \nu_e + Q\,(1.2\text{ MeV}) \tag{A.10}$$

The half-life time of a positron from the decay of ${}^{7}_{13}F$ to ${}^{6}_{13}C$ is approximately 10 minutes. Ammonia is labelled with the ${}^{13}_{7}N$ radionuclide to obtain functional images for the diagnosis of coronary artery disease and myocardial infarction [Peng and Levin (2012)]. Given the half-life time of this radionuclide, the use of ${}^{13}_{7}N$ in PET medical imaging is appropriate;

however, when performing PET imaging in engineering physics, which requires at least an hour of particle tracking in order to obtain a comprehensive description of particle motions, the use of ${}^{7}_{13}N$ is unsatisfactory.

A.6 Positron Emission from ${}^{9}_{18}F$

The decay mode of the ${}^{9}_{18}F$ parent nucleus into ${}^{8}_{18}O$ is given by:

$$ {}^{9}_{18}F \rightarrow {}^{8}_{18}\,O + {}^{1}_{0}\,\beta^{+} + \nu_e + Q\,(0.638\text{ MeV}) \tag{A.11} $$

The half-life time for the conversion of ${}^{9}_{18}F$ to ${}^{8}_{18}O$, via beta decay, is approximately 110 minutes. Fluorodeoxyglucose is labelled with the ${}^{9}_{18}F$ radionuclide to retrieve functional PET images of the human body, for the discovery of potentially malignant diseases and the diagnosis of coronary artery disease as well as myocardial infarction [Peng and Levin (2012)]. As discussed, the half-life time of the ${}^{9}_{18}F$ parent nucleus is exploited in several medical imaging routines. Additionally, this half-life time is extremely useful in particle tacking (PEPT) experiments.

Appendix B

Theory of the PEPT technique

B.1 True Coincidence, Scattered Coincidence, Random Coincidences

The three kinds of coincident detection methods that can be employed by detectors during a PEPT experiment are true, random and scatter coincidences.

A *true coincidence* take places when both gamma photons emitted from the same annihilation arrive at the PET detectors in coincidence without experiencing any interactions or energy loss within the field of view (FoV) before being detected [Phelps (2006)]. (The rate of true coincidences increases linearly with the activity of the tracer 8 particle [Saha (2010)]. Given a specified time window, a detector pair will detect such scattered events provided they fall within the predefined energy window. These scattered events reduce the image contrast by adding background noise. Furthermore, the magnitude of scattered events depends on the position of the tracer, the density of the surroundings, the density of the scintillation material, the activity of the tracer and the window size or the window width of the pulse height analyser (PHA). Generally, the use of a pulse height window results in the observation of a large number of scattered events. The scatter to true events ratio is independent of the activity of the tracer, because each individual event varies linearly with the activity [Saha (2004)].

A *scattered coincidence* take place if one or both of the gamma photons emitted from a single annihilation, undergo Compton scattering, within the surrounding medium, before arriving at the PET detectors. The direction of the gamma photon is altered due to the Compton scattering; therefore, it is possible that the subsequent coincidence detection will be assigned to the wrong line of response (LOR). Since these scattered events are detected within the coincidence time window, they diminish the quality or contrast of the images by adding background noise. In a PEPT experiment, the prevalence of these scattering events is altered with the position of the tracer particle in the rotating mill. Furthermore, this scattering depends on the material with which the PET scintillators are manufactured. In addition, the radioactivity of the tracer particle influences the number of observed scattered events, i.e. scattering events increase linearly with the radioactivity.

Random coincidences within a PET scanner are more inclined to occur if opposing paired detectors are characterised by a wide coincidence timing window. Random coincidences take place when unrelated gamma photons, emitted from the trace particle, are detected by a pair of opposing detectors and are temporally adjacent enough to be recorded within the coincidence timing window [John and Fessler (1997)]. In fact, these random coincidences contribute false information to the triangulation process and are consequently called accidental coincidences. The contrast of the PET images is affected by these random coincidences. Evidently, these random coincidences which are artifacts of the experimental procedure produce highly undesirable background counts. Furthermore, it was shown that the rate of random coincidences in a PET scanner is proportional to the square of the current activity level of the tracer particle within the field of view of the scanner [Bailey et al. (2005b), Saha (2010)]. The rate of accidental coincidences can be predicted throughout the scanning process and can therefore be applied in the correcting of the "projected" data. But the correction of projected data impacts the signal to noise ratio, subsequently affecting the image contrast. Therefore, reducing the collection of random coincidences is the only method capable of enhancing the image quality without reducing its signal to noise ratio. This essentially technical procedure can be performed by reducing the timing window, as the probability for the occurrence of random coincidences is proportional to the coincidence timing window as expressed in equation (B.1). Consequently, the signal to noise ratio does not exclusively determine the quality of the images obtained from PET scanner [Yao et al. (2005)]. The rate R of random or accidental events is defined by the following equation:

$$R = 2W_T.C_1.C_2 \tag{B.1}$$

where W_T is the time window and C_1 and C_2 are signal counts rates of detectors on a LOR. The random count rate is measured in nanoseconds and the single counts rates are measured in counts/sec. Therefore, in the correction of coincidence events, these random counts are subtracted from prompt or true events registered by both detectors.

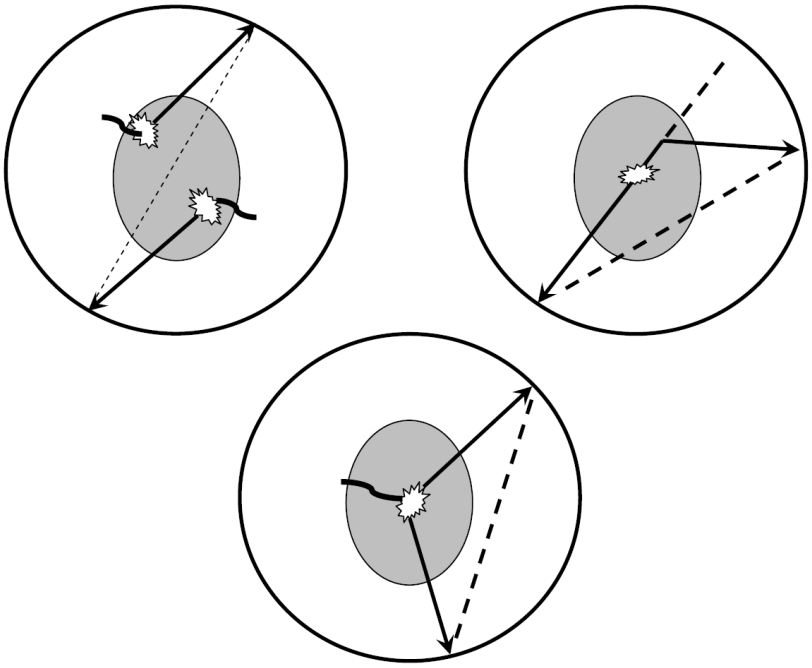

Figure B.1: Degrading effects in PET, from left to right random coincidences, scattered coincidences and prompt gamma coincidences where one of the annihilation photons is detected in coincidence with a prompt gamma photon.

B.2 Energy Resolution

The competence of a detector to differentiate the different energies of radiation relies upon on the energy resolution of the detector. The energy resolution of the scintillation detectors of the PET scanner is a function of the relative light emitted by the detector and its intrinsic energy resolution of the detector. The errors in the energy measurements are governed by the intrinsic energy resolution. PEPT techniques require that the PET scanner has a good energy resolution [Bailey et al. (2005b)].

B.3 Dependency of Sensitivity on Depth of Interaction

The sensitivity of a detector used in a PET scanner, is defined as the competence of the detector to detect coincidence gamma photons emitted from annihilations inside the FoV of the PET scanner. The sensitivity of a PET scanner depends on both its geometry and the stopping power of the scintillation material of which it is comprised [Bailey et al. (2005b)]. A highly sensitive scanner is characterised by a small diameter and large axial FoV. As we know, the stopping power is an intrinsic property of the material used in the PET detector;

consequently, appropriate scintillation should material should be chosen for the detector. The advantage of using a high sensitivity scanner, is that, for a given radioactivity of the FoV, it can accumulate more coincident events within a fixed time interval. As a consequence, these reconstructed PET images a characterised a high signal to noise ratio.

The occurrence of parallax errors in the PET images can be regulated by a thin detector with a higher stopping power. However, on other hand, this thin detector reduces the sensitivity of the PET scanner. Evidently, an accurate measurement of the photon depth of interaction is required to handle this positive correlation between sensitivity and parallax error [Bailey et al. (2005a), Bailey et al. (2005b)].

B.4 Iterative Triangulation

The triangulation is an approach based on mathematics to detect a point, where an annihilation takes place along a line of responses. Detection of a point of an annihilation based on two lines of responses (LoRs) is trivial. It is observed that there are multiplied LoRs which intersect themselves not at a single point in a FoV of a PET scanner. Consequently, it is necessary to introduce a technique in order to enhance the triangulation in the present of noise making events or corrupted events, such as random and scatter coincidences. It is ridiculous to eliminate or separate the scattered and random coincidences from the true coincidences. There were many criteria and error techniques of triangulation introduced in computer vision [Hartley and Schaffalitzky (2004), Hartley and Zisserman (2004), Nordberg (2009), Oliensis (2002)]. The technique used in my thesis is an iterative triangulation scheme followed by [Parker et al. (1993)].

Mathematically it is expressible as the following [Morrison (2012)]:

$$\begin{aligned} \underline{m}_1 &= \underline{m}_{11} + k_1 \left[\underline{m}_{12} - \underline{m}_{11}\right] \\ \underline{m}_2 &= \underline{m}_{21} + k_2 \left[\underline{m}_{22} - \underline{m}_{21}\right] \\ \underline{m}_3 &= \underline{m}_{31} + k_3 \left[\underline{m}_{32} - \underline{m}_{31}\right] \end{aligned} \tag{B.2}$$

where $m_j\,(j = 1, 2, 3)$, is random points on an individual line connecting two extreme points m_{j1} and m_{j2}. The $k_i\,(i = 1, 2, 3)$, are parameters to be determined. Let m_0 be the centroid point or closed point of all the three above lines; consequently:

$$\left(\underline{m}_0 - \underline{m}_j\right) . \left(\underline{m}_{j2} - \underline{m}_{j1}\right) = 0 \tag{B.3}$$

Using equations (B.2 and B.3) we can get the subsequent expression:

$$\begin{aligned} \left[\underline{m}_0 - \underline{m}_{j1} - k_j(\underline{m}_{j2} - \underline{m}_{j1})\right] .(\underline{m}_{j2} - \underline{m}_{j1}) = 0 \\ k_j = \frac{(\underline{m}_0 - \underline{m}_{j1}).(\underline{m}_{j2} - \underline{m}_{j1})}{|(\underline{m}_{j2} - \underline{m}_{j1})|^2} \end{aligned} \tag{B.4}$$

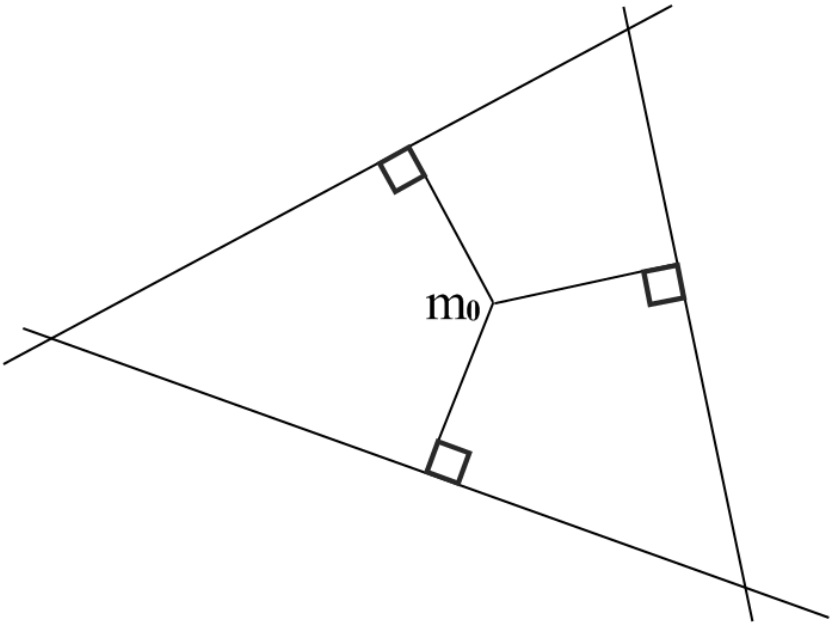

Figure B.2: Shortest distances from centroid point to LoRs.

Therefore, the perpendicular distance between the point m_0, the centroid point and one of three trajectories defined in equation (B.2) is given by:

$$\begin{aligned}\delta_j(m_0) &= |\underline{m}_0 - \underline{m}_j| \\ &= |\underline{m}_0 - \underline{m}_{j1} + k_j\left(\underline{m}_{i2} - \underline{m}_{j1}\right)| \\ &= \sqrt{A - B - C - D}\end{aligned} \tag{B.5}$$

where $A = |\underline{m}_0|^2 + (k_j+1)^2|\underline{m}_{j1}|^2 + \mu^2|\underline{m}_{j2}|^2$, $B = 2(1+k_j)\left(\underline{m}_0.\underline{m}_{j1}\right)$, $C = 2k_j\left(\underline{m}_0.\underline{m}_{j2}\right)$ and $D = 2k_j(1+k_j)\left(\underline{m}_{j1}.\underline{m}_{j2}\right)$. Consequently, the total distance between the point m_0 and the aforementioned three LoRs is given by:

$$\begin{aligned}\delta_T &= \delta_1(m_0) + \delta_2(m_0) + \delta_3(m_0) \\ &= \sum_1^3 \delta_i(m_0)\end{aligned} \tag{B.6}$$

Furthermore, the mean distance between the centroid point m_0 and three LoRs is given by:

$$\overline{\delta_T} = \frac{1}{3}\delta_T \tag{B.7}$$

In general, recorded PET data consists of a large number LoRs from which a single set S_0, composed of LoRs, $L_1, L_2, ...L_N$ is selected for triangulation [Parker et al. (1993)]. Let m_{S0} be the centroid point or minimum distance point for the set S_0. Consequently, the total minimum distance between the LoRs in set S_0 is given by:

$$D_T(S_0) = \sum_{1}^{N} \delta_j(m_{S0}) \tag{B.8}$$

where $\delta_j(m_{S0})$ is the distance between the j^{th} LoR or trajectory from the centroid point m_{S0}. Furthermore, the mean, $\overline{D_T}$, of these distances can be expressed as:

$$\overline{D_T} = \frac{1}{N} D_T(S_0) \tag{B.9}$$

where N is the total number of LoRs in set S_0. According to equation (B.9), it is obvious that the uncertainty of this triangulation depends on both the summation of individual distances from the centroid point to each LoR and the total number of LoRs. However, both of them uniquely impact the governing uncertainty. Therefore, in order to attain the best possible triangulation accuracy, individual distances larger than some predetermined value should be eliminated first. This method is called iterative triangulation. This technique improves the accuracy of determination of the value of the centroid point. Using analytical expressions, we can calculate the coordinates of m_{S0} and consequently the values of $\delta_j(m_{S0})$.

Consider the outlines of the iterative scheme for the triangulation.

1. In the zeroth step of the iterative scheme, m_{S0} is estimated and the distances, $\delta_j(m_{S0})$, larger than the mean value, $\alpha\overline{D_T}$, are discarded. The constant, β, is a fixed parameter employed in controlling the speed of convergence of the iteration. As a consequence, a new set,S_1, of the LoRs are obtained from this first step of the iterative scheme and are used to generate an improved estimate of the centroid point, m_{S1}, and the mean value, $\overline{D_T}(S1)$. Consequently:

$$\begin{aligned} \overline{D_T}(S0) &> \overline{D_T}(S1) \\ m_{S0} &> m_{S1} \\ N(S_0) &> N(S_1) \end{aligned} \tag{B.10}$$

   where $N(S_0)$ and $N(S_1)$ are the number of LoRs in set S_0, and set S_1 respectively.

2. Generally, a new set S_j can be created by imposing an upper limit, $\lambda\overline{D}_T(S_{j-1})$, on the LoRs in the previous subset, S_{j-1}; thus generating an improved value for the estimate of the centroid point and mean value. The new set is characterised by the following inequalities:

$$\begin{aligned} \overline{D_T}\,(S_{j-1}) &> \overline{D_T}\,(S_j) \\ m_{S(j-1)} &> m_{S(j)} \\ N\,(S_{j-1}) &> N\,(S_j) \end{aligned} \tag{B.11}$$

3. The iterative scheme is terminated when a specified fraction, f, of the initial LoRs remain. This condition is expressed as follows:

$$N\,(S_j) = fN\,(S_0) \tag{B.12}$$

4. If $N\,(S_j)$ is less than the specified number, then the closest LoRs that were previously rejected, are once again included in the iterative scheme until the condition expressed in equation (B.12) is satisfied.

5. The termination of the iterative technique can be achieved by targeting a specified mean value, i.e.,$\overline{D_F}S_j$ is less than the specified value, then the iteration is terminated.

6. Let S_T and m_{S_T} be the set of LoRs and centroid point of the final iteration, respectively. Each LoR is associated with the time different recorded time t_j. Therefore, the centroid point m_{S_F} is considered to be the position of the particle at an average time t_{ave} [Parker et al. (1993)].

$$t_{ave} = \frac{1}{N_F} \sum_{S_F} t_j \tag{B.13}$$

   where N_F be the number of LoRs in the final step of iteration.

A triangulation technique executed for a moving particle is not similar to the one employed for a stationary particle. However, a triangulation technique for a stationary particle is considered as a building blocks for a triangulation of a moving particle. If LoRs resulted from a moving particle are divided into sufficiently short time intervals, then we can assume a moving particle is nearly stationary within each time intervals. This assumption allows us to employ the triangulation of the stationary particle to a moving particle.

B.5 Termination-Point of Triangulation Iteration

As I elucidated prior, there are two factors, the fraction of initial LoRs remaining and value of the uncertainty of the position of the tracer particle, destine the condition of termination of iteration process. It has been elaborated clearly how uncertainty of the position of the particle varies with the fraction of initial LoRs remaining [Parker et al. (1993)]. Further, it has been shown that precision of triangulation of the tracking particle depends on the amount of radioactivity given by the tracer particle and, the physical and chemical properties of the tracer [Fan and Smith (2006)].

B.6 Effects of Tracer Properties on PEPT results

A precision δ of locating a stationary tracer particle is given by [Fan and Smith (2006)]:

$$\delta = \frac{\sigma}{\sqrt{fN}} \tag{B.14}$$

where σ is spatial resolution of a PET camera, f represents a fraction of original events remaining and N is the number of events in the beginning of the iterative technique. The precision of the triangulation can be enhanced by increasing the value N; however, if the N is increased such that to incorporate more corrupted LoRs, then it might influence the precision of the triangulation [Bridgwater et al. (2004)]. The number of LoRs are employed to extract for the triangulations of the tracer particle relay on the velocity and radioactivity and the volume of material over which the gamma photons have to pierce before detection by PET scanners [Fan and Smith (2006)].

Throughout the PEPT experiment the tracer particle is situated in and amongst the population of particles being investigated. The whole system, inclusive of the tracer particle, is considered as a single granular system. Each particle in this granular system exhibits two types of motion; rotational and translational. Under given operational conditions of the rotating mill, both kinds of motion are completely determined by the size, mass, shape and surface properties of the particles. Therefore, it is very important that the tracer particle should be identical with other population of particles [Fan and Smith (2006)].

B.7 Tracer Labelling

The half life time of the tracer used in a PEPT experiment should be sufficient enough to cover the period necessary for tracking the trace particle, the time needed to take out the tracer particle from the rest of the bulk population, and the time required to set the configuration of the PET scanner. However, the half-life time should not be so long as to pose a radiation hazard due to the protracted radioactivity. The radioisotopes produced in iThemba Labs are ^{67}Ga, ^{123}I solutions, ^{123}I capsules, $^{123}I[MIBG]$, ^{18}F and ^{8}Ge. However, ^{18}F is regularly employed in PEPT experiments, because it only emits mono-energetic (511keV) gamma photons. Moreover, this energy is favourable for obtaining an extremely high accuracy in the locating of the tracer particle. Also, the half-life time (109 min) of ^{18}F is appropriate for particle tracking experiments. There are two main methods employed in the production of ^{18}F radioisotopes. The first of these, is performed by directing a high energy beam composed of ^{3}He isotopes at a volume of purified water within a container constructed of titanium, silver, or some other solid material [Fan and Smith (2006)]. Generally, this high energy beam is generated by a cyclotron. ^{18}F obtained from purified water is in an ionic state and therefore can be readily absorbed by organic or in-organic material via ion-exchange or surface absorption [Fan and Smith (2006)].

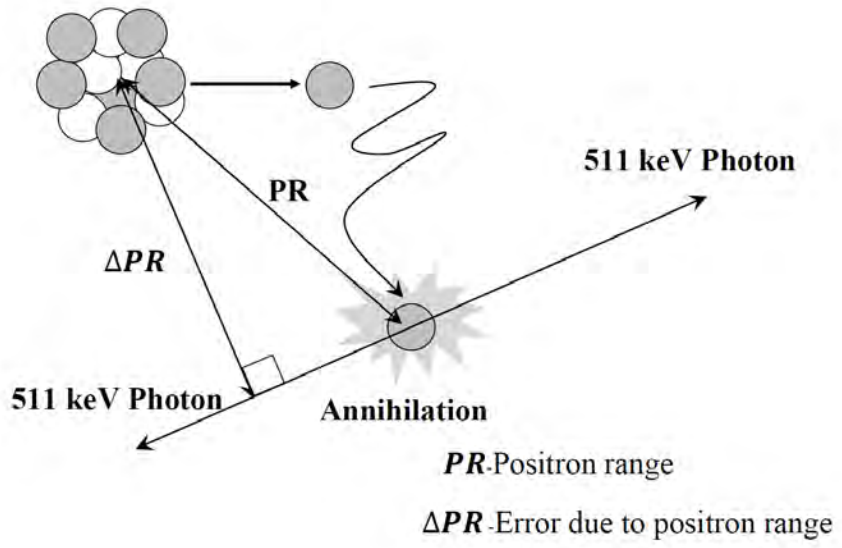

Figure B.3: The Positron Range: Error in determination of the location of positron emitting radionuclide due to Positron Range.

B.8 Uncertainty associated with the PEPT Technique

In addition to the aforementioned process, gamma photons are also created when an excited daughter nucleus de-excites from a metastable state to its stable ground state. These gamma photons are not relevant to the thesis; however, the presence thereof does perturb the triangulation procedure. Furthermore, a positron emitted from a parent nucleus, thermalizes through interactions with the medium before being absorbed by an electron to form a meta-stable nucleus called positronium. This positronium is a meta-stable bound state of an electron positron pair and exists in the two following excited states: ortho-positronium in which the spin alignment of the electron positron pair is parallel (triplet state) and para positronium in which the spin alignment is anti-parallel (singlet state). The positronium exists in one of these excited state for an extremely brief period after which the positron and electron annihilate, producing gamma photons.

Furthermore, determination of a LoR is governed by the range of a positron and non-colinearity. The following two paragraphs describe the above two factors aforementioned above.

The range of a positron is defined as the distance from which it originates, i.e the location of the parent nucleus, to where it annihilates with an electron. As we know, LoRs do not represent lines along which the tracer particle is located. Moreover, positrons deviate from their original paths as a result of interactions with the medium before annihilating with electrons. Therefore, as shown in figure (B.3) the net distance drifted by a positron differs from its expected range. However, with PET imaging, the perpendicular distance from the point of emission, to the point of annihilation, is defined as the range of the positron. Another

important consideration, is that the ranges of positrons emitted from different radionuclides are not the same, and depend on the type of radionuclide. Hence, the spatial resolutions of PET scanners differ according to the type of radionuclides employed.

The second effect arises from a non-zero initial energy and momentum of the positron-electron pair from which the annihilation gammas are formed. Evidently, this means the pair are not at rest before they annihilate. As such, the resulting pair of emitted gamma photons do not propagate in opposite directions along a perfectly straight line. Therefore, the angle at which the gamma photons are emitted will exhibit some distribution about the 180^0. This phenomenon resulting in a spread of the angle at which the back-to-back gamma photons are emitted is known as nonlinearity. The effect is depicted in figure (B.4). Unlike the positron range, the effect of nonlinearity is independent of the type of radionuclide employed. When performing PEPT experiments, the effects of nonlinearity are generally not considered; however, it has been shown in [Phelps (2006), Levin and Hoffman (1999)] that the effect of nonlinearity depends linearly on the diameter of the PEPT scanner used.

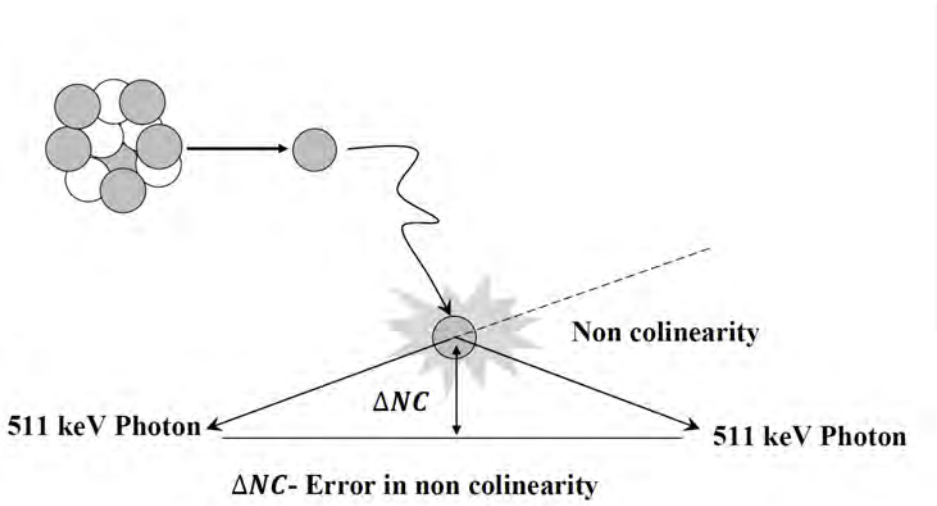

Figure B.4: The Nonlinearity of annihilated photons: Error in determination of the location of positron emitting radionuclide due to nonlinearity Phelps (2006)

In addition, the attenuating environment and its strength affect the propagation of annihilation photons. Therefore, before reaching the detector, the direction of propagation of these gamma photons are altered according to the attenuating strength of the medium. As a tracer particle rotates within the medium of the rotating mill, the physical configuration of the surrounding environment changes with the time. As such, the photons from annihilations, have to cross different sizes of attenuating medium before reaching the detectors of the PET scanner.

Generally, we always talk about the point where an annihilation gamma photon is projected onto the front surface of the PET scanner detectors. If the surface of the PET detectors are made with a very thin material, then it is enough to consider a point of projection on the front surface of the detectors as the final destination of the gamma photons. However, the surfaces of PET detectors are in fact not made with thin materials, and exhibit surface thicknesses generally in the range from 2cm to 3cm. Therefore, it is essential to consider the

photon depth of interaction within the detector. Furthermore, the uncertainty in the depth of interaction compromises the spatial resolution of images. In [Levin et al. (1997),Phelps (2006)], the adverse effects of depth interaction on LoR assignment are discussed.

Further positional errors are affected by Compton scattering within the PET detector material [Levin and Hoffman (1999)] as well as scintillation light multiplexing. The technique to control these source of errors is described exhaustively in [(Moses and Derenzo, 1994), Habte et al. (2005)]. In [Parker et al. (1993)], the tracer particle is assumed to be a point in the iterative triangulation technique; however, this is evidently not the case. Consequently, this assumption impacts the accuracy of the triangulation procedure. Despite the finite size of the tracer particle, it is treated as a point charge in single and multi-particle tracking experiments. This point charge simplification of the tracer particle is used in the iterative triangulation technique [Parker et al. (1993)]. Of course, the tracer particle does possess some finite physical dimensions; consequently, this assumption impacts negatively on the triangulation procedure, particularly when the tracer particle is in motion.

Appendix C

Scintillation Detectors in PET

Scintillation detectors are the most common detectors employed in PET scanners. These detectors exhibit an exceptionally high efficiency in detecting 511keV gamma photons, when they impinge on the surface of the detector. An effective mode of detection is strongly based on the ability of the detector to stop annihilated gamma photons, the signal decay time and the intrinsic energy resolution of the detector [Phelps (2006), Bailey et al. (2005b)]. The stopping power of the constituent crystal material of the scintillator, governs the mean distance traversed by the annihilation photon before depositing its energy. Therefore, scintillation material characterised by a very short mean path display a higher efficiency in stopping the annihilated 511 keV gamma photons. The stopping power of the detector depends on the intrinsic physical properties of the detector material; chiefly, the density and effective atomic number [Saha (2010)]. It is highly advantageous that PET detectors be comprised of scintillation material characterised by a large stopping power as this lowers the parallax errors in acquired images [Bailey et al. (2005b)].

Proceeding some interval of time, an atom excited by a photon returns to its ground state. Upon returning to this ground state a characteristic photon in the visible light spectrum is emitted. Both the decay time and the quantity of light output are based on the intrinsic nature of the material used in the detector. A shorter scintillator decay time is useful for enhancing the detector efficiency at high count rates. Therefore, a shorter decay time delivers an enhanced energy resolution [Bailey et al. (2005b), Saha (2010)]. In addition, the light output from the scintillation material affects the image generated by the PET scanner. Essentially, a high light output from the scintillation material provides a better spatial resolution [Moszynski et al. (2004), Murthy et al. (1994)], a higher coding ratio and a good energy resolution. As shown in table (C.1), the maximum value of the intrinsic energy resolution of a detector is 20% for a routine integration time for pulse formation. However, in the PET imaging process, the imaging time is a thousand times shorter than the routine time in order to exclude random coincidences. Consequently, the number of photoelectrons collected from a single pulse is relatively small, and leads to a deterioration in the energy resolution.

Generally, NaI(Tl) is preferred as a scintillator material. This is primarily as a result of its superior light output capabilities, which has the advantageous effect of increasing spatial as well as energy resolutions. Examples of its use can be found in: PC-I [Burnham and Brownell (1972)], the ECAT systems [Phelps et al. (1978)] and Donner 280 crystal ring scanner

[Derenzo et al. (1988)]. Bismuth germinate (BGO) constitutes the scintillator material in most PET scanners [Burnham and Brownell (1972), Cho and Farukhi (1977), Derenzo et al. (1979)] because it possesses the highest stopping power (higher density and linear attenuation coefficient)[Bailey et al. (2005b)]. BGO scintillators are expected to provide a higher spatial resolution than NaI(Tl), because comparitively, annihilated photons have significantly shorter attenuation lengths in BOG. Consequently, this inherent property of BGO permits the use of a large number of crystals within the PET geometry. However, its decay time is longer and therefore compromises the efficiency of the detector at high count rates [Phelps et al. (1978), Saha (2010)]. Furthermore, BGO emits very low light output and consequently provides a poor energy resolution [Saha (2010)].

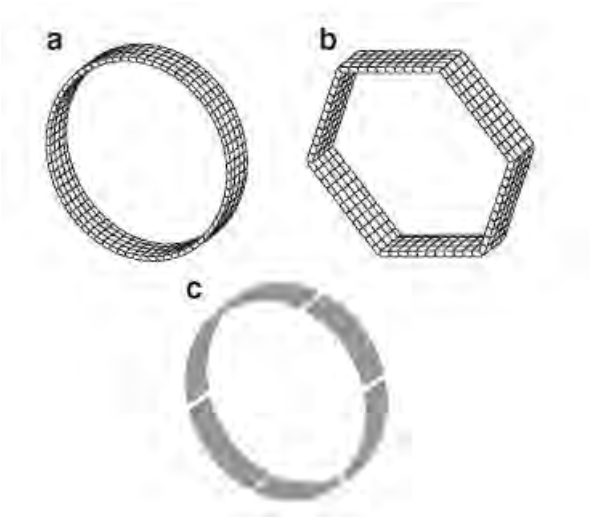

Figure C.1: Types of configurations used for PET detectors: (a) Circular full-ring scanner. (b) Hexagonal array of quadrant-sharing panel detectors. (c) Continuous detectors using curve plates of NaI(Tl) [Saha (2010)]

Property	NaI(Tl)	BGO	LSO	YSO	GSO	BaF_2
Density (g/cm^3)	3.67	7.13	7.4	4.53	6.71	4.89
Effective Z	50.6	74.2	65.5	34.2	58.6	52.2
Attenuation Length (nm)	2.88	1.05	1.16	2.58	1.43	2.2
Decay Constant (ns)	230	300	40	70	60	0.6
Light Output (Photons/ KeV)	38	6	29	46	10	2
Relative light Output (%)	100	15	75	118	25	5
Intrinsic ($\Delta E/E$)	5.8	3.1	9.1	7.5	4.6	4.3
$\Delta E/E(\%)$	6.6	20	10	12.5	8.5	11.4
Attenuation Coefficient $\mu(cm^{-1})$	0.3411	0.9496	0.8658	0.3875	0.6978	0.4545
Index of Refraction	1.85	2.15	1.82	1.8	1.91	1.56

Sodium Iodide doped with Thallium (NaI(Tl))
Bismuth Germanate $Bi_4Ge_3O_{12}$(BGO)
Iutetium Oxyorthosilicate doped with Cerium $Lu_2SiO_5 : Ce$ (LSO)
Yttrium Oxyorthosilicate doped with Cerium $Y_2SiO_5 : Ce$ (YSO)
Gadolinium Oxyorthosilicate doped with Cerium $Gd_2SiO_5 : Ce$ (GSO)
Barium Fluoride

Table C.1: Physical properties of commonly used scintillator in PET. The energy resolution and attenuation coefficients are measured at 511 keV [Bailey et al. (2005b), Saha (2010)].

Table ($C.1$) displays the pertinent characteristics of the several types of scintillation material. The choice of scintillation material to be utilised in the PET detectors, is based on an overall comparison of the numerous relevant properties of the materials. The preferred qualities of scintillation material include: short decay time, high light output, short attenuation length and high density. LSO possesses all the aforementioned favourable qualities which seemingly make it a perfect candidate for use in scintillator material. On the other hand however, LSO is associated with an extremely low energy resolution. Although LSO possesses a naturally occurring radioisotope, ^{176}Lu, which decays via β^- decay producing an excited daughter which stabilises with the emission of an X-ray/s with energy in the range 88-400 keV, these emissions do not produce substantial background noise because the energy window does not accept radiation of such low energies.

Despite Gadolinium Oxyorthosilicate (GSO) possessing a lower stopping power and light output than LSO, manufactures adopt GSO as a PET detector due to its superior energy resolution and excellent decay time [Bailey et al. (2005b), Humm et al. (2003)]. Faster data collection is a special intrinsic property of the GSO, however, these crystals are extremely fragile and, therefore require careful storage [Saha (2010)]. Surprisingly, GSO can be cut into remarkably small pieces of crystal, consequently, the dimensions of these crystals allow for an exceptional spatial resolution in PET images.

Appendix D

2D Distributions of PEPT Data

The 2D azimuthal maps discussed in chapter (6) are presented in this Appendix. No discussion is given herein. This chapter serves purely as a compliment to the discussion given in chapter (6).

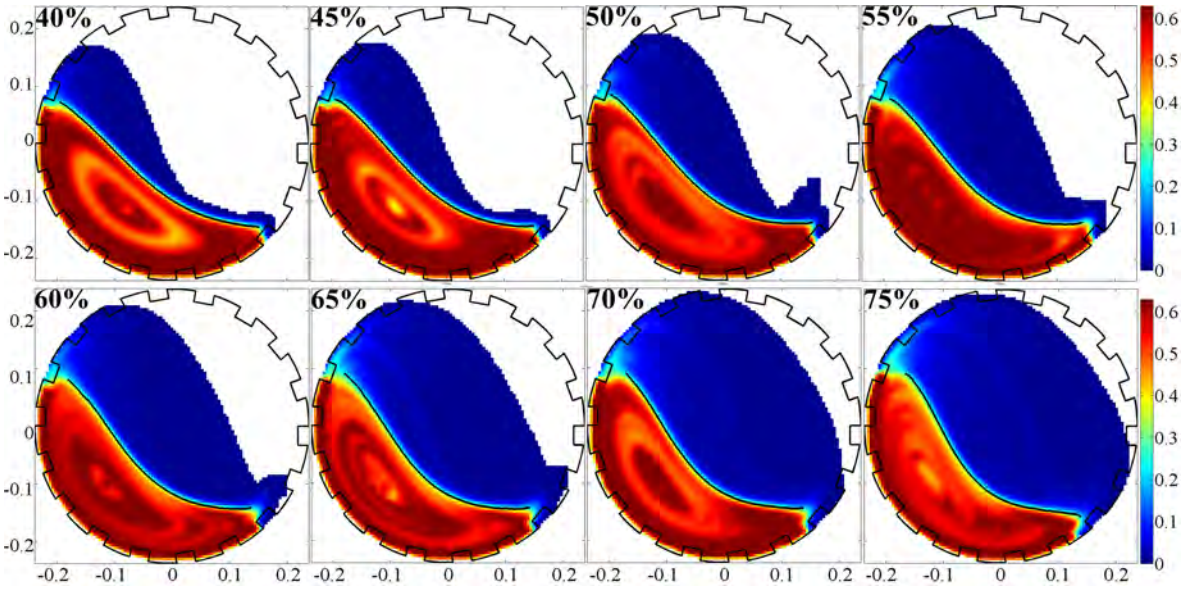

Figure D.1: Volume concentration distribution of the 5mm sized glass bead charge derived from PEPT experiments.

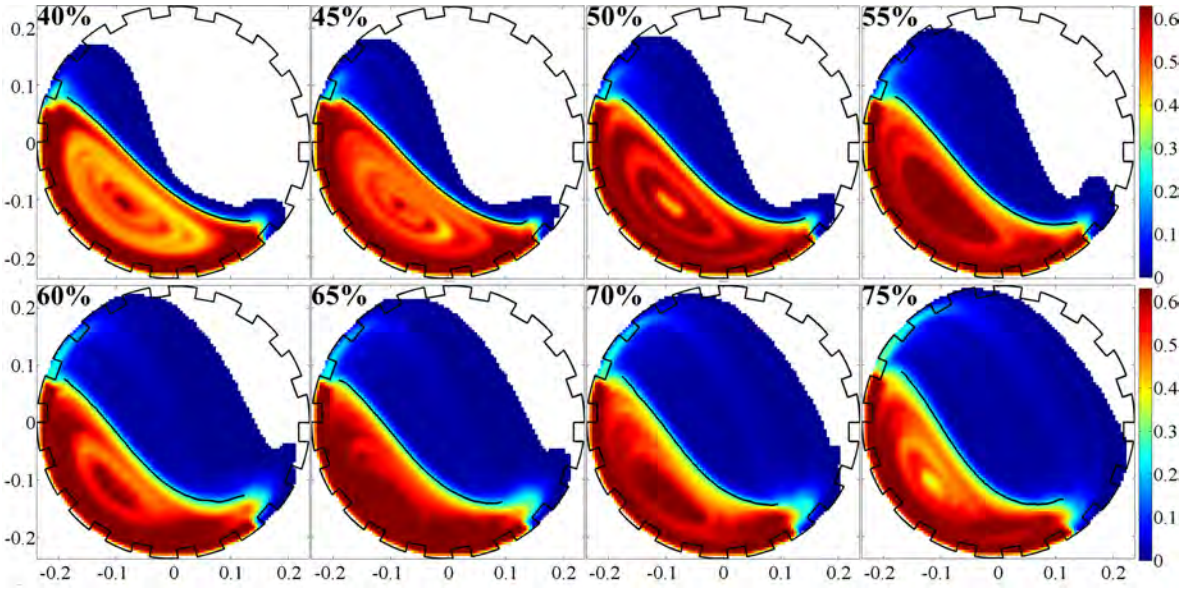

Figure D.2: Volume concentration distribution of the 8mm diameter glass bead charge derived from PEPT experiments.

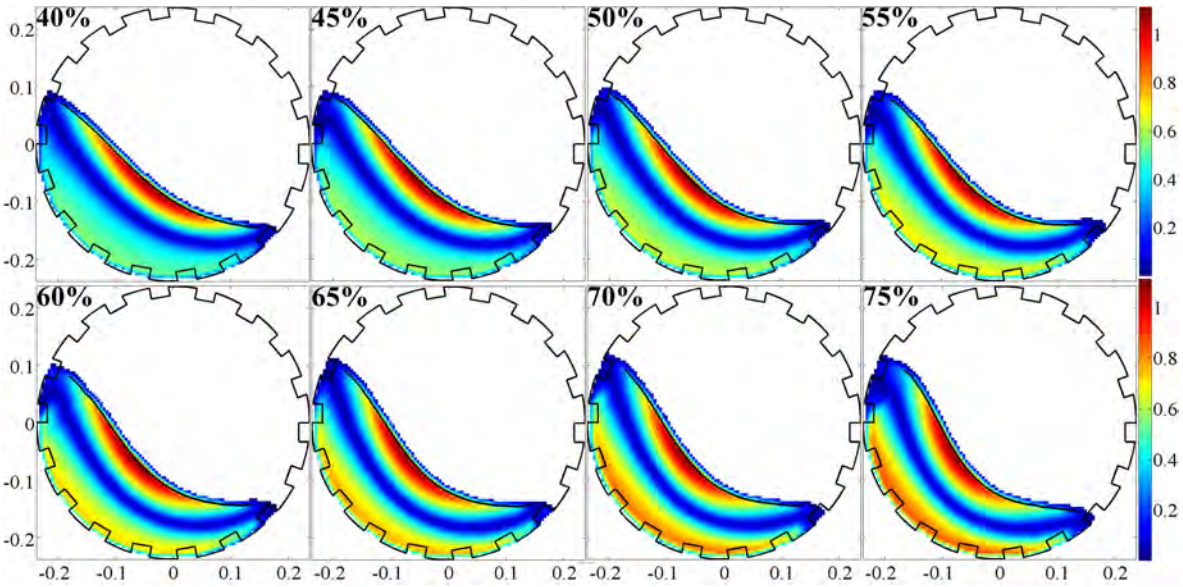

Figure D.3: Tangential velocity distribution of the 5 mm sized glass bead charge derived from PEPT experiments.

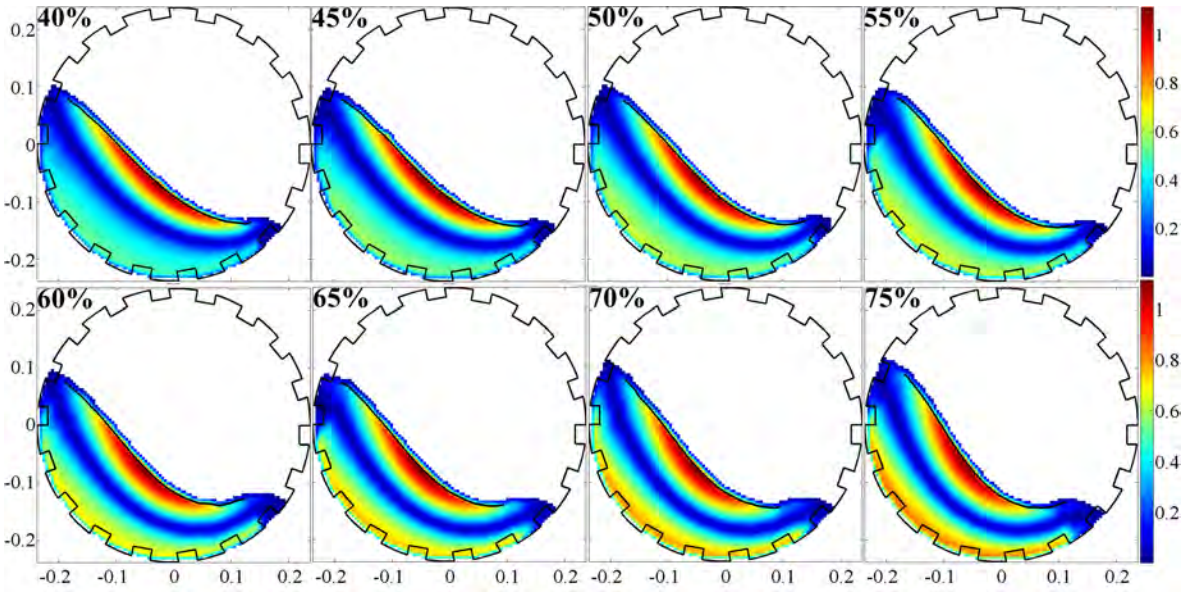

Figure D.4: Tangential velocity distribution of the 8 mm sized glass bead charge derived from PEPT experiments.

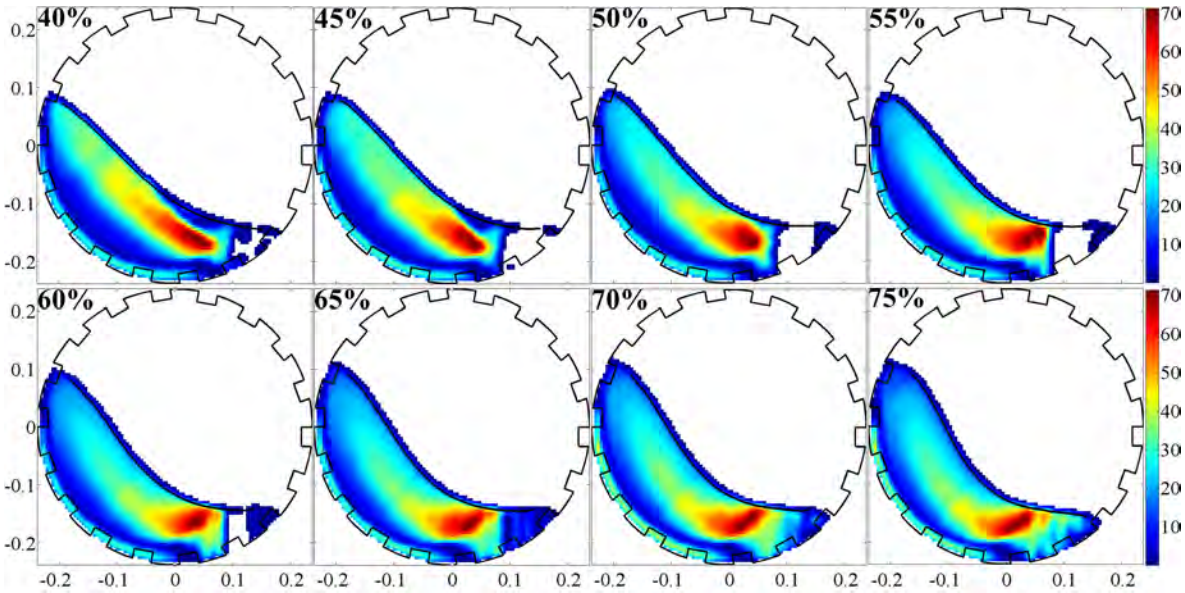

Figure D.5: Shear rate distribution of the 5 mm sized glass bead charge derived from PEPT experiments.

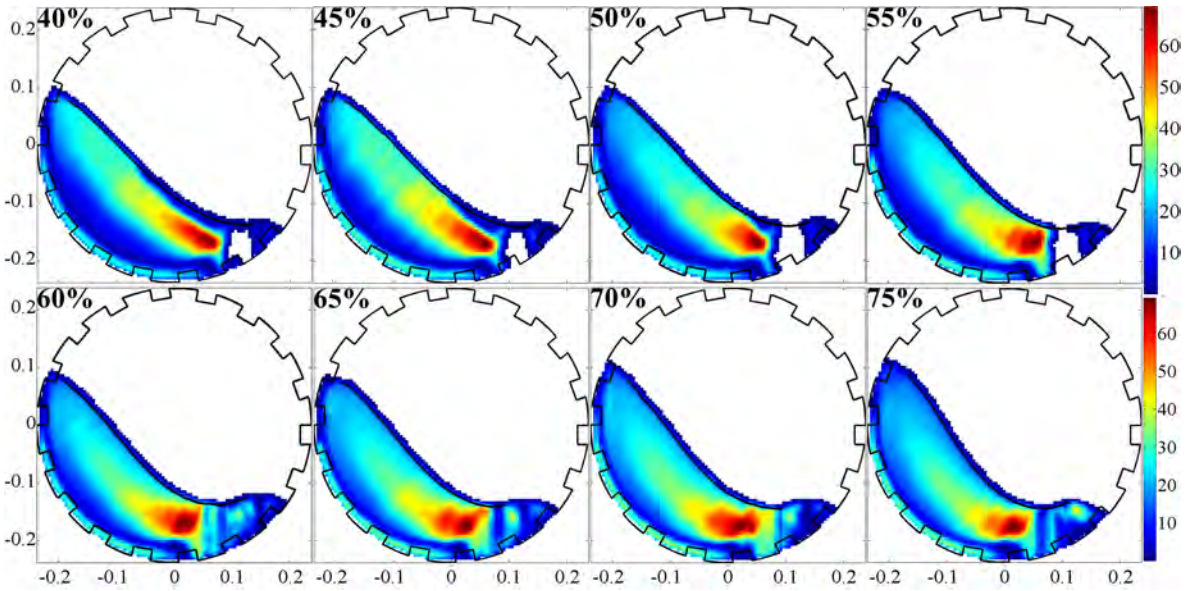

Figure D.6: Shear rate distribution of the 8 mm sized glass bead charge derived from PEPT experiments.

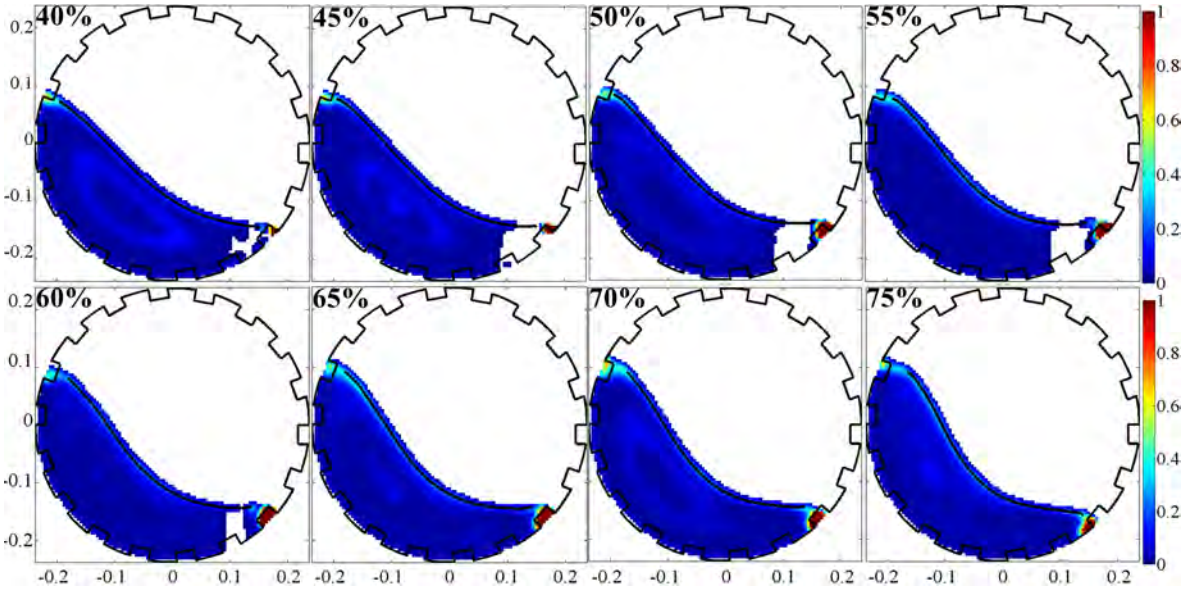

Figure D.7: Inertial number distribution of the 5 mm sized glass bead charge derived from PEPT experiments.

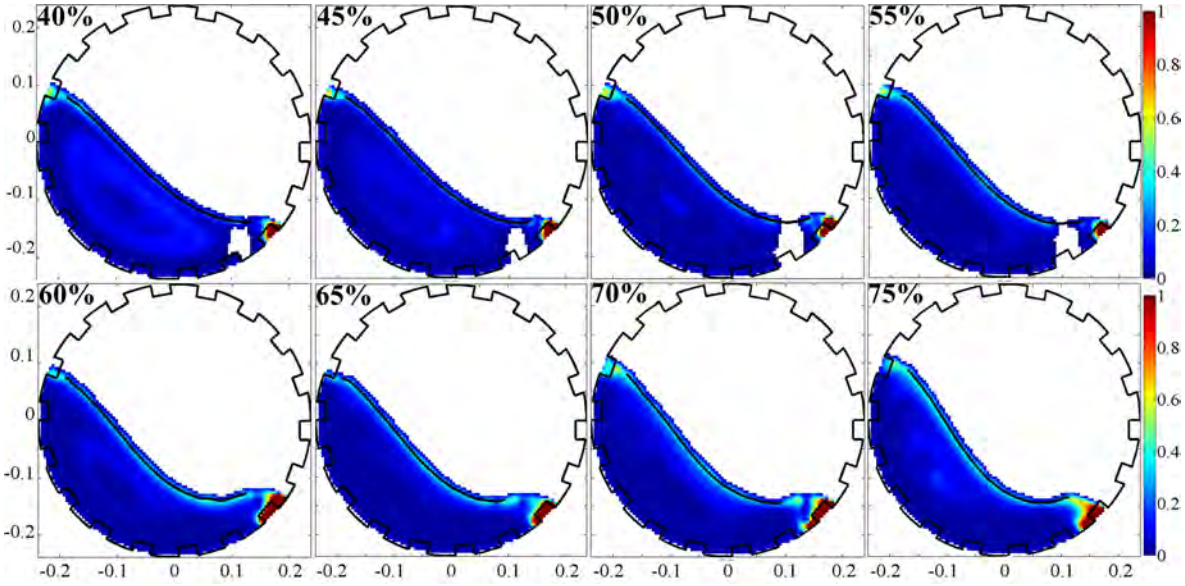

Figure D.8: Inertial number distribution of the 8 mm sized glass bead charge derived from PEPT experiments.

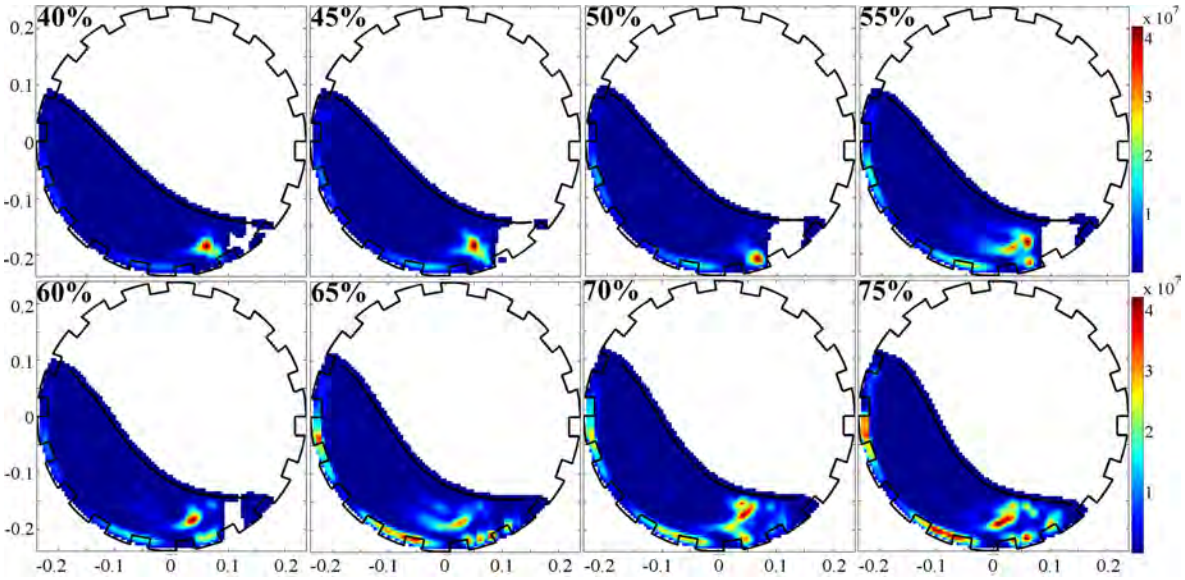

Figure D.9: Power dissipation due to compressive stresses between 5mm sized granules derived from PEPT experiments.

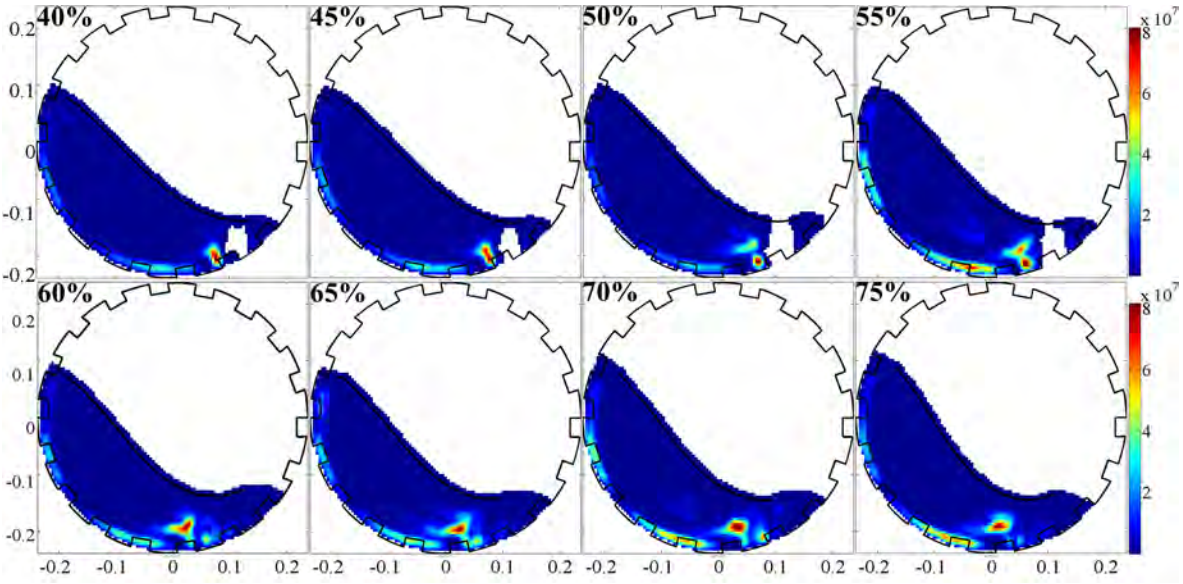

Figure D.10: Power dissipation due to compressive stresses between 8mm sized granules derived from PEPT experiments.

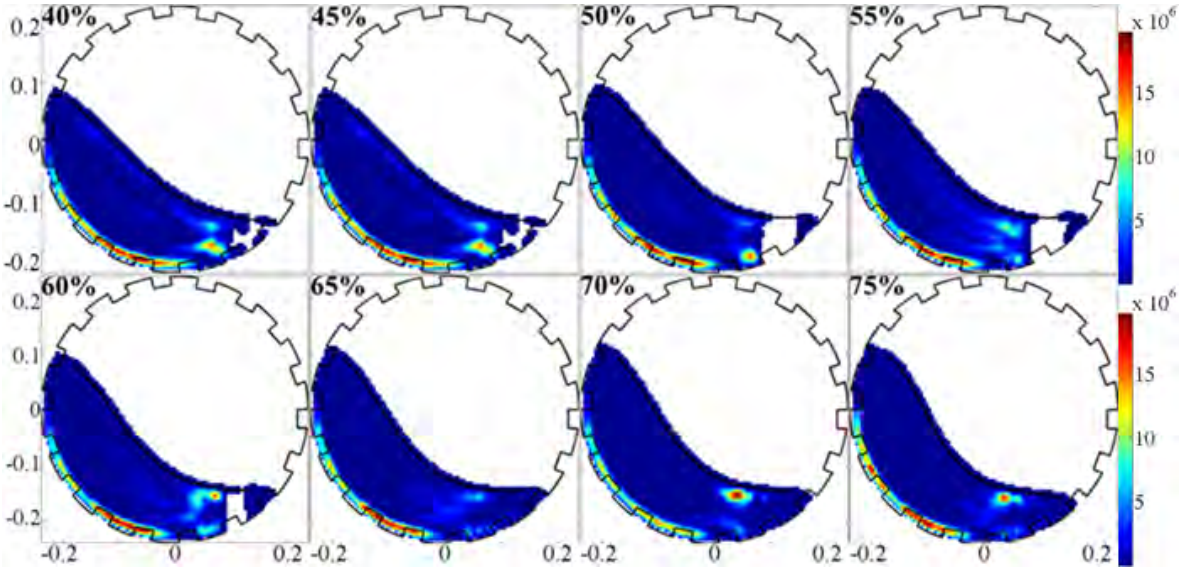

Figure D.11: Power dissipation due to shear stresses between 5mm sized granules derived from PEPT experiments.

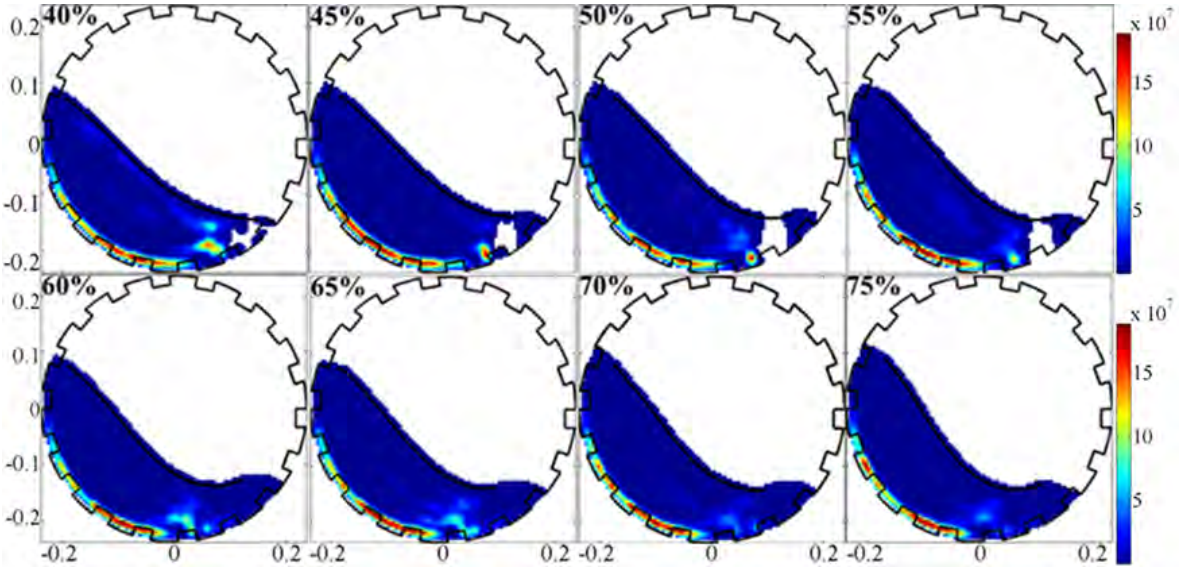

Figure D.12: Power dissipation due to shear stresses between 8mm sized granules derived from PEPT experiments.